UNIVERSITY OF SOUTHAMPTON

Evolution of spin and orbital periods in isolated white dwarfs and related binary systems

Carolyn Brinkworth

SCHOOL OF PHYSICS AND ASTRONOMY

FACULTY OF SCIENCE

May 14, 2005

UNIVERSITY OF SOUTHAMPTON

ABSTRACT

FACULTY OF SCIENCE

SCHOOL OF PHYSICS AND ASTRONOMY

Doctor of Philosophy

Evolution of spin and orbital periods in isolated white dwarfs and related binary systems

by Carolyn Brinkworth

Variability in isolated white dwarfs and associated binary systems can reveal a large amount of information about the source. We have used photometric variability to derive the spin periods of seven magnetic white dwarfs, and in the process we have discovered variability in $\sim 55\%$ of our sample. We believe that in at least two of our sources we have discovered the first star spots ever to be detected on the surfaces of white dwarfs. We also investigate the changing period of the eclipsing pre-cataclysmic variable NN Ser by measuring the timings of the system's mid-eclipses using the high-speed CCD camera, ULTRACAM. We find that the period is shortening at an average rate of $\dot{P} = (9.057 \pm 0.005) \times 10^{-12}$, consistent with standard models of orbital period change derived for much more massive secondary stars, and two orders of magnitude higher than the current theoretical prediction. We also discuss other potential mechanisms for this observed period change.

Contents

List of Figures

List of Tables

Acknowledgements

A huge thank you to Tom Marsh for his endless patience, brilliant supervision, and for actually reading this. Thanks in equal measures to Christian Knigge for taking over the job when Tom headed to Warwick. I promised I wouldn't take up much of his time, but I think I lied. Thanks too to everyone else who helped me over the 3 years, especially Katherine, Luisa and Ralph who acted as first-filter to catch the really stupid questions before they got as far as Tom. All credit to my various office mates - Luisa, Jose, Vanessa, William, Dave, Matt, Nick, Silas and Eduardo: not only did they not throttle me, I also never felt the compulsion to throttle them. To my pseudo-housemates (Ross, Shaggy, Kirsty, Kate), all my friends at work (esp. Ed and Liz) and home (Helen, Lizzie, Claire & Hannah), a huge thank you to you all for making me laugh and keeping me sane.

Finally, the biggest vote of thanks has to go to my family for their unconditional love and support. This is dedicated to my brother, Rob - the better-looking, funnier and more socially adept member of the family, and my favourite person in the world.

Chapter 1

Introduction

This thesis is based upon photometric observations of variability in isolated and binary white dwarf systems. Variability in isolated systems can either be interpreted as pulsations in the star (on periods 100 – 1200 s) or, on longer timescales, as a result of the spin period of the source. Variability in binary systems is more complicated, but contains far more useful information about the system. This chapter aims to introduce the background required to understand the analysis and results contained in Chapters 2-5.

1.1 Isolated stars

1.1.1 White Dwarfs

White dwarfs (WD) are the remnants of low-mass ($0.7\,\mathrm{M}_{\odot} < M < 7\,\mathrm{M}_{\odot}$) stars similar to our Sun. All stars spend the majority of their lifetimes gradually converting hydrogen into helium by the process of nuclear fusion in their cores. During this

time they are in balance, with the force of gravity acting to collapse the star matched by the thermal and radiation pressure sustained by nuclear burning. As long as the star continues to fuse hydrogen into helium, and so continues to produce energy, this balance is maintained and the star is said to be a "main-sequence" star. At some point, however, the hydrogen "fuel" in the stellar core will be depleted. When this happens, core nuclear burning stops, although burning in a hydrogen shell around the core will continue. The helium core begins to cool, the pressure drops, and so it contracts, turning gravitational energy into thermal energy and heating up. This new source of heat accelerates the shell hydrogen burning, which spreads further out into the surrounding matter. The helium "ash" from the shell falls to the core, increasing its mass and causing it to keep contracting and heating up. The increased heat flow from the core, combined with the shell hydrogen burning, massively increases the luminosity of the star. The outer atmosphere expands as it compensates for the increased heat flow from the centre, turning the star into a "red giant". The star will undergo substantial mass loss during its red giant phase, as the outermost layers of the star are so far from the core that it has a relatively low surface gravity.

The core continues to contract and heat up until it finally reaches the critical temperature (about 100 million Kelvin) for helium to begin fusing into carbon and oxygen. The core then expands, reducing the radiation outflow and causing temperatures to drop in the surrounding gas. This slows the shell hydrogen burning and allows the outer layers of the star to contract and heat up. The star enters a second, shorter, stable core burning phase, although most of the star's luminosity is still generated by the hydrogen shell burning. During this time the star is a sub-giant. Eventually, after about 100 million years, the helium in the core will run out. The core will contract for a second time until it is prevented from doing so by electron degeneracy pressure. This contraction heats up the gas surrounding the core, and shell helium-burning begins.. As with shell hydrogen-burning, the release of energy

is enormous, and causes the star to enter a second red giant phase, this time more luminous than before. The star is now an "asymptotic giant branch" (AGB) star, comprising an inert carbon-oxygen core and helium- and hydrogen-burning shells, all surrounded by a hydrogen envelope. The hydrogen-burning shell, cooled by the expansion, becomes dormant for a while.

Later in the AGB phase, as the helium in the helium-burning shell becomes exhausted, the outer layers will contract and re-ignite the hydrogen shell. This begins dumping helium into the depleted helium-burning shell just below it, causing a series of "helium-shell flashes" and thermal pulses that eject the outer stellar atmosphere as a planetary nebula. The exposed core is left to cool and fade over many millions of years, and this remnant is known as a "white dwarf".

The type of white dwarf created will depend on the initial mass of the parent star (progenitor), and therefore its evolutionary path. The scenario described above applies to white dwarfs with progenitors of mass $0.7 \sim 5\,\mathrm{M}_{\odot}$, which will leave a white dwarf composed mainly of carbon and oxygen. For lower-mass stars, the initial contraction phase will not heat the core sufficiently to ignite helium burning and so the remnant will be mainly composed of helium, although the evolutionary timescale of such stars is longer than the age of the Universe. Helium white dwarfs do exist, but are created by binary rather than single-star evolution. Meanwhile, those stars with masses $\sim 5 - 7\,\mathrm{M}_{\odot}$ are massive enough to ignite the carbon core as the helium becomes depleted, so creating oxygen-neon-magnesium white dwarfs. While the lower mass limit of white dwarf progenitors is simply constrained by the age of the Universe, there is a considerable uncertainty in the values of the upper mass limit quoted above.

White dwarfs are extremely compact objects, with a mass roughly that of our Sun, but a radius closer to that of the Earth. The mass distribution of white dwarfs

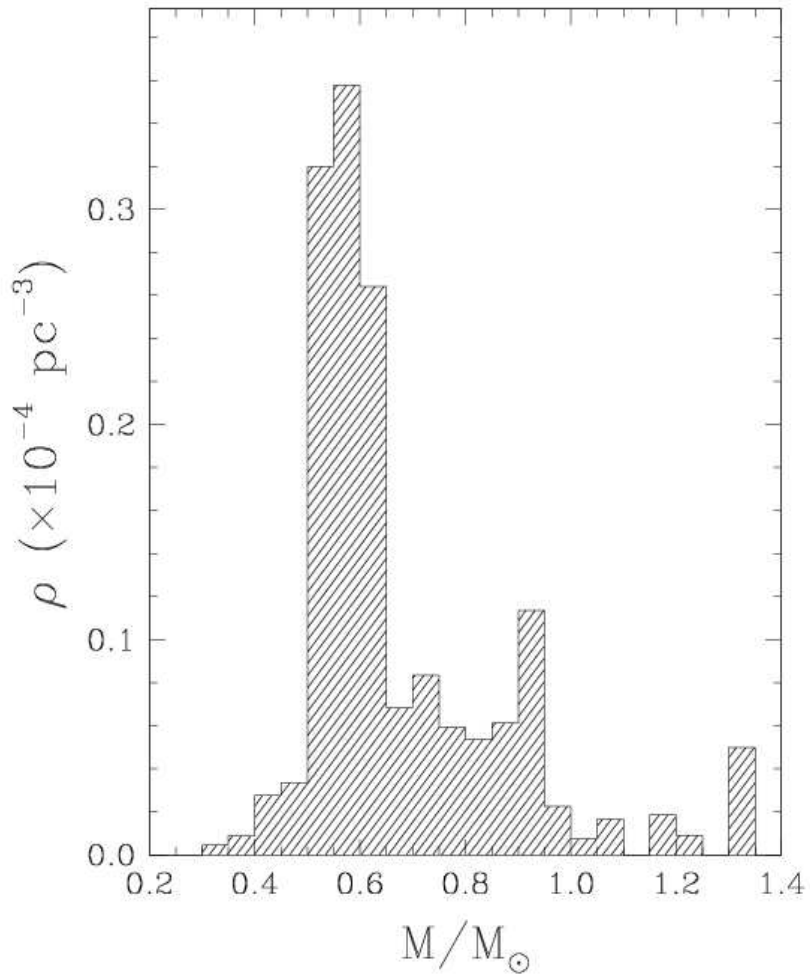

Figure 1.1: Mass distribution for white dwarfs, taken from Liebert et al. (2005).

shows a main peak at about $0.6\,M_\odot$, with a sharp low-mass peak centred around $0.4\,M_\odot$ and a broad higher-mass component around $0.8\,M_\odot$ (Liebert et al. 2005; see Fig 1.1). The maximum mass for a white dwarf is $1.4\,M_\odot$, called the Chandrasekhar limit. Above this mass the electron degeneracy pressure is not high enough to be able to balance the gravitational force, and the electrons are forced into their nuclei and combine with the protons to form neutrons. Instead of forming a white dwarf, a higher-mass body such as this would form a neutron star. Liebert et al. (2005) show that the majority of white dwarfs can form by single-star evolution as described above, but of the 15% of white dwarfs with masses $> 0.8\,M_\odot$, more than 80% of these are expected to have been formed by double-degenerate mergers (see also Marsh et al. 1997; Vennes 1999; Bergeron et al. 1992; Schmidt et al. 1992), although high-mass WDs may also be formed following a period of mass-transfer from a companion star. Temperatures are typically $T < 50,000\,K$ and their rotational periods are of order $P_{rot} \sim 1$ day.

1.1.2 Magnetic White Dwarfs

Recent studies have suggested that between 10 – 16% of all isolated white dwarfs have strong magnetic fields ($B = 3 \times 10^4 - 10^9\,G$, Kawka et al. 2003; Liebert et al. 2003; Schmidt & Smith 1995), and a further 25% may have weak magnetic fields near or below the current observational threshold (Aznar-Cuadrado et al. 2005). Liebert et al. (2003) also suggested that the incidence of magnetism among the local white dwarf sample may increase with decreasing temperature, luminosity (and therefore increasing cooling age). This is in contrast to the theoretical expectation that fossil fields should decay with time (Fontaine et al. 1973, but see Valyavin & Fabrika 1999 for a conflicting viewpoint).

1.1.2.1 Detection of magnetic fields

There are 4 main ways to detect magnetic fields in white dwarfs, although the full theory behind each of them is beyond the scope of this thesis. See Wickramasinghe & Ferrario (2000) for a more comprehensive review of the following methods.

1. *Zeeman spectroscopy.* Magnetic fields affect the electron energy levels in atoms by splitting them into discrete levels according to their magnetic quantum number, m, and orbital angular momentum, l. This, in turn, splits the spectral absorption lines, where the difference in frequency between the lines is a measure of the magnetic field strength. Advances in the identification of hydrogen and helium lines in strong fields (Wunner et al. 1985; Jordan et al. 2001) have led to a huge improvement in the estimates of the high field strengths seen in many white dwarfs. Zeeman splitting is detectable in stars with fields $\gtrsim 10^6$ G.

2. *Zeeman spectropolarimetry.* An electron in an atom can be modelled as a linear harmonic oscillator. When in a region with a magnetic field, the harmonic oscillator will precess about the field, and can be described as a combination of a linear oscillator along the field, a circular oscillator with the same sense as a free electron in the field, and a circular oscillator rotating in the opposite sense. These three components are the π, σ_+ and σ_- components, and their polarisation and intensity can be used to map the field strength and direction in the star. The σ components will be circularly polarised when viewed along the field direction, linearly polarised when viewed perpendicular to the field and elliptically polarised at viewing angles in between. The π component will be linearly polarised at all angles, in an orthogonal direction to the σ components, except when viewed along the field direction, when the intensity will be zero. Spectropolarimetry is particularly useful for detecting low field

strengths in white dwarfs, when the Zeeman splitting is too weak to fully split the lines. In this case the opposite polarisations of the σ_+ and $\sigma-$ components can be detected in the red and blue wings of the lines.

3. *Magnetic field broadening.* The positions and strengths of the Zeeman-split components of a line are heavily dependent on field strength and direction. Since the field is expected to vary across the surface of the white dwarf, this leads to a broadening of the spectral lines, known as "magnetic field broadening". Another source of line broadening is caused by the splitting of spectral lines in the presence of an electric field, and is known as "Stark broadening". In a stellar context, the field is generated by the electrons and ions in the gas, so the amount of broadening is a measure of the electron density, and therefore pressure and gravity in a star's atmosphere.

4. *Continuum polarisation.* Absorption and scattering processes in the stellar atmosphere are affected by the presence of a magnetic field, and so lead to field- and polarisation-dependent opacities (magnetic dichroism). The level of polarisation of the light emerging from the atmosphere will therefore indicate the presence of a magnetic field. The ratio of linear to circular polarisation can give an indication of field strength - for frequencies below the cyclotron resonance frequency ($B \gtrsim 2 \times 10^8$ G for optical wavelengths), the polarisation will be mainly linear, while for frequencies above the cyclotron frequency, the polarisation will be mainly circular (Martin & Wickramasinghe 1982). It should be noted, however, that the polarisations are somewhat dependent on field direction and radiative transfer effects in the atmosphere. The variation in continuum intensity with field strength and direction can also be used to measure spin periods in high-field isolated magnetic white dwarfs (see Section 1.1.2.3 and Chapter 3).

1.1.2.2 Characteristics of magnetic white dwarfs

There are two possible origins for the fields of magnetic white dwarfs (MWDs): either they are the remnants of the fields of their main-sequence progenitors, amplified by contraction as the star evolved off the main sequence, or the fields are generated by dynamo action during post-main sequence evolution (see Wickramasinghe & Ferrario 2005 for a comprehensive discussion). As the only main-sequence stars with significant magnetic fields are the chemically peculiar Ap and Bp stars, it has generally been assumed that these are the progenitors of MWDs. Typical fields strengths for Ap and Bp stars are $\sim 10^2 - 10^4$ G, but the contraction of the stellar core during white dwarf formation can amplify these fields by about 4 orders of magnitude due to the conservation of magnetic flux, resulting in field strengths comparable to those measured in MWDs. However, it seems that the space density of Ap and Bp stars is not high enough to support the incidence of magnetism observed in white dwarfs, leading to the suggestion that the low-field MWDs may be descended from normal main-sequence stars with as-yet undetected weak magnetic fields (Kawka et al. 2003).

The field structure of magnetic white dwarfs is rarely a centred dipole, but can usually be modelled with an offset dipole structure, where the dipole centre is shifted up or down the axis of rotation of the MWD. The well-studied MWDs (all with temperatures above 10,000 K) all have off-centred dipole or more complex field structures. One of the most extreme MWDs is RE J0317-853, which has the highest temperature (50000 K, Barstow et al. 1995) of any known white dwarf and a very high field strength (340 MG) that can be modelled with an offset dipole. This unusual object also displays large-amplitude variability on a period of 725.4 s, indicative of fast rotation and probably caused by the effect of the magnetic field on the line-of-sight continuum opacity as the star rotates. Despite being able to model the

vast majority of MWD field structures as offset dipoles, there are two cooler stars, WD1953-011 (Maxted et al. 2000) and PG1031+234 (Latter et al. 1987) which have been shown to have spot-like field enhancements.

The study of magnetic white dwarfs as a class is important as the magnetic field may well play a role in the evolution (more specifically, the initial-final mass relation) of white dwarfs. Magnetic white dwarfs tend to have a higher average mass than their non-magnetic counterparts (their distribution peaks between $\sim 0.8 - 0.93\,M_{\odot}$, depending on the sample), which would seem to suggest that the magnetic field may affect the growth of the stellar core during post-main sequence evolution. However, Wickramasinghe & Ferrario (2005) have shown that it is possible for the post-main sequence evolution to be field-independent if we include, as progenitors, stars with mass $M > 4.5\,M_{\odot}$ that are magnetic below the current observational threshold.

The spin periods of white dwarfs, on the other hand, are almost certainly affected by the presence of a magnetic field. While non-magnetic white dwarfs have spin periods of $\sim$ 1 day (Karl et al. 2005; Koester et al. 1998; Heber et al. 1997; O'Brien et al. 1996), their magnetic counterparts seem to display a bimodal distribution, with a few rotating very slowly ($>$ 100 years; a result confirmed recently by Beurmann & Reinsch 2002), and the other group rotating with short periods of order minutes – days. In theory, all WDs should be rotating close to the break-up value, as the conservation of angular momentum during the contraction of the core should cause the white dwarf to "spin up". This implies that there is a very efficient angular momentum transfer from the core to the envelope during post-main sequence evolution. Spruit (1998) suggested that the long-period systems could be created if the magnetic fields lock the WD to its envelope, so quickly shedding angular momentum, while King et al. (2001) proposed that the very fast rotators ($P_{rot} \sim$ minutes) may be spun up during double-degenerate mergers (e.g. RE J0317-853). Ferrario & Wickramasinghe (1997) recently suggested that the high-field magnetic white dwarfs

formed by single-star evolution may display a correlation between field strength and spin period. They also split the MWDs into three identifiable categories: strongly magnetised slow-rotators (P $\sim$ 50 – 100 years) formed by single-star evolution; strongly-magnetised fast rotators (P $\sim$ 700 s) formed through mergers, and a third group of modest rotators (P $\sim$ hours – days) of mixed origin (both single and binary evolution). We investigate this further in Chapter 3.

1.1.2.3 Variability in magnetic white dwarfs

There are 3 temperature regions of instability along the white dwarf cooling track, within which the stars may be seen to pulsate with periods $\sim$100 - 1200 s. For hydrogen-rich DA white dwarfs this region is between $\sim$ 11000 K – 12500 K for log $g \simeq 8$ (Bergeron et al. 1995, Koester & Allard 2000; Mukadam et al. 2004), for the helium-rich DB stars it lies between $\sim$ 22000 – 28000 K (Beauchamp et al. 1999) and for the hot pre-white dwarfs it is above $\sim$60000 K (O'Brien 2000). The instability is observed as non-radial g-mode pulsations and can be used to probe the internal structure of the star. A small number of magnetic white dwarfs are also seen to vary on longer timescales (P $\sim$ hours – days), far too slowly to be linked to the pulsation periods, while others display short-term variability even though their temperatures suggest that they are well outside the instability regions. This type of variability is generally attributed to the rotational period of the star.

Measuring rotational periods in non-magnetic WDs is notoriously difficult due to the heavy broadening of the spectral lines by the strong gravitational field. MWDs on the other hand, display spectroscopic and/or photometric variability which allows much easier identification of their spin periods. Spectroscopic variability is generally caused by variations in the surface field strength, which can be observed in the motion of the Zeeman-split components of the Balmer lines. Photometric variability

is caused by the dependence of the continuum opacity on the surface field strength, called magnetic dichroism (Ferrario et al. 1997), but this requires a high magnetic field strength. Variability may also be caused by low-level accretion of matter onto the MWD from the interstellar medium. Theoretically, low-field MWDs are not expected to display significant photometric variability, but we have observed this in at least two low-field MWDs, as discussed in Chapters 2 and 3 of this thesis. These results are believed to be the first photometric detections of star spots on the surfaces of white dwarfs.

Star spots can be caused by a number of different mechanisms. Accretion onto the white dwarf from the interstellar medium or an undetected binary companion can create either a hot or cooler spot depending on the relative temperature of the white dwarf and accretion stream and the rate of mass transfer. Cooler (and therefore darker) areas may also be caused by surface abundance inhomogeneities if the opacity of heavier elements is enough to block the optical flux (e.g. as in GD 394, Dupuis et al. 2000). For GD 356 and WD 1953-011 we favour the classic star spot theory, analogous to sun spots, which are caused by the inhibition of convection in the stellar atmosphere by the magnetic field. White dwarfs become fully radiative above temperatures of 12 – 14000 K, so MWDs below that temperature should be capable of forming star spots. These areas of reduced convection are cooler (and therefore darker) than the surrounding atmosphere, leading to a drop in the observed magnitude of the star as the spots rotate into view. Previous spectroscopic observations of a number of these stars had failed to reveal variability.

1.2 Binary Systems

Binary stars come in two main types - those where mass is transferred between the component stars, called "interacting binaries," and those where the two components are completely separated, called "non-interacting binaries." If the system components are relatively close to one another (within a few stellar radii, called a close binary system) then evolution of the system tends to drive the component stars closer together, with the non-interacting binaries evolving into interacting ones.

1.2.1 Evolution of close binary systems

The evolution of all close binary systems is governed by angular momentum (AM) loss. In the majority of these systems, this loss is driven by a combination of gravitational radiation (Kraft et al. 1962; Faulkner 1971), which is dominant for periods $P_{orb} < 3\,h$, and magnetic braking (Verbunt & Zwaan 1981), which dominates for $P_{orb} > 3\,h$. Gravitational radiation is relatively well understood, with the angular momentum loss rates simply governed by the masses and separation of the components of the binary system. Magnetic braking, however, is a more complicated issue. The mechanism is driven by the magnetic field and stellar wind of one of the binary components (usually the main-sequence secondary star). As mass is driven off in the stellar wind, the ionised particles are forced to co-rotate with the field lines out to the Alfvén radius. This draws angular momentum away from the star, effectively exerting a braking force to slow its spin. In close binaries, the secondary star is tidally locked to the primary star, so the angular momentum loss cannot act to slow the spin period of the secondary star alone. Instead, the angular momentum is drawn from the binary orbit, causing it to shrink and the orbital period of the binary to decrease. The loss rates generated by magnetic braking are the subject of

much debate, and are discussed in depth in Chapter 4 of this thesis.

1.2.2 Cataclysmic Variables

Cataclysmic variable stars (CVs) are interacting binary stars comprising a white dwarf primary star orbited by a late-type main-sequence secondary star (see Fig 1.2). The lower-mass secondary star is much less dense and has a much larger radius than the compact white dwarf primary star. As the two components evolve to smaller separations, the secondary star becomes distorted by the gravitational pull of the white dwarf, until an outermost part of the secondary star's atmosphere experiences more gravitational force from the white dwarf than from its parent star, and overflows onto the primary star. This is called Roche lobe overflow, where the Roche lobe of a star is an equipotential surface at which mass-transfer can occur. The closest point of the Roche lobe to the primary is called the inner Lagrangian (L1) point, and is the point where the gravitational forces from the two components are balanced. It is through this point that mass-transfer takes place. The material from the secondary star passes through the L1 point in a thin stream, initially moving towards the primary star at roughly the sound speed in the gas. However, the material also has a tangential velocity from the orbital motion of the secondary star that is approximately ten times the radial speed of the stream. Therefore, instead of falling directly towards the primary star, the material settles into an accretion disc around the white dwarf. The material in the accretion disc will gradually lose angular momentum and accrete onto the primary star (Warner 1995, Hellier 2001).

CVs have short periods ($64\,\mathrm{min} < \mathrm{P_{orb}} \lesssim 2\,\mathrm{days}$) and their secondary stars are in rotational lock with the orbital period. Typical white dwarf masses for CVs are $0.5 - 1\,\mathrm{M_\odot}$, and typical separations of the two stars are of order a few solar radii.

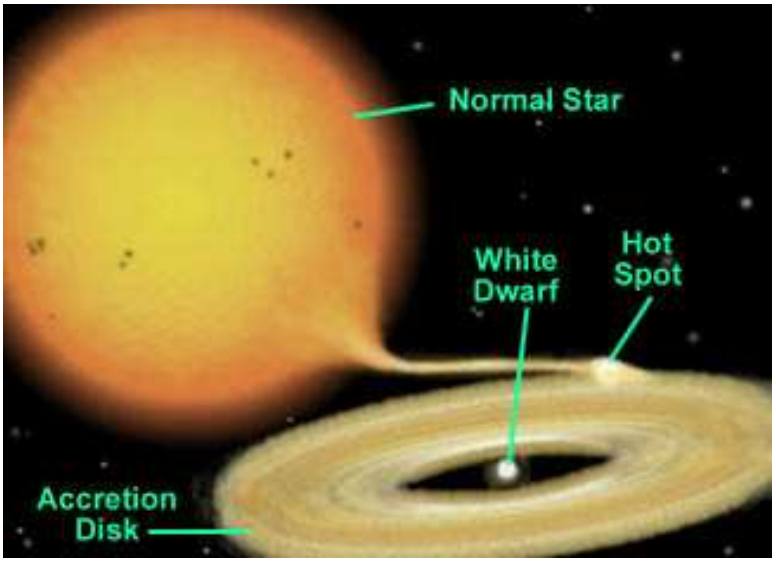

Figure 1.2: Artist's impression of a cataclysmic variable

The progenitors of CVs are close binary systems, with separations of only a few hundred solar radii and $P_{orb} \sim 10$ years. If one star is approximately solar mass, but the other is more massive, the more massive one will evolve off the main sequence and become a red giant more quickly than the other. At this point the more massive star will overflow its Roche lobe and transfer material onto the solar-mass star. This is unstable, as a transfer of material from a more massive star to a less massive star causes the material to be moved further from the centre of mass of the system. In order to conserve angular momentum, the separation of the two stars must decrease, which reduces the size of the Roche lobe and instigates more mass transfer. This positive feedback results in a runaway transfer of mass from the red giant, and its entire envelope is dumped onto the main-sequence star, overflowing its Roche lobe and creating a "common envelope" around the whole system.

The envelope acts as a drag force on the two stars, which lose angular momentum to the cloud, expelling it from the system but at the same time decreasing their separation. This process can cause a decrease in orbital separation from ~ 100 $R_\odot$ to ~ 1 $R_\odot$ in around 1000 years. Eventually the entire envelope is thrown off as a

planetary nebula, leaving the WD-MS star binary. If the separation of the two stars is small enough, this binary has the potential to evolve into a cataclysmic variable, and is called a pre-CV.

As a pre-CV finally evolves to a short-enough period, the remaining main-sequence star will start to overflow its Roche lobe, causing mass transfer onto the white dwarf. In this case the less massive star is losing mass onto the more massive star, so the overflowing material is moving closer to the centre of mass of the system. In the absence of angular momentum losses, the separation of the binary must increase slightly to conserve AM, causing the star to detach from its Roche lobe and mass transfer to stop. This type of mass transfer is stable, but cannot be the whole story, since CVs are observed to undergo steady mass transfer, without continually cutting off.

Steady mass transfer can occur in two ways. Firstly, if the secondary star is evolving off the main sequence, it will be in the process of expanding to become a red giant. If the star is expanding, it will remain in contact with its Roche lobe and continue to transfer mass, despite the increase in separation of the two stars. Obviously only a small fraction of CVs will contain evolving secondaries, so there must be another mechanism at work in those with main-sequence secondaries. The accepted model is a combination of the two angular momentum loss mechanisms discussed in Section 1.2.1.

1.2.3 Orbital period distribution

The distribution of CV orbital periods is shown in Fig 1.3 (Kolb et al. 1998). There are several important features of this distribution. The first is the long period cutoff at about $P_{orb} > 12$ hours. This is limited by the mass of the secondary star,

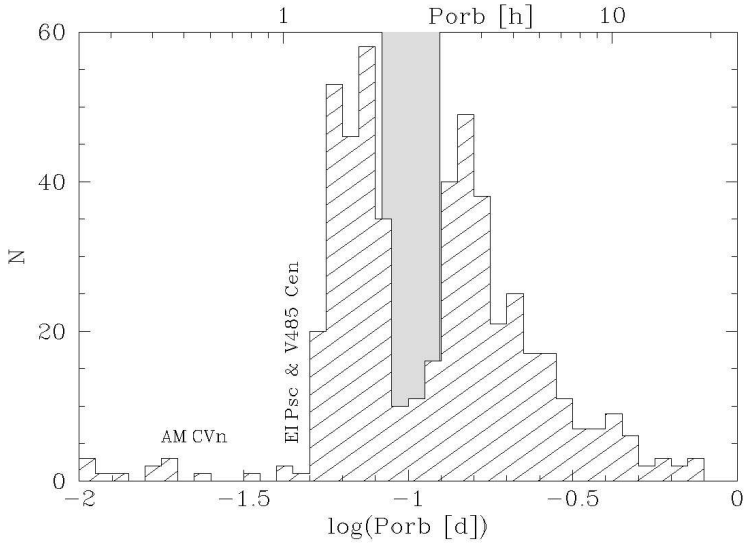

Figure 1.3: Orbital period distribution of CVs. There is a short period cut off at around 78 mins, a long period cut off at about 12 hours and the period gap between 2 and 3 hours (Kolb et al. 1998).

which must be less massive than the WD to maintain stable mass transfer. As P_{orb} increases, the separation increases, so the secondary star mass must increase to maintain contact with its Roche lobe. As the mass of the white dwarf must be less than the Chandrasekhar mass ($M \leq 1.4\,M_{\odot}$), so must the mass of the secondary, limiting the orbital period to ~ 12 hours. The few systems with longer periods can be explained if the secondary star is evolving into a red giant, making it larger but less massive than a star on the main sequence.

The second feature of the distribution is the period gap between $2 - 3$ hours. In the standard model of CV evolution, this is explained by a shutdown of magnetic braking as the system reaches a period of 3 hours. As the secondary star loses mass to the primary star its mass is reduced, so the gravitational pressure on the core decreases and the nuclear reactions slow down. Less energy is generated by the secondary star so the radiation pressure drops and the star contracts to maintain hydrostatic equilibrium. This contraction occurs on the Kelvin-Helmholtz timescale. If this is longer than the mass-transfer timescale then the star cannot adjust quickly

enough to the mass transfer and finds itself with a radius greater than equilibrium for its mass. The star will therefore contract back to its equilibrium radius, halting mass transfer until the system evolves to a separation small enough to re-start it. Why this should happen at $P_{orb} \sim 3$ hours is still a matter of debate, but the star becomes fully convective at the mass corresponding to a 3-hour binary, so it is hypothesised that this might cause a disruption of the magnetic field. The most widely accepted theory is that the restructuring of the star destroys the radiative-convective boundary that anchors the base of the magnetic field. If the field lines are not anchored then particles from the stellar wind are no longer forced to co-rotate with the star, so destroying the mechanism for magnetic braking. Evolution down to $P_{orb} \sim 2$ hours would therefore occur by gravitational radiation while the binary is detached, before the secondary star comes back into contact with its Roche lobe at $P_{orb} \sim 2$ hours and mass transfer is re-established.

The final main feature in the distribution is the period minimum at about 78 mins. This occurs when the mass of the secondary star is so low that the star becomes degenerate. In this state, mass-loss causes the radius of the star to *increase*. Therefore, as mass is lost the binary radius expands slightly, but the secondary star's radius *increases*, so the system will now evolve to longer periods. This is called the "period bounce".

1.2.4 Eclipsing Binaries

One of the most useful types of binary system, from a scientific point of view, is the eclipsing binary. This is where the secondary star passes between the primary star and the observer, causing a temporary drop in the measured light flux from the system. The flux as a function of time is called the binary light curve and can be used to derive a large amount of information about the system components.

The light curve alone can only provide information about the relative values for the system parameters, but when combined with radial velocity information, it is possible to derive the absolute values.

The light curve of an eclipsing binary, NN Ser, (binned by a factor of 30 for clarity) is shown in Fig. 1.4.

The first piece of information we can take from the light curve is the orbital period of the binary. The large drop in light from the system, seen as a deep trough in the light curve at phase 0, is the point at which the secondary star passes in front of the hot, white dwarf primary star, eclipsing its light. We can therefore use the time between these eclipses to test for changes in the orbital period of the system. We expect close binary systems to naturally evolve to shorter periods as the system loses angular momentum, although measured changes in eclipse timings can also be attributed to other mechanisms, as discussed in detail in Chapter 4.

The primary eclipse itself can be used to find the relative radii of the binary components. The length of the eclipse is the time it takes for the secondary star to pass in front of the primary star, and is therefore a measure of the secondary star's diameter, while the time it takes for the system to go from un-eclipsed to minimum light (the ingress time) is a measure of the diameter of the white dwarf. If we combine these times with the radial velocity information on the speed of the stars in their orbit, we can calculate the absolute radii. The radii derived for the components depend upon the assumption that the widest part of the secondary star passes in front of the white dwarf, i.e. that the inclination of the system is 90°. If the inclination is smaller than this, the true radius of the secondary star will be larger than the calculated value, while the true radius of the white dwarf will be smaller.

NN Ser also shows a bump in the light curve between eclipses. This is due to

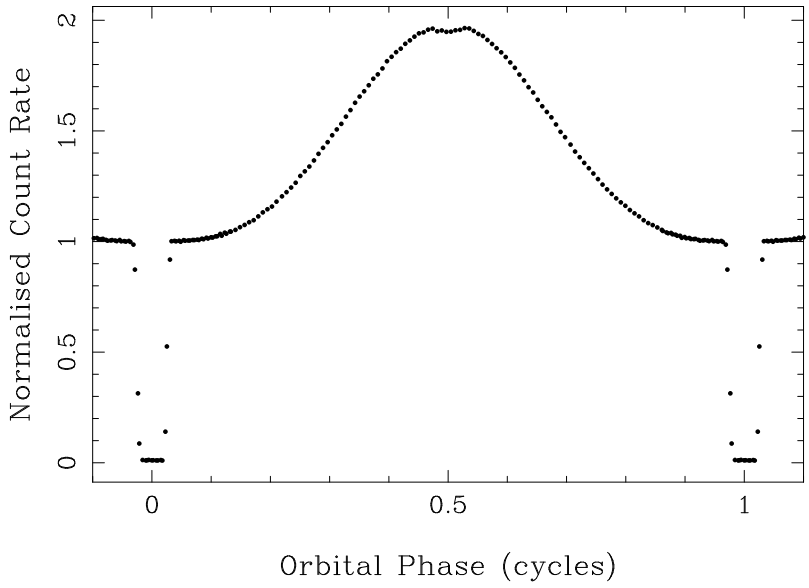

Figure 1.4: Example of an eclipsing binary light curve. See Section 1.2.4 for explanation

the *reflection effect*, where one face of the secondary star is heated by the radiation from the white dwarf. This radiation is reprocessed and emitted by the secondary star, and is seen as an increase in flux whenever the irradiated face is visible.

Finally, this light curve, taken with ULTRACAM, shows a small dip at the top of the reflection effect bump, at phase 0.5. This is the secondary eclipse as the white dwarf passes in front of the much larger, but much cooler, secondary star. This can be used to estimate the inclination of the system and more tightly constrain the radii of the stars.

In order to achieve good estimates for the system parameters, it is important to measure the timings of the eclipses as accurately and precisely as possible. By using a new ultra-fast CCD camera called ULTRACAM, we have been able to improve the time resolution for NN Ser's light curve to 2.06 s, far better than had been previously achieved. An overview of ULTRACAM can be found in Section 1.3.1

1.3 Data collection

The data contained in this thesis were taken from two sources. Chapters 2 and 3 are based on photometric observations of relatively bright (V = 13 – 17 mag) isolated magnetic white dwarfs. These observations were taken using the 1.0 m Jacobus Kapteyn Telescope, which was part of the Isaac Newton Group of telescopes at the Observatorio del Roque de los Muchachos of the Instituto de Astrofisica de Canarias. The data were all collected using the SITe1 CCD chip, which is 2088 × 2120 pixels in size, with readout noise = 6 e and gain = 1.9 e/ADU. The pixel size is 15μm and the image scale is 0.33"/pix.

The data contained in Chapter 4 were collected using the 4.2m William Herschel Telescope, also run by the Isaac Newton Group, combined with the high-speed CCD camera ULTRACAM.

1.3.1 ULTRACAM

ULTRACAM is an ultra-fast, triple-beam CCD camera designed by Vik Dhillon and Tom Marsh (see Dhillon & Marsh 2001 for an extensive review). It was designed to study one of the relatively unexplored regions of parameter space - high temporal resolution. By using ULTRACAM we were able to observe our target at high time resolution, in three different wavebands simultaneously. The optical layout of ULTRACAM can be seen in Fig 1.5 and comprises four separate stages - the collimating fore-optics, to collimate the light from the telescope; the dichroic beamsplitters to split the incoming light into blue, green and red wavebands; the filters, using the Sloan filter system u', g' and a choice of r', i' or z'; and the re-imaging lenses to re-focus the filtered light onto the CCDs. The CCDs themselves are back-illuminated frame-transfer chips, cooled by a peltier-device and water cooler. The exposed area

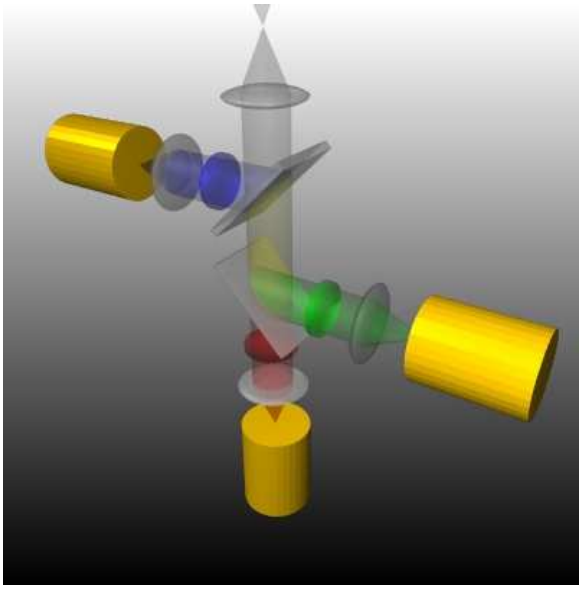

Figure 1.5: Optical layout of ULTRACAM.

is 1024 × 1024 pixels, with pixel size = 13μm and a scale of 0.3"/pix. The readout noise is 3.10 – 3.40 e, depending on the CCD, while the gain is 1.13-1.20 e/ADU. The frame-transfer chips enable data to be taken in the exposed area, while the previous frame in the masked area is being read out. This means that, for small windows, ULTRACAM can take 0.0017 s exposures with a dead-time of only 0.0001 s. For our target (V $\simeq$ 15 mag) we achieved a time resolution of $\sim$ 2.06 s.

1.3.2 Data reduction with ULTRACAM

Most of the data in this thesis were reduced using the ULTRACAM pipeline software developed by T. R. Marsh. The data from ULTRACAM are stored in two files - a .xml file containing information about the data format, and a .dat file containing all the raw data. The pipeline software can either work with these two files, or each run can be split into individual image (.ucm) files and processed separately. The ULTRACAM software can also be used with data from other telescopes, e.g.

the JKT. Files in .fits format can be converted into .ucm format and processed in exactly the same way as individual ULTRACAM files.

The main element of the ULTRACAM software is the reduce file, which sets up the parameters for data reduction. This file can be edited to change the aperture settings, extraction method, profile fitting parameters, sky estimation method, noise parameters and calibration files (dark frame, bias frame, flat-field frame and bad pixel mask). In order to extract the photometry from the data frames, an aperture (.ape) file must be set up containing the positions and sizes of all the apertures in a particular frame. This is then called by the reduce file when running the reduction.

There are two options for the aperture type - either fixed or variable. Fixed apertures are fixed in size, regardless of the conditions or profile of the target. Variable apertures are allowed to vary in size according to the FWHM of the fitted profile to a selected star in the frame. This means that we can compensate for changes in the observing conditions throughout the run.

There are also two types of extraction method available - normal and optimal. Normal extraction simply means that all of the counts within the aperture are added up and output in counts per second. The alternative is to use Tim Naylor's optimal extraction (Naylor 1998) which weights the extraction according to the fitted profile of the target. This gives a noticeable improvement in the photometry of weak signals, but in practice we have found that it tends to make the photometry of high signal-to-noise targets worse.

Once the reduce and aperture files have been set up, the reduction can be run on a whole list of files. The apertures are re-centred on their stars in each frame, with the permitted shifts in position from one frame to the next defined by the user in the reduce file. The extracted photometry is output in a .log file, with the GPS timestamp for each frame expressed in MJD and accurate to 1 μs. The photometry

is recorded in counts per second.

More information regarding the ULTRACAM software can be found at Tom Marsh's website, currently at:

http://quetzel.csc.warwick.ac.uk/phsaap/software/ultracam/docs/index.html.

Chapter 2

Star spots on magnetic white dwarfs: WD 1953-011 & GD 356

2.1 Introduction

Variability in isolated white dwarfs is almost exclusively due to pulsations of the stars with periods $\sim 100 - 1200$ s as they pass through instability strips during their evolution (e.g., Mukadam et al. 2004). Longer-period variability, which may be indicative of rotation, is not especially common as the spectral lines usually used to detect rotation are heavily gravitationally broadened (although the sharp H_α NLTE cores of hydrogen-rich DA white dwarfs can still be used), and the surfaces of white dwarfs are virtually featureless. In isolated magnetic white dwarfs (MWD) however, spectroscopic, polarimetric and photometric variability is relatively common as the photometric flux and spectral lines are affected by the change in magnetic field strength across the visible surface of the star. While spectroscopic and polarimetric variability is relatively sensitive even to low fields, photometric variability in MWDs is thought to be caused primarily by the dependence of the continuum opacity on the

field strength. This requires a high field strength before the opacity is sufficiently affected to cause a measurable change in flux. Low-field magnetic white dwarfs are therefore not expected to display significant photometric variability. Here we present photometry of two low-field MWDs - WD 1953-011 and GD 356, both of which are shown to be variable at levels $\sim$2% [1]. Since their fields are too low to cause magnetic dichroism, we believe that the variability is caused by the presence of star spots on the surface of the white dwarfs, which cause periodic changes in flux as they rotate in and out of the line of sight.

2.1.1 WD 1953-011

WD 1953-011 is an isolated magnetic white dwarf with observations spanning several decades. It is one of the closest MWDs to Earth ($\sim$12 pc, Harrington & Dahn 1980), but is relatively cool (7920 ± 200 K, Bergeron et al. 2001) and therefore quite faint (V = 13.7 mag). There have been many attempts to measure the magnetic field strength of WD 1953-011, but the differences in the results from each attempt suggested that the field structure was probably quite complex. Circular polarimetry by Schmidt & Smith (1995) gave a mean longitudinal field strength of 15.1 ± 6.6 kG, observations of the narrow H_α core by Koester et al. (1998) revealed a narrow Zeeman triplet consistent with a mean field strength of 93 ± 5 kG and Maxted & Marsh (1999) observed broad depressions in the wings of the H_α line that indicated a mean surface field strength of ~ 0.5 MG. The field structure was finally mapped by Maxted et al. (2000), who discovered variations in the equivalent width of the Balmer lines, unusual in a low-field white dwarf. Modelling of these variations revealed a complex field structure, with a strong (~ 500 kG) spot-like field superimposed on a weaker (~ 70 kG) dipolar distribution.

[1] Published in Monthly Notices of the Royal Astronomical Society, Brinkworth et al. (2004, 2005)

In 2001 we began a photometric campaign to search for variability in the BVRI broad bands and the narrow H_β band. Here we present the results and derive a rotational period for WD 1953-011 of 1.44 days.

2.1.2 GD 356

GD 356 (B = 13 MG, $T_{\rm eff}$ = 7500 K) is unique among magnetic white dwarfs in showing resolved Zeeman triplets of H_α and H_β in *emission* (Greenstein & McCarthy 1985). Detailed modelling of spectropolarimetric observations by Ferrario et al. (1997) points to the existence of a latitudinally extended spherical sector or strip covering approximately 10% of the stellar surface, over which the stellar atmosphere has an inverted temperature distribution in its outer layers. This small region is most likely the site of origin of the emission lines.

The cause of this temperature inversion is a mystery, especially as there is no evidence for a low-mass close, stellar companion from which GD 356 could be accreting. Ferrario et al. (1997) investigated the most obvious interpretation, chromospheric activity, but the evidence for a very localised emission region, and the absence of evidence for such a phenomenon in other similar magnetic white dwarfs argues against such an interpretation. Ferrario et al. (1997) also considered a model invoking Bondi-Hoyle accretion (accretion from the surrounding interstellar medium, Bondi & Hoyle 1944), but this interpretation remains unsatisfactory due to a lack of detectable X-ray emission (see Section 2.5.4.2).

Other authors have considered more exotic explanations for the presence of Zeeman-split emission lines in GD 356. For example, Li et al. (1998) suggest that an Earth-like planet, orbiting through the magnetic field with a period of a few hours, might heat the white dwarf's atmosphere near the poles via the generation of

electrical currents, as in the Jupiter-Io system. Alternatively, following the work of Zheleznyakov & Serber (1995), Gnedin et al. (2001) propose that in the regions of the magnetic poles, cyclotron radiation pressure exceeds the local force of gravity, driving a plasma jet into the magnetosphere. The emission lines may be formed in this outflowing plasma. Crucially, none of these models were able to utilise information about the rotation period of GD 356, since no evidence for rotation had previously been detected. Ferrario et al.'s multi-epoch spectropolarimetry appeared to rule out rotation in the period range $\sim$1h – 3 years, and a lack of variability in Gnedin et al.'s long-term spectropolarimetric observations led them to conclude that the rotation period of GD 356 exceeds 5 years. Indeed, Ferrario et al. (1997) admit that the details of the star's underlying field geometry are difficult to ascertain with any certainty given the data available to them, especially a lack of rotational modulation.

After our success with detecting photometric variability in WD 1953-011, we began a survey of isolated white dwarfs (see Chapter 3) to determine whether photometric variability was common, and to see whether we could find evidence for star-spots on any other cool, low-field white dwarfs. GD 356 was one of these systems, and is found to be variable at a 2% level, with a modulation period (which we again interpret as the spin period) of 0.0803 days. Again, we believe that the variations are caused by a star spot on the surface of the white dwarf, which also seems likely to be the site of the Zeeman emission.

2.2 Observations

2.2.1 WD 1953-011

We observed WD 1953-011 at 7 epochs between July 2001 and May 2003. In total we obtained 900 observations in the V band. The data were all taken using the 1 m Jacobus Kapteyn Telescope on La Palma. A full list of V band observations is given in Table 2.1, although we also took data in B, R and I broad bands and H_β narrow band during the July 2001 run. As the results of the photometry were found to be almost identical in all of the bands, we restricted the subsequent observations to V band only. The SITe1 CCD chip is 2088 x 2120 pixels, with readout noise = 6 e and gain = 1.9 e/ADU. The pixel size is 15μm and the image scale is 0.33"/pix.

2.2.2 GD 356

We observed GD 356 at 3 epochs, in August 2002, February 2003 and May 2003, again using the 1.0 m Jacobus Kapteyn telescope and the SITe1 CCD chip. The observations were all taken using a V Harris filter with a typical exposure time of 60 – 90 s. The chip was windowed to improve the readout time for the August and May runs, but not for the February run due to problems with handling windows in TRM's ULTRACAM reduction software at the time. See Table 2.2 for a full list of observations.

Table 2.1: List of observations of WD 1953-011 taken with the JKT on La Palma. Observers: C. S. Brinkworth CSB, T. R. Marsh TRM, L. Morales-Rueda LMR, M. R. Burleigh MRB, S. A. Good SAG

Dates	Filter	Exp (s)	No. of obs	Observer	Conditions
05/07/01	V Kitt	40	14	TRM	Good
06/07/01	V Kitt	40	18	TRM	Fair
07/07/01	V Kitt	40	19	TRM	Superb
08/07/01	V Kitt	40	6	TRM	Poor seeing
09/07/01	V Kitt	40	9	TRM	Good
10/07/01	V Kitt	40	12	TRM	Good
11/07/01	V Kitt	40	12	TRM	Good
14/05/02	V Harris	40	30	MRB,SAG	Cirrus
15/05/02	V Harris	40	45	MRB,SAG	Good
16/05/02	V Harris	40	25	MRB,SAG	Variable
17/05/02	V Harris	40	40	MRB,SAG	Good
26/05/02	V Harris	60	15	TRM,CSB	Good
27/05/02	V Harris	60	10	TRM,CSB	Good
28/05/02	V Harris	60	20	TRM,CSB	Cirrus
29/05/02	V Harris	60	20	TRM,CSB	Cirrus
30/05/02	V Harris	60	30	TRM,CSB	Cirrus
31/05/02	V Harris	60	20	TRM,CSB	Good
01/06/02	V Harris	60	20	TRM,CSB	Good
15/07/02	V Harris	60	26	LMR	Good
16/07/02	V Harris	60	36	LMR	Good
17/07/02	V Harris	60	11	LMR	Good
18/07/02	V Harris	60	25	LMR	Good
19/07/02	V Harris	60	27	LMR	Good

Table 2.1: continued

Dates	Filter	Exp (s)	No. of obs	Observer	Conditions
20/07/02	V Harris	60	29	LMR	Good
21/07/02	V Harris	60	34	LMR	Good
02/08/02	V Harris	60	5	MRB,CSB	Good
03/08/02	V Harris	60	20	MRB,CSB	Good
04/08/02	V Harris	60	15	MRB,CSB	Good
05/08/02	V Harris	120	15	MRB,CSB	Some cirrus
06/08/02	V Harris	40	15	MRB,CSB	Superb
07/08/02	V Harris	60	5	MRB,CSB	Good
10/09/02	V Harris	60	30	TRM	Good
11/09/02	V Harris	60	24	TRM	Cirrus
12/09/02	V Harris	60	32	TRM	Superb
13/09/02	V Harris	60	40	TRM	Some cirrus
15/09/02	V Harris	100	20	TRM	Poor seeing
08/05/03	V Harris	60	3	LMR	High cloud
09/05/03	V Harris	60	4	LMR	Good
10/05/03	V Harris	60	5	LMR	Good
11/05/03	V Harris	60	5	LMR	Poor seeing
12/05/03	V Harris	60	5	LMR	Good
13/05/03	V Harris	60	5	LMR	Good
14/05/03	V Harris	60	5	LMR	Good
15/05/03	V Harris	60	5	LMR	Good
16/05/03	V Harris	60	10	LMR	Twilight
17/05/03	V Harris	60	8	LMR	Twilight
18/05/03	V Harris	60	5	LMR	Variable seeing
20/05/03	V Harris	60	6	LMR	High cloud

Table 2.1: continued

Dates	Filter	Exp (s)	No. of obs	Observer	Conditions
21/05/03	V Harris	60	5	LMR	Good
22/05/03	V Harris	60	5	LMR	Dusty
23/05/03	V Harris	60	5	LMR	Good
25/05/03	V Harris	60	5	CSB, MRB	Good
26/05/03	V Harris	90	5	CSB, MRB	Superb
27/05/03	V Harris	60	5	CSB, MRB	Superb
28/05/03	V Harris	60	10	CSB, MRB	Clear but dusty
29/05/03	V Harris	60	5	CSB, MRB	Good
30/05/03	V Harris	60	5	CSB, MRB	Good
31/05/03	V Harris	60	10	CSB, MRB	Superb

2.3 Data reduction

We had intended to use TRM's ULTRACAM reduction and analysis software to reduce and analyse the data for both of our targets, but the software was not completed in time to be used for WD 1953-011. These data were therefore reduced using the Starlink packages, and analysed using TRM's PERIOD package.

2.3.1 WD 1953-011

Each of the seven data sets were reduced in the same way using the packages FIGARO and KAPPA. First the bias frames from a run were combined to form a

Table 2.2: List of observations of GD 356 taken with the Jacobus Kapteyn Telescope on La Palma.

Date (dd/mm/yy)	Exp (s)	No. of obs	Conditions
01/08/02	60	45	Clear, seeing 1.5"
03/08/02	60	10	Clear, seeing 0.7-1"
04/08/02	60	10	Clear, seeing 0.8-1.3"
05/08/02	90	15	Variable. Seeing 0.7-1.5"
06/08/02	60	55	Clear, seeing 0.7"
07/08/02	60	31	Clear, seeing 0.8"
21/02/03	120	34	Clear, seeing 1.4-2"
22/02/03	90	20	Cirrus, seeing 2"
25/02/03	60	27	Clear, seeing 1-1.2"
26/02/03	90	28	Clear, seeing 1.5"
25/05/03	85	66	Clear, seeing 1"
27/05/03	120	50	Clear, seeing 1"
30/05/03	120	40	Clear, seeing 1"
31/05/03	120	50	Clear, seeing 0.8"

master bias for the whole run. This was subtracted from all other frames. The flats were then checked, and those with mean counts of less than 7000, or greater than 35000 were discarded. We were concerned that there may be a problem with the flat fields at short exposure times, caused by the shutter speed allowing the centre of the chip to be exposed for a longer time than the edges. This was potentially important as the variation we were trying to measure between the target and comparisons was small - of order 2%. The flats were checked by dividing those of different exposure time by each other, and we found a gradient peaking in the centre of the chip. However, this effect was only seen in the September 2002 data, and was not only confined to the very low exposure times (< 2 s) as we were expecting, but affected flats with exposures of up to 20 s. We suspect that this was caused by a loose filter moving with respect to the chip, but that these variations smoothed out over long exposure times. We therefore only used flats with exposure times of > 20 s to generate the master flat.

A single master flat was generated for each run in an attempt to remove systematic variations from night to night. This was not possible for the July 2001 run, as the first night's data was taken on a different part of the chip to the rest of the run, and there were no full-frame flats. Therefore the first night of that run is flat-fielded with a different master flat to the other 6 nights. The first May 2002 run was flat-fielded with dome flats as there were no sky flats available. All of the dome flats had exposure times of 10 seconds. The second May 2002 run had target frames with a mixture of fast and slow readout speeds. We therefore used two different master flats, one for the fast readout frames and one for the slow. The May 2003 run occurred during a very dusty period, hence the flats changed nightly. This run was therefore flat-fielded with an individual master flat for every night.

Once the master flats had been divided from the target frames, we performed aperture photometry using AUTOPHOTOM, part of the Starlink PHOTOM pack-

age. This was performed with several different apertures to determine the optimum aperture radius of 4 pixels. The sky background was taken from an annulus around the target stars, the measurement errors were estimated from sky variance, and the sky background level was estimated using the clipped mean of the pixel values in the annulus.

Results were output in counts. Once we had compared the comparison stars and established that they were not varying with respect to each other, we combined their fluxes to give us one bright comparison star, and divided the target photometry by the newly generated comparison star to give us differential photometry of the target.

The July 2001 data had been taken with the Kitt Peak V filter, while the rest of the data was taken with the Harris V filter. We corrected for this by integrating models for a cool white dwarf (for the target) and a G-type main-sequence star (for the comparisons) through both filter responses, and multiplying the July 2001 data by the ratio. The correction to the differential photometry only amounted to a factor of 0.9974.

All times were corrected to heliocentric Julian date.

2.3.2 GD 356

The data were all reduced using TRM's ULTRACAM pipeline software. Bias frames for each night were combined to create a master bias, which was then subtracted from all other frames. Sky flats were then checked, and any with counts of less than 10000 or greater than 35000 were discarded. The remaining flats were combined to create a master flat for each night that was normalised and used to flat-field the target frames. There were no sky flats for the 22nd, 25th or 26th of February so the target frames from those nights were flat-fielded using combined dome flats.

Differential photometry was performed on the target with respect to 2 bright comparison stars in the field. Once we had established that neither was varying, we then used the data that was reduced with respect to the brightest comparison. Results were output in differential magnitudes.

2.4 Analysis and Results

2.4.1 Determining the periods

For each of the targets, we used a "floating mean" periodogram (e.g., Cumming et al. 1999; Morales-Rueda et al. 2003) to determine the period of each epoch separately, and all of the data together. This is a generalisation of the Lomb-Scargle periodogram (Lomb 1976; Scargle 1982) and involves fitting the data with a sinusoid plus constant of the form:

$$A + B\sin[2\pi f(t - t_0)],$$

where f is the frequency and t is the observation time. The advantage over the Lomb-Scargle periodogram is twofold - it takes the errors on the data points into account, and treats the constant, A, as an extra free parameter rather than fixing the zero-point and then fitting a sinusoid, i.e. it allows the zero-point to "float" during the fit. The resultant periodogram is an inverted χ^2 plot of the fit at each frequency. For each target, periodograms of the individual epochs and all of the data combined can be seen in Figs 2.1 & 2.5.

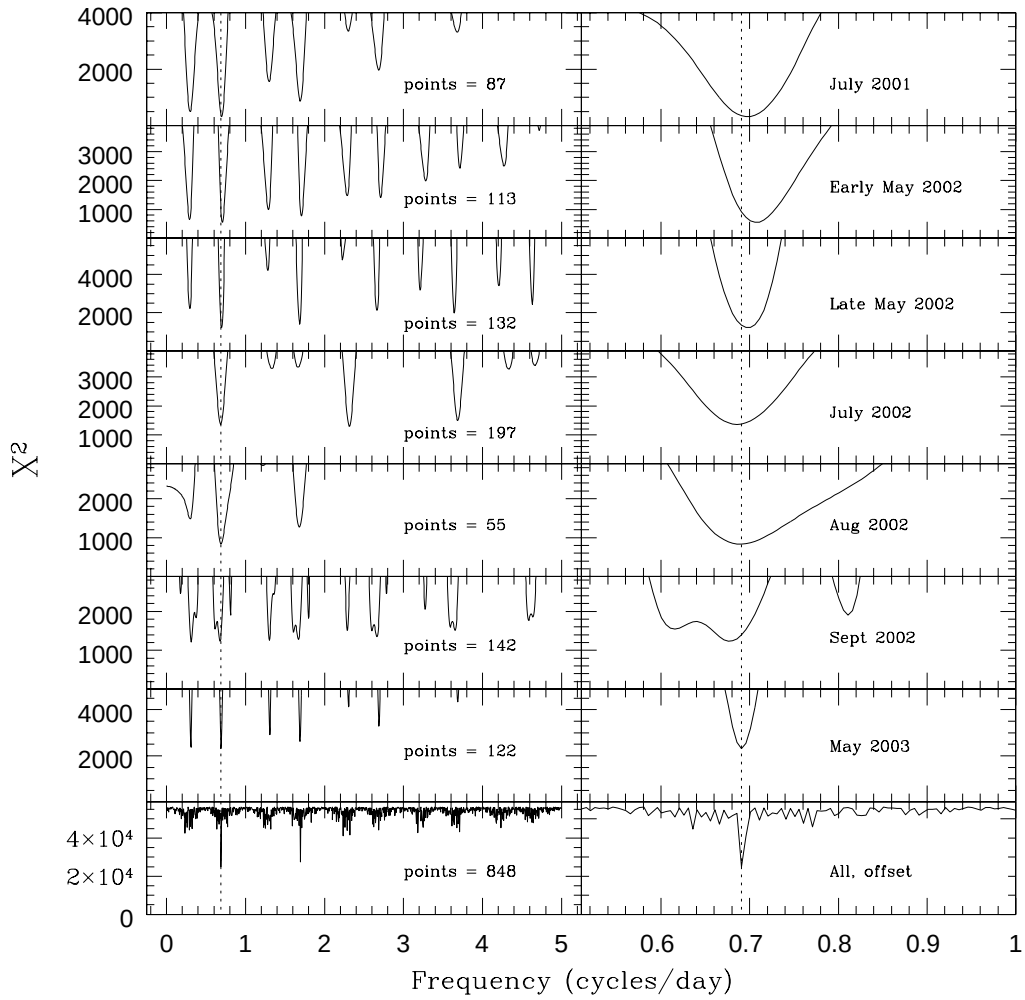

Figure 2.1: WD 1953-011: periodograms for all of the 7 data sets, and all of the data with the average flux at each epoch set to zero (bottom). A period of approximately 1.4418 days is favoured (vertical dotted line). The expanded plots seem to show a slight shift in the best-fitting period (see Fig. 2.4 and Section 2.4.2)

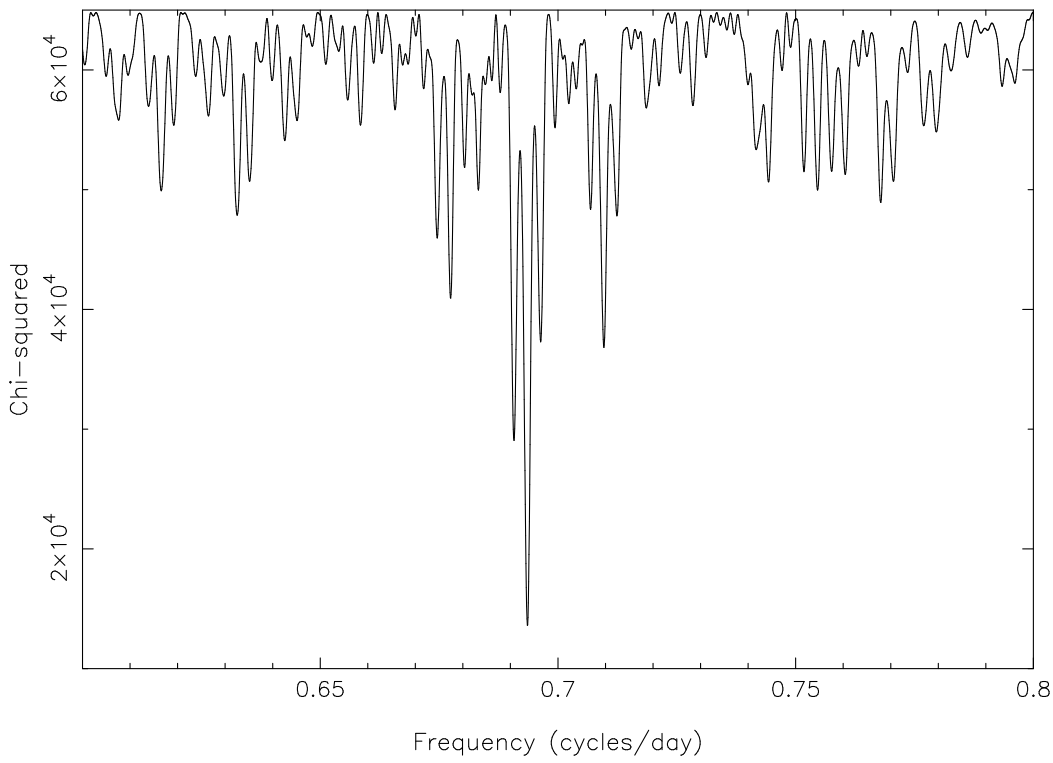

Figure 2.2: WD 1953-011: periodogram zoomed in on the best-fitting period of 1.44176 days (0.6935 cycles/day).

2.4.2 Uncertainties in the periods

2.4.2.1 WD1953-011

The errors output by the packages are the formal statistical errors, but due to the high signal-to-noise ratio they are likely to be underestimates of the actual errors due to e.g. anomalies in the flat fields, aperture edge effects, and so on. We therefore obtained an independent estimate of our errors by bootstrapping our data. We fit the data for each epoch with a sine wave, then resampled the data, randomly selecting the same number of points and re-fitting with the sine wave (resampling with replacement, Diaconis & Efron 1983). This was repeated 500000 times. The resultant period distributions can be seen in Fig. 2.3. In order to avoid excessive weighting of a few data points, the errors were set to a standard average value before bootstrapping. The bootstrapping seems to indicate that there is a small change in the best-fitting period between each epoch. To test the robustness of this result to night-to-night systematic zero-point shifts we repeated the bootstrap runs after adding flux offsets to each night. The offsets were added as Gaussian random variables. We found that an RMS offset in differential flux of only 0.003 caused enough of a spread in the period distributions that the period shift between each epoch was no longer significant. As such a shift could be caused by anomalies in the flat fields, irregularities in the chip or by slight variations in the standard stars, we conclude that there is no evidence for a period change in WD 1953-011 in our data. Despite the slight variations in the best periods at each epoch, the overall value of the rotational period is based on a very long (3 year) baseline of observations, so we expect it to be an accurate measure of the actual spin period of this star.

The phase-folded light curve (Fig. 2.4) shows a variation in the flux of $\pm 1\%$. Fig. 2.1 shows the periodograms for each epoch, showing that the deepest minimum in χ^2 for all but one data set, and the only minimum common to all epochs, is that

at approximately 0.69 cycles per day, corresponding to:

$$HJD = 2452489.3588(9) + 1.441769(8)E$$

which specifies the time of minimum light. The zero-point was selected to give the minimum correlation between it and the fitted period. The light curve also appears to be slightly non-sinusoidal at the level of 1 – 2 mmag in the 1st harmonic. There initially appear to be several sharp features in the folded light curve, most notably at phase 0.4. However, all of these outlying points are from single nights during either the first May 2002 or the July 2002 run. As these features are not seen at any of the other epochs, we suspect that they are not significant features in the WD 1953-011 light curve.

2.4.2.2 GD 356

For GD 356, there is a small offset in differential magnitude between each epoch which may be a sign of a second, longer-term, variability, but more data will be required to verify this result. In order to obtain a clearer periodogram for the short-term variation, we removed this long-term variation by offsetting the average y value of each dataset to zero, hence the August, February and May data sets were offset in y by -0.208, -0.206 and -0.204 differential magnitudes respectively. The bottom panel of Fig 2.5 shows the periodogram for all the data when the long-term variation has been removed. As the standard error estimates output by the ULTRACAM software are likely to be underestimated due to the relatively high signal-to-noise of the data, the error bars for this last data set were re-scaled by adding 0.001 in quadrature to the quoted errors to bring the reduced χ^2 down to 1. This data set was then used to generate the best-fit period and ephemeris.

Two periods were found to be significantly ($\Delta\chi^2 > 60$) better than the rest (see Fig 2.6):

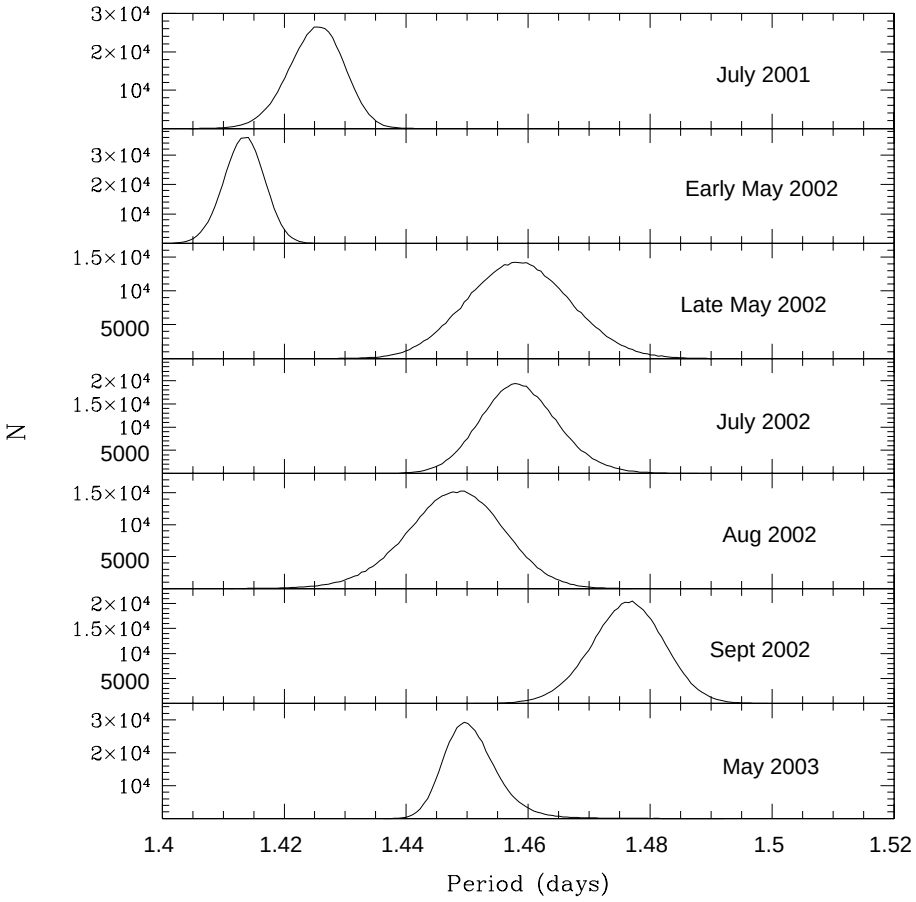

Figure 2.3: Period distributions for all 7 data sets after bootstrapping 500000 times and plotting over 200 bins (see Section 4.2).

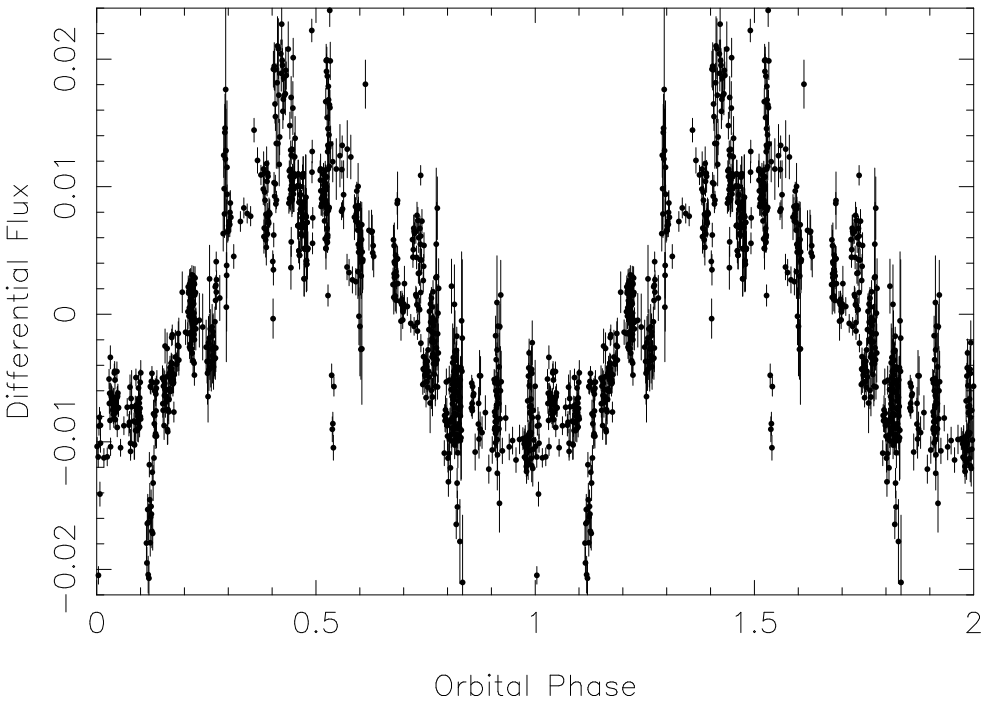

Figure 2.4: WD 1953-011: All of the data folded on the best-fitting period of 1.44176 days.

$$HJD = 2452715.07580(5) + 0.0803000(7)E$$

and

$$HJD = 2452715.97555(5) + 0.0803652(3)E,$$

where the ephemeris given is the point of minimum light for which the correlation between the fitted zero point and period is at a minimum.

We were fortunate enough to observe an entire spin cycle of this target, which has allowed us to select the shorter period as the correct alias. This period is already marginally favoured in the periodogram as its χ^2 is 4 less than that of the longer period.

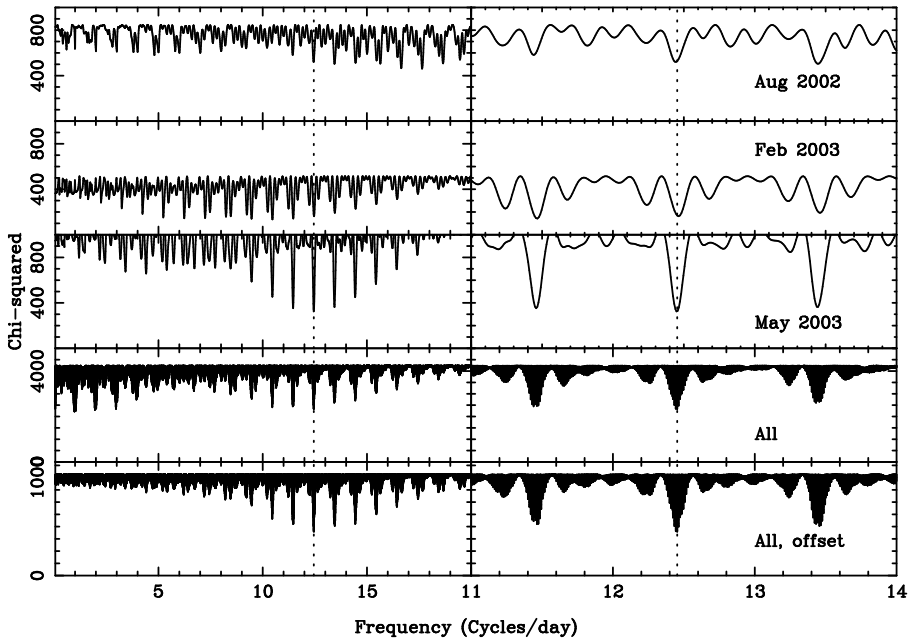

Figure 2.5: GD 356: periodograms for all of the data sets. Panel 1: August 2002. Panel 2: Feb 2003. Panel 3: May 2003. Panel 4: all data. Panel 5: all data, with the average y value of each set offset to zero, removing slight variations in the differential magnitude between each epoch (see Section 2.3). A period of 0.080300 days is favoured (dotted line).

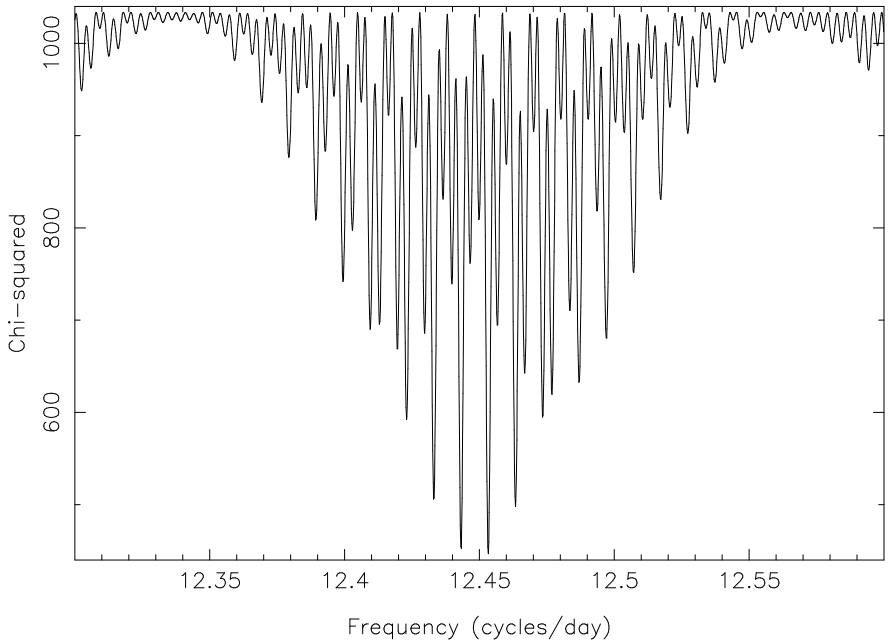

Figure 2.6: GD 356: periodogram zoomed in on the best fitting period of 12.4533 cycles/day.

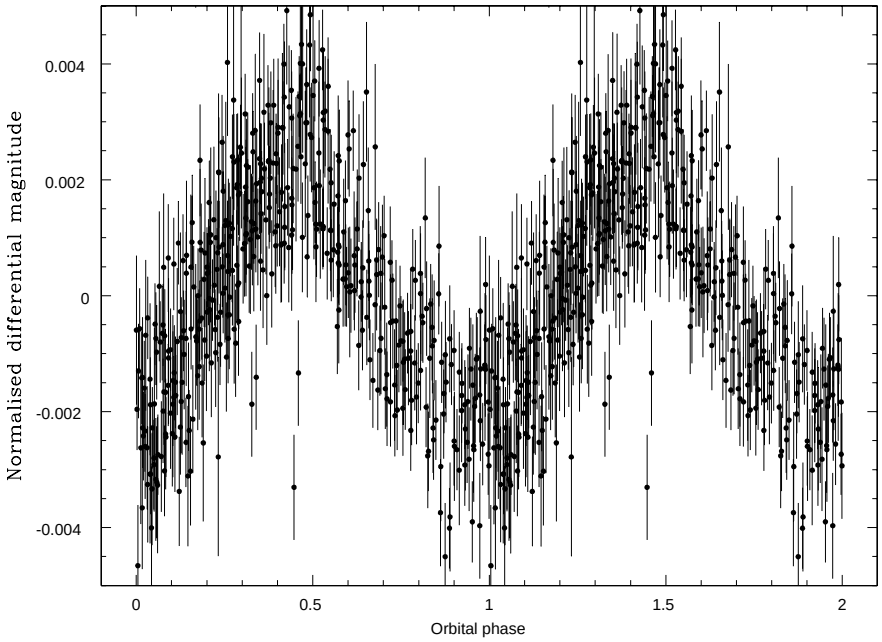

Figure 2.7: GD 356: Light curve folded on the best-fitting period of 12.4533 cycles/day = 0.08030 days

2.5 Discussion & Conclusions

2.5.1 WD 1953-011

The variation in the flux from WD 1953-011 could be explained if it were a binary system, with the secondary body emitting re-processed light visible for part of the orbital cycle. However, Maxted et al. (2000) found that the radial velocity was constant to within 2 km/s. Within this error, assuming the inclination is 90° and using an orbital period of 1.44 days, it is still possible to miss a companion body with mass < 0.009 $M_\odot$ ($\sim$10 M_J) orbiting at approximately 0.02 AU. However, such a body would only re-process $\sim 0.013\%$ of the light from the white dwarf, and hence could not produce the variability on the $\sim 2\%$ peak-to-peak level that we see. Decreasing the inclination increases the allowable mass of a companion, but also increases the orbital separation. For a secondary body to be massive enough to re-

process 1% of the light from the white dwarf, the orbital inclination would have to be less than 1°, by which point the difference in the visibility of the re-processed light at different phases would be negligible. This leads us to believe that the variability is somehow caused by the magnetic field of the MWD.

2.5.2 GD 356

The analysis of spectropolarimetric observations of GD 356 undertaken by Ferrario et al. (1997) led those authors to conclude that magnetic activity is confined to a limited, latitudinally extended spherical sector or strip which covers around 10% of the stellar surface. The presence of H_α and H_β in emission shows that a temperature inversion exists in this region, but since the gas is tenuous and optically thin it is energetically insignificant and unlikely to contribute to the continuum emission. By analogy with star- and sun-spots, where convective energy flow is suppressed by high magnetic fields (at $T_{\rm eff} \sim 7500$ K, GD 356 has a convective atmosphere, Bergeron et al. 2001), we expect regions of higher field such as this to be dark. We show that the near sinusoidal variability visible in our V-band light curve is consistent with this dark spot.

2.5.3 The cool spot variability models

We believe that the variations on both WD 1953-011 and GD 356 may be caused by star spots on the surface of the WDs, analogous to sun spots. Star spots are regions where magnetic fields are concentrated. The strong field beneath the surface suppresses the normal convective upflow of hot material from the interior, cutting off the energy supply to the region above. This causes a spot of lower temperature, and therefore lower luminosity, to be formed. As the MWD rotates, the visibility

of this cooler spot will vary, causing a periodic variation in the flux from the star. At temperatures of only $\sim$7900 K and $\sim$7500 K for WD 1953-011 and GD 356 respectively, both are well below the limit required for a convective atmosphere (12 – 14000 K, Bergeron et al. 1995), and therefore may be capable of forming star spots.

The visibility of the spot will depend upon the angle between the spin axis and our line of sight. Consider a small spot at latitude β on the white dwarf. The variation in the light curve will mainly depend upon the varying projected area of the spot as the white dwarf rotates (we ignore limb darkening as a second order effect).

Defining phase $\phi = 0$ as the point at which spot is closest to us, then the cosine of the angle between the normal to the surface of the white dwarf at the location of the spot and our line of sight (α) is given by

$$\cos\alpha = \cos\beta \sin i \cos\phi + \cos i \sin\beta,$$

where i is the inclination of the spin axis to our line of sight. The projected area factor, $\cos\alpha$, therefore varies sinusoidally with the phase ϕ. This will be true so long as $\cos\alpha > 0$ for all ϕ (if $\cos\alpha < 0$ then the spot is not visible, so the light curve will be flat).

Therefore, for a sinusoidally varying light curve, we require that $\beta > i$. If seen at large i then the spot must be near the pole, but if i is small, then the spot could be almost anywhere on the visible hemisphere - the only condition is that $\beta > i$.

The amplitude of the light curve depends upon the size of the spot and how dark it is, and it would be easy to fit the light curves of both WD 1953-011 and GD 356 for a variety of spot sizes. Since a spot of finite size is simply the result of integrating many infinitesimal spots, large spots can also lead to sinusoidal variations as long

as every part of them satisfies the $\beta > i$ constraint. This is consistent with both the model for WD 1953-011 proposed by Maxted et al. (2000), who suggested that the magnetic spot may cover $\sim 10\%$ of the surface of the WD, and the estimate by Ferrario et al. (1997), who suggested a similar spot size on GD 356. Limb-darkening of the form $I \propto 1 - \epsilon + \epsilon \cos\alpha$ will introduce a first harmonic from the $\epsilon \cos\alpha$ factor. This will be negligible as long as

$$\frac{1}{2}\epsilon \cos\beta \sin i \ll 1 - \epsilon,$$

where ϵ is the linear limb-darkening coefficient. Taking $\epsilon \approx 0.6$, we require $\cos\beta \sin i \ll 1.3$. This can be satisfied along with $\beta > i$ by many values of spin axis inclination and spot latitude, e.g. $i = 30$, $\beta = 70$ gives $\cos\beta \sin i = 0.17$. In this case, a large spot would help suppress the harmonic term relative to the fundamental. Thus a spot on the surface provides a natural explanation for the sinusoidal flux variation that we see.

For GD 356, the region is presumably the source of the Zeeman-split emission lines of H_α and H_β seen in optical spectra, as proposed previously by Ferrario et al. (1997). Although those authors (and Gnedin et al. 2001) did not report variability of the emission lines, either in velocity or flux, in the light of the discovery of broad-band photometric variability a detection of modulation of the emission lines themselves may provide clues as to their origin. However, this photometric modulation is so small that, even if it is stronger in the Zeeman components than the photometry, it may be difficult to detect. We note that while we have concentrated on the dark-spot model as the source of the photometric variability, we are unable to rule out a grey-spot model, or a non-uniform temperature distribution across the surface of the white dwarf, unrelated to the chromospheric spot.

2.5.4 Alternative theories

The sinusoidal variations observed in the light curves of both WD 1953-011 and GD 356 are consistent with the rotational modulation of a dark spot covering $\sim 10\%$ of the stellar surface. This spot is either observed near the rotational equator from a position near the rotational pole, or close to the rotational pole from high inclination. There have, however, been a number of alternative explanations for the variability in the two systems, which we discuss below.

2.5.4.1 WD 1953-011

It was suggested by our anonymous referee for Brinkworth et al. (2005) that the photometric variations observed in WD 1953-011 may be caused instead by the presence of circumstellar matter caught in the magnetic field of the white dwarf, as observed in some helium-rich Bp stars (e.g. Groote & Hunger 1982). We believe that this is highly unlikely due to the absence of emission lines in the spectra of the star taken by Maxted et al. (2000), and the absence of a formation mechanism for these clouds. Three possible origins are suggested in Groote & Hunger (1982): that the clouds are left over matter from the formation of the white dwarf; that they are formed through accreted matter; or that they are formed from mass lost by the white dwarf. The first scenario is unlikely as any matter left over from the formation of the white dwarf should have been driven off by radiation pressure while the white dwarf was still very hot. Similarly, the second mechanism should produce emission lines in the magnetic white dwarf spectrum that are not seen in the observed spectra. Finally, the low temperature and low magnetic field strength of WD 1953-011 make it doubtful that the stellar wind would be strong enough to drive mass loss from the white dwarf, or that the ejected mass would be trapped by the field lines. We therefore find it improbable that the variations seen in WD 1953-011 are caused by anything

other than a feature on the surface of the star itself.

2.5.4.2 GD 356

We have deliberately not attempted here to give a physical explanation for the origin of the Zeeman-split emission lines that make GD 356 unique even among the rare magnetic white dwarfs. Chromospheric activity (and an associated X-ray bright corona) is an obvious explanation, but no evidence for such a phenomenon has ever been detected from a magnetic white dwarf (e.g. Arnaud et al. 1992; Cavallo et al. 1993). From *ROSAT* observations, Musielak et al. (1995) give the upper limit on the X-ray luminosity of GD 356 at a few $\times 10^{26}\,\mathrm{erg\,s^{-1}}$, the same order of magnitude as the luminosity of the solar corona. The only white dwarf that might have a corona detected at X-ray wavelengths, KPD 0005+5106, has an implied luminosity five orders of magnitude higher (Fleming et al. 1993). The evidence for a very localised emission region led Ferrario et al. (1997) to also argue against the chromospheric activity / hot corona interpretation.

Alternatively, GD 356 might be accreting either from a nearby companion or via Bondi-Hoyle accretion from an interstellar medium. However, near-infrared photometry presented by Ferrario et al. (1997) rules out the presence of all but very low mass non-stellar companions, and the lack of detectable X-ray emission by Musielak et al. (1995) renders the accretion scenario unsatisfactory at present.

We note that new, more sensitive X-ray observations of GD 356 have recently been scheduled with the *Chandra* observatory. The detection of hard X-ray emission, and possibly X-ray variability on the same timescale as the optical oscillations reported here would give credibility to the chromospheric activity and/or accretion models.

Chapter 3

Magnetic white dwarf survey

Following our discovery of photometric variability in the cool, low-field, isolated magnetic white dwarfs, WD 1953-011 and GD 356, we decided to carry out a similar survey of all of the isolated magnetic white dwarfs in Wickramasinghe & Ferrario (2000). Before this survey, almost two-thirds of all magnetic white dwarfs had never been observed for photometric, polarimetric or spectroscopic variability, and the longest confirmed period for any magnetic white dwarf was for our target, WD 1953-011, at 1.44 days. Assuming that variability in isolated white dwarfs is due to their spin period, the survey was intended to tackle a range of issues: firstly, is there any correlation between spin period and other key parameters, such as magnetic field strength, age, temperature and mass? Secondly, is the period distribution of magnetic white dwarfs really bimodal, with one group rotating extremely slowly (>100 years) and another rotating very quickly, or is this a selection effect, with short-period variability favourably detected within week-long observing runs and long-period variability detected between individual observing campaigns? Finally, can we verify our star-spot theory by searching for variability in other low-field white dwarfs with temperatures below the critical temperature for a convective atmosphere

of $\sim$12 – 14000 K?

We were awarded 3 weeks of JKT time in August 2002, February 2003 and May 2003 to conduct our survey of the targets visible from the Northern hemisphere. We have also just been awarded further time on the robotic Liverpool Telescope, spread over the next 4 semesters to search for longer-term variability in our sample. This will be the first attempt to search for periods on timescales of months. Here we present the preliminary results of our initial survey.

3.1 Observations

In total, over the 3 weeks of JKT time, we observed 40 targets from the list of isolated magnetic white dwarfs contained in Wickramasinghe & Ferrario (2000). Of those targets, we were able to observe 14 over more than one week to search for variability over timescales of weeks – months. All of the sources were observed using the Harris V filter and the SITe1 CCD chip (2088 $\times$ 2120 pixels, readout noise = 6 e, gain = 1.9 e/ADU, pixel size = 15μm, image scale = 0.33"/pix). Once the field of view was set up for the targets, the chip was windowed for subsequent observations in order to reduce the readout time during the August and May runs. This was not possible during the February 2003 run due to reduction software problems at the time. Exposure times varied between 30 s and 200 s, depending on the magnitude of the target and the observing conditions. A full list of observations can be found in Table 3.1.

3.2 Data Reduction

All of the data were reduced immediately at the telescope to allow us to adapt our observing plan to the results. Initially we observed all of the targets on as many time baselines as possible, ensuring that we spent 2 hours on each target to check for short-term variability, then re-visiting them on as many nights as possible during the week. By reducing the data at the telescope we were able to adapt our strategy to ensure that a source varying on short periods could be observed again over a couple of hours. This also meant that we were not wasting time observing long-period sources on short timescales.

The data were re-reduced more carefully on our return. All of the data were reduced in the same way using T. R. Marsh's ULTRACAM pipeline software. Bias frames for each night were combined to create a master bias, which was then subtracted from all other frames. Sky flats were then checked, and any with counts of less than 10000 or greater than 35000 were discarded. The remaining flats were combined to create a master flat for each night that was normalised and divided from the target frames. There were no sky flats for the 22nd, 25th or 26th of February so the target frames from those nights were flat-fielded using combined dome flats.

Differential photometry was performed on the targets with respect to at least 2 bright comparison stars in the field. We used variable apertures (allowing the apertures to vary with the fitted FWHM of the source) with normal extraction (as opposed to Tim Naylor's optimal weighted extraction) and clipped mean sky estimation. Once we had checked the comparison stars for variability, we then added the non-variable ones together to create one bright comparison, which we divided into the target to give the differential photometry. Results were output in differential flux and all times were converted to heliocentric Julian date.

Table 3.1: List of observations of the 40 isolated magnetic white dwarfs from Wickramasinghe & Ferrario (2000). Observations are listed by target, in order of RA.

Target	Alt. name	Dates	Exp (s)	N	Conditions(seeing)
G217-037	WD0009+501	04/08/02	90-120	35	Clear (0.8" – 1.3")
		05/08/02	60	40	Clear (0.7" – 1.5")
		06/08/02	30-50	88	Clear, dusty ($\sim$ 0.7")
		07/08/02	60	35	Clear (0.8" – 1.2")
G158-45	WD0011-134	02/08/02	60	5	Clear ($\sim$1")
		03/08/02	60	40	Clear (0.7" – 1")
		04/08/02	120	10	Clear (0.8" – 1.3")
		05/08/02	120	8	Clear (0.7" – 1.5")
		06/08/02	120	13	Clear, dusty ($\sim$0.7")
		07/08/02	60-200	15	Clear (0.8" – 1.2")
HE0107-0158	n/a	02/08/02	60	40	Clear ($\sim$1")
		04/08/02	120	10	Clear (0.8" – 1.3")
		06/08/02	40-50	10	Clear, dusty ($\sim$0.7")
PG0136+251	WD0136+251	04/08/02	90-120	10	Clear (0.8" – 1.3")
		06/08/02	45	10	Clear, dusty ($\sim$0.7")
		07/08/02	120	5	Clear (0.8" – 1.2")
KPD0253	WD0253+508	24/02/03	120	15	Poor seeing
LHS 5064	WD0257+080	20/02/03	120	5	Clear (1.8")
		21/02/03	120	5	Clear (1.4" – 2")
		22/02/03	120	10	Clear (1")
		24/02/03	120	5	Poor seeing
		26/02/03	120	8	Clear ($\sim$2")

Table 3.1 cont.

Target	Alt. name	Dates	Exp (s)	N	Conditions (seeing)
G 99-37	WD0548-001	20/02/03	60	5	Clear (∼1.8")
		21/02/03	60	5	Clear (1.4" – 2")
		22/02/03	30-60	10	Clear (1")
		26/02/03	60	3	Clear (∼2")
G 99-47	WD0553+053	20/02/03	40	35	Clear (∼1.8")
		21/02/03	60	5	Clear (1.4" – 2")
		22/02/03	30-60	25	Clear (1")
		26/02/03	60	3	Clear (∼2")
GD 77	WD0637+477	20/02/03	60	5	Clear (∼1.8")
		21/02/03	100	20	Clear (1.4" – 2")
		22/02/03	60	10	Clear (1")
		24/02/03	60	5	Poor seeing
		25/02/03	60	5	Good (1" – 1.2")
G 234-4	WD0728+642	21/02/03	120	5	Clear (1.4" – 2")
		22/02/03	120	10	Clear (1")
		26/02/03	120	3	Clear (∼2")
G 111-49	WD0756+437	21/02/03	120	5	Clear (1.4" – 2")
		22/02/03	120	10	Clear (1")
		24/02/03	120	10	Poor seeing
		25/02/03	120	48	Good (1" – 1.2")
		26/02/03	120	27	Clear (∼2")
GD 90	WD0816+376	21/02/03	120	5	Clear (1.4" – 2")
		22/02/03	120	10	Clear (1")
		26/02/03	120	3	Clear (∼2")
LB 8827	PG0850+192	21/02/03	120	5	Clear (1.4" – 2")

Table 3.1 cont.

Target	Alt. name	Dates	Exp (s)	N	Conditions (seeing)
		22/02/03	90	10	Clear, cirrus later (1")
		24/02/03	120	5	Poor seeing
		25/02/03	80-120	10	Good (1" – 1.2")
G 195-19	WD0912+536	21/02/03	40	5	Clear (1.4" – 2")
		22/02/03	60	10	Clear (1")
		24/02/03	90	5	Poor seeing
		25/02/03	60-75	10	Good (1" – 1.2")
		26/02/03	75	3	Clear (∼2")
		25/05/03	60	5	Clear (∼1.5")
		26/05/03	60	5	Good (<1")
		27/05/03	30	5	Clear (∼1")
		28/05/03	60	5	Dusty (1.1" – 1.5")
		29/05/03	60	5	Clear (∼1")
		30/05/03	60	5	Photometric (∼1")
		31/05/03	60-120	10	Cirrus (1.1")
LB 11146	WD0945+245	21/02/03	80	5	Clear (1.4" – 2")
		24/02/03	120	5	Poor seeing
		25/02/03	120	8	Good (1" – 1.2")
PG 1015+015	WD1015+014	21/02/03	180	26	Clear (1.4" – 2")
GD 116	WD1017+367	21/02/03	120	5	Clear (1.4" – 2")
		25/02/03	60	8	Good (1" – 1.2")
LHS 2273	WD1026+117	26/05/03	300	5	Good (<1")
		27/05/03	300	5	Clear (∼1")
		28/05/03	300	20	Dusty (1.1" – 1.5")
		31/05/03	300	5	Clear (1.1")

Table 3.1 cont.

Target	Alt. name	Dates	Exp (s)	N	Conditions (seeing)
PG 1031+234	WD1031+234	22/02/03	90-120	25	Clear, cirrus later (1" – 2")
HE 1045-0908	WD1045-091	25/02/03	120	29	Good (1" – 1.2")
		26/02/03	120	18	Clear (∼2")
LBQS 1136-0132	WD1136-015	21/02/03	180	5	Clear (1.4" – 2")
HE 1211-1707	n/a	26/02/03	120	21	Clear (∼2")
		30/05/03	300	22	Photometric (∼1")
PG 1220+234	WD1220+234	21/02/03	60	5	Clear (1.4" – 2")
		22/02/03	30	10	Cirrus (∼1" – 2")
		26/02/03	60	3	Clear (∼2")
G 256-7	WD1309+853	25/05/03	300	5	Clear (∼1.5")
		26/05/03	180-300	10	Good (<1")
		29/05/03	180	17	Clear (∼1")
		31/05/03	180	5	Clear (1.1")
SBSS 1349+545	WD1349+545	26/05/03	300	5	Good (<1")
		27/05/03	300	10	Clear (∼1")
		28/05/03	300	20	Dusty (1.1" – 1.5")
		29/05/03	300	11	Clear (∼1")
		31/05/03	300	5	Clear (1.1")
LP 907-037	WD1350-090	25/05/03	120	5	Clear (∼1.5")
		26/05/03	90-100	10	Good (<1")
		31/05/03	90	15	Clear (1.1")
EUVE J1439+75.0	n/a	02/08/02	60	5	Clear (∼1")
		03/08/02	60	10	Clear (0.7" – 1")
		07/08/02	45	5	Clear (0.8" – 1.2")
		21/02/03	120	5	Clear (1.4" – 2")

Table 3.1 cont.

Target	Alt. name	Dates	Exp (s)	N	Conditions (seeing)
		22/02/03	120	5	Some cirrus (2" – 3")
		26/02/03	120	3	Clear (∼2")
		31/05/03	120	5	Clear (<1")
PG 1533-057	WD1533-057	03/08/02	60	5	Clear (0.7" – 1")
		04/08/02	60	10	Clear (0.8" – 1.3")
		05/08/02	60	43	Clear (0.7" – 1.5")
		07/08/02	60	10	Clear (0.8" – 1.2")
		21/02/03	120	5	Clear (1.4" – 2")
		22/02/03	120	10	Cirrus, near moon (∼2")
		25/02/03	120	3	Good (1" – 1.2")
		26/02/03	120	3	Clear (∼2")
		25/05/03	180	20	Clear (∼1.5")
		26/05/03	90-120	92	Good (<1")
		27/05/03	90	90	Clear (∼1")
		29/05/03	180	44	Clear (∼1")
		30/05/03	180	45	Photometric (∼1")
		31/05/03	180	35	Clear (<1")
GD 356	WD1639+537	03/08/02	60	10	Clear (0.7" – 1")
		04/08/02	60	10	Clear (0.8" – 1.3")
		05/08/02	60-90	13	Clear (0.7" – 1.5")
		06/08/02	60	55	Clear, dusty (∼0.7")
		07/08/02	60	31	Clear (0.8" – 1.2")
		21/02/03	120	34	Clear (1.4" – 2")
		22/02/03	90	20	Some cirrus (∼2")
		25/02/03	60-90	27	Good (1" – 1.2")

Table 3.1 cont.

Target	Alt. name	Dates	Exp (s)	N	Conditions (seeing)
		26/02/03	90	28	Clear (∼2")
		25/05/03	85	66	Clear (∼1.5")
		27/05/03	120	50	Clear (∼1")
		30/05/03	120	40	Photometric (∼1")
		31/05/03	120	50	Clear (<1")
PG 1658+441	WD1658+441	02/08/02	60	40	Clear (∼1")
		04/08/02	60	10	Clear (0.8" – 1.3")
		07/08/02	60	5	Clear (0.8" – 1.2")
		28/05/03	120	10	Dusty (1.1" – 1.5")
G 240-72	WD1748+708	02/08/02	60	40	Clear (∼1")
		04/08/02	60	10	Clear (0.8" – 1.3")
		06/08/02	40	5	Clear, dusty (∼0.7")
		07/08/02	60	5	Clear (0.8" – 1.2")
		28/05/03	90	10	Dusty (1.1" – 1.5")
G 183-35	WD1814+248	03/08/02	60	10	Clear (0.7" – 1")
		04/08/02	60-90	10	Clear (0.8" – 1.3")
		05/08/02	120	5	Clear (0.7" – 1.5")
		06/08/02	45-50	15	Clear (∼0.7")
		07/08/02	60	48	Clear (0.8" – 1.2")
		25/05/03	95	10	Clear (∼1.5")
		26/05/03	50	5	Good (<1")
		28/05/03	180	5	Dusty (1.1" – 1.5")
		29/05/03	180	10	Clear (∼1")
		30/05/03	180	10	Photometric (∼1")
G 141-2	WD1818+126	02/08/02	60	5	Clear (∼1")

Table 3.1 cont.

Target	Alt. name	Dates	Exp (s)	N	Conditions (seeing)
		03/08/02	60	5	Clear (0.7" – 1")
		04/08/02	60-180	26	Clear (0.8" – 1.3")
		05/08/02	60	5	Clear (0.7" – 1.5")
		06/08/02	30-40	10	Clear, dusty (∼0.7")
		07/08/02	40	5	Clear (0.8" – 1.2")
		28/08/02	180	10	Dusty (1.1" – 1.5")
G 227-28	WD1820+609	03/08/02	60	10	Clear (0.7" – 1")
		05/08/02	60	10	Clear (0.7" – 1.5")
		06/08/02	30-40	15	Clear, dusty (∼0.7")
		07/08/02	30	5	Clear (0.8" – 1.2")
		28/05/03	180	10	Dusty (1.1" – 1.5")
G 227-35	WD1829+547	02/08/02	60	40	Clear (∼1")
		03/08/02	60	10	Clear (0.7" – 1")
		07/08/02	40	5	Clear (0.8" – 1.2")
		29/05/03	180	10	Clear (∼1")
Grw+70°8247	WD1900+705	03/08/02	30	60	Clear (0.7" – 1")
		05/08/02	20	50	Clear (0.7" – 1.5")
		06/08/02	10	5	Clear, dusty (∼0.7")
		07/08/02	30	5	Clear (0.8" – 1.2")
		27/05/02	60	5	Clear (∼1")
GD 229	WD2010+310	02/08/02	60	40	Clear (∼1")
		03/08/02	60	10	Clear (0.7" – 1")
		07/08/02	120	5	Clear (0.8" – 1.2")
		29/05/03	120	10	Clear (∼1")
PG 2329+267	WD2329+267	02/08/02	60	45	Clear (∼1")

Table 3.1 cont.

Target	Alt. name	Dates	Exp (s)	N	Conditions (seeing)
		03/08/02	60	10	Clear (0.7" – 1")
		06/08/02	60	60	Clear, dusty (∼0.7")
		07/08/02	60-120	38	Clear (0.8" – 1.2")
		25/05/03	200	5	Clear (∼1.5")

3.3 Detection of variability

As with WD 1953-011 and GD 356, we used a "floating mean" periodogram (e.g., Cumming et al. 1999; Morales-Rueda et al. 2003; see Chapter 2 for a discussion) to search for periodicity in each of the targets. The resultant periodogram is a χ^2 plot of the fit at each frequency. In order to establish that the periodicity was real, I carried out two other tests. Firstly I fit a constant to the data and compared the χ^2 of the fit to the minimum χ^2 in the periodogram, running an F-test to check whether the target was indeed variable. Unfortunately, I found that the F-test supported variability in all of my objects, even those for which I am virtually certain that none exists over the measured timescales. This is almost certainly due to underestimated errors in the data not covering the scatter. In order to compensate for this, I re-scaled the errors to give a reduced $\chi^2 = 1$ for the global minimum in the periodogram. I then re-compared the χ^2 values from the periodogram to the χ^2 of a constant fit, taking a change in χ^2 of 16 (equivalent to 4σ) as the minimum required for a period to be significantly better than a constant fit. A list of the χ^2 , reduced χ^2 and re-scaled χ^2 values for all of the targets can be found in Table 3.2 Having established that the

formal error bars failed to cover the scatter in the data, I then checked the level of variability in the comparison stars compared to that in the target. I calculated the RMS of the normalised target differential light curve and normalised light curves of the comparisons with respect to each other (see Table 3.2), although it should be noted that the measured RMS values are dependent on the magnitude of the stars. For those sources with a target RMS comparable to the comparison RMS, I ran a periodogram on the comparison stars to check for any periodicity in the variability. Those targets that display variability on the same level as the comparisons, with a similar significance in the periodogram compared to a constant fit, are listed as non-variable. A good example of this can be seen in G99-37 (Fig 3.33) which seemed to display significant variability, but which was shown to be due to low-amplitude variations in at least one of the comparison stars.

The final classification of variable or non-variable was made by using a combination of the above methods. The identification of the best-fitting period for the variable targets was made by examining the change in χ^2 between the global χ^2 minimum and the next-best frequency. Lines marking changes in χ^2 of 1, 4 and 9 (equivalent to 1σ, 2σ and 3σ errors, assuming only one fitted parameter) have been marked on each of the periodograms. The 2σ errors are quoted in the text, and a change in χ^2 of 9 between two minima was taken as a significantly better fit.

For some of the targets (e.g. LB8827) there were a number of local minima within the 3σ error. In these cases, I have also included a Lomb-Scargle periodogram of the data as an alternative test, plus the light curves folded on at least the best two periods from the two periodograms. The most likely periods for each of the targets are quoted in the text, along with their 2σ errors.

The results are split into 4 groups: targets displaying strong and clearly periodic variability; targets with strong variability, but undefined period; targets with

possible variability, but with more work or more data required to verify this, and finally, targets not seen to vary over the timescale of our observations. It should be stressed that the following results are somewhat preliminary, and therefore some targets may yet change groups as more rigorous checks are applied to the data and periodograms. Future work includes checking the outlying points for poor observing conditions or bad pixels near the target or comparisons, and applying Monte-Carlo and bootstrapping methods to the data to check the stability and significance of the minima in the periodograms.

3.3.1 Uncertainties in the period

For those targets with a derived period, I have included two plots of the periodogram: one showing the full range, and the other zoomed in on the best frequency. In the zoomed plot, I have plotted the boundaries of a change in χ^2 from the minimum of 1, 4 and 9 in magenta, green and red respectively. These correspond to the 1σ, 2σ and 3σ errors on the best-fit frequency, assuming that we have fit only one useful parameter - i.e. the period. I have over-plotted a line at our best frequency (i.e. at the global χ^2minimum) and a line at any previously reported frequency, taken from Wickramasinghe & Ferrario (2000), to check for consistency. Errors quoted in the text are the errors in the best-fitting frequency corresponding to a 2σ change in χ^2 from the local minimum, unless otherwise stated. Targets are split into the four groups previously outlined, but are listed alphabetically within each group.

Target	Target vs comparison RMS	Average comparison RMS	RMS_{targ} / RMS_{comp}	Constant χ^2	Sinusoid χ^2	N	Scaled constant χ^2	Scaled sinusoid χ^2	$\Delta\chi^2$
G111-49	0.0272	0.0053	5.11	2085	119	95	1592	91	1501
HE1211-1707	0.0142	0.0063	2.24	94	17	21	94	17	77
PG1015+015	0.0177	0.0048	3.66	288	32	26	198	22	176
PG1031+234	0.0473	0.0037	12.7	2401	29	24	1656	20	1636
PG1533-057	0.0060	0.0030	2.00	1050	644	326	532	322	210
G99-47	0.0091	0.0027	3.37	330	158	67	139	63	76
G195-19 (all)	0.0206	0.0052	3.94	4915	525	61	533	57	477
G195-19 (Aug)	0.0058	0.0021	2.72	174	26	27	154	23	121
G195-19 (May)	0.0100	0.0060	1.67	490	152	34	97	30	67
G217-037	0.0076	0.0054	1.40	1572	803	235	452	231	221
G227-28	0.0102	0.0062	1.64	449	79	81	438	77	361
G234-4	0.0077	0.0037	2.08	36	12	16	36	16	20
G240-72	0.0099	0.0055	1.80	1153	53	63	1441	59	1382
G240-72 (Aug)	0.0027	0.0031	0.87	51	36	51	67	47	20
LB8827	0.0163	0.0050	3.29	426	22	30	503	26	477
LHS2273	0.0085	0.0028	3.03	136	85	35	50	31	19
LHS5064	0.0179	0.0062	2.87	376	32	33	340	29	312
LP907-037	0.0068	0.0044	1.56	190	40	30	124	26	98
PG1658+441	0.0075	0.0052	1.44	363	77	64	283	60	223
PG2329+267	0.0083	0.0047	1.77	500	318	150	217	149	68
EUVE J1439+75.0	0.010	n/a	n/a	109	53	37	68	34	34
G99-37	0.0046	0.0042	1.10	39	11	21	60	17	43
G141-2	0.0090	0.0085	1.05	212	54	55	196	50	146
G158-45	0.0059	0.0043	1.38	163	118	89	119	86	33
G227-35	0.0059	0.0092	0.64	87	45	64	116	60	56
G256-7	0.0043	0.0069	0.62	39	21	35	58	31	27
GD90	0.0048	0.0035	1.37	23	8	16	35	12	23
GD229	0.0054	0.0051	1.05	218	94	65	141	61	80
Grw+70°8247	0.0058	0.0087	0.67	500	320	148	226	144	82
HE0107-0158	0.0096	0.0028	3.48	46	34	54	68	50	18
HE1045-0908	0.0059	0.0037	1.61	42	29	41	54	37	17
LB11146	0.0037	0.0043	0.86	12	3.5	12	27	8	19
PG0136+251	0.0116	0.0043	2.70	52	40	60	73	56	17
PG1220+234	0.0086	0.0060	1.43	16	7	17	32	13	19
SBSS1349+545	0.0046	0.0043	1.07	360	265	51	64	47	17
G183-35	0.0148	0.0086	1.72	245	211	154	154	114	40
GD77	0.0015	0.0013	1.18	72	54	45	55	41	14

Table 3.2: Table of parameters used to determine variability in our targets - see text for explanation. Targets are sorted by group: Targets displaying strong and clearly periodic variability; targets with strong variability but undefined period; targets with possible varibility; targets not seen to vary. Targets are listed in alphabetical order within those groups.

3.4 Results

3.4.1 Targets displaying strong and clearly periodic variability

3.4.1.1 G111-49

The magnetic nature of G111-49 was discovered by Putney (1995), who re-classified its type as DAP and reported strong circular polarisation (V_{max} = 9%)and a field strength of $\sim$ 220 MG. The author notes that G111-49 has been classified as a variety of different types since its first classification by Greenstein et al. (1977) and suggests that this could be indicative of rotation. We have discovered variability in G111-49 at a peak-to-peak level of $\sim$ 9% and a period of $6.68\,^{+0.02}_{-0.03}$ hours. The χ^2 of this fit is 117 over 91 degrees of freedom (dof), compared to the χ^2 of a constant fit of 2085 over 94 dof. The folded light curve and periodogram can be seen in Figs 3.1 & 3.2.

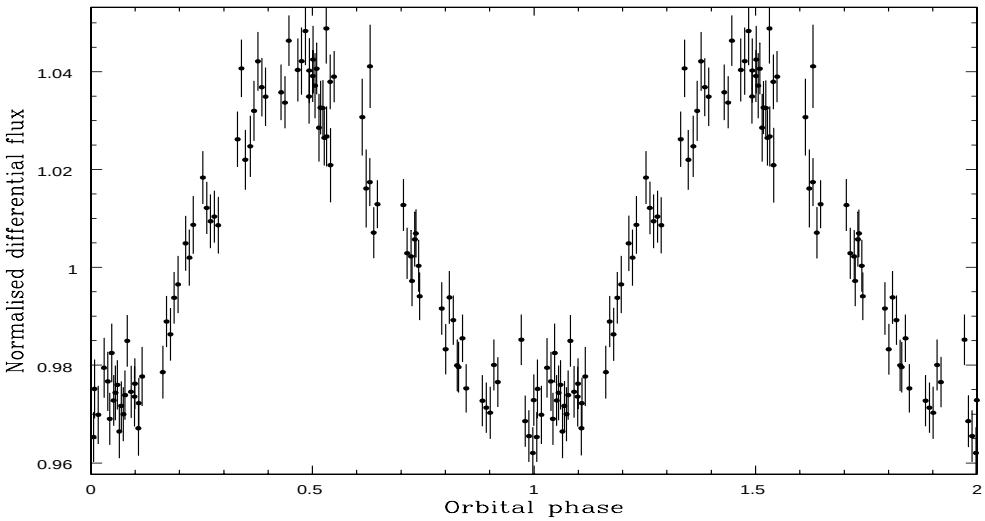

Figure 3.1: Phase-folded light curve for G111-49, with period = 6.68 hours.

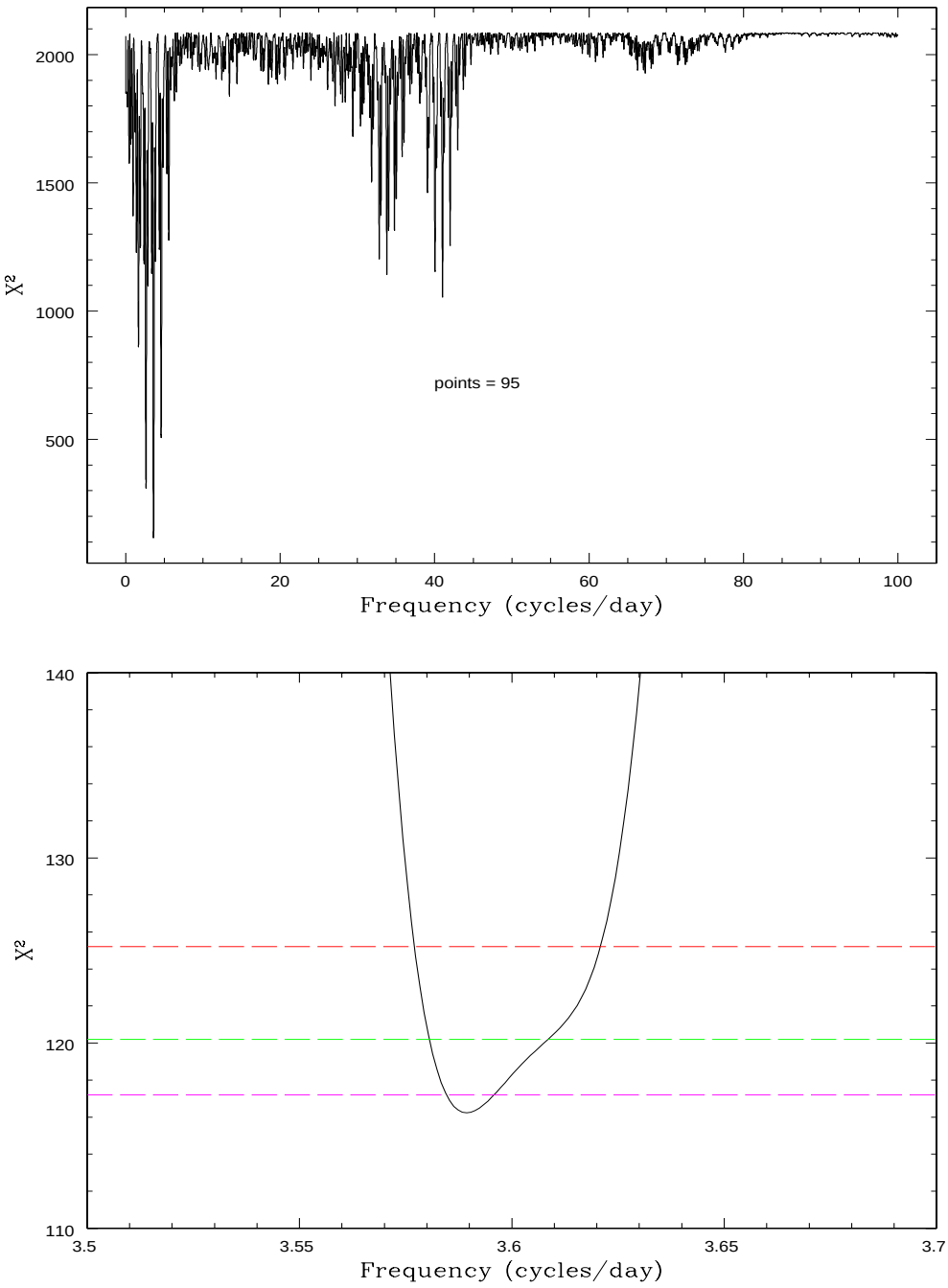

Figure 3.2: Top - periodogram for G111-49. Bottom - periodogram zoomed in on the best frequency of 3.59 cyc/day. Magenta, green and red dashed lines show the 1, 2 and 3σ errors.

3.4.1.2 HE1211-1707

Reimers et al. (1996) reported time-variable absorption features in the spectrum of HE1211-1707, and Schmidt et al. (2001) found the rotation period to be ∼2 hours. We were therefore surprised when our data from Feb 2003 failed to show any indication of periodic variability. We suspected that our exposure times were significantly too short (HE1211-1707 is one of the faintest targets in our sample, at V = 16.8 mag), so more than doubled them for the May 2003 run, when we also had better observing conditions. We therefore discarded the Feb 2003 data and concentrated on the second set. Using these data, we have confirmed variability in this target on a level of ∼ 2% with a period of $1.77\,^{+0.43}_{-0.23}$ hours (Fig. 3.3). The fit has $\chi^2 = 16.6$ over 17 dof compared to a constant fit of 94 over 20 dof.

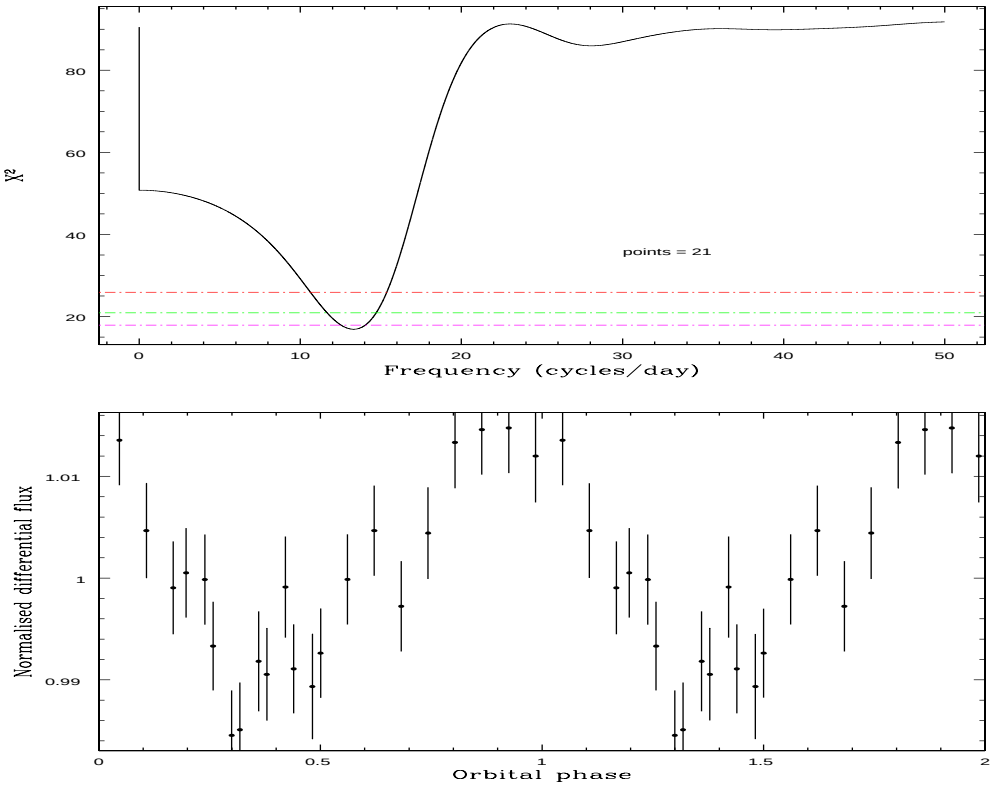

Figure 3.3: Top - periodogram for HE1211-1707. Bottom - phase-folded light curve for HE1211-1707, with period = 1.77 hours. (Frequency = 13.55 cyc/day)

3.4.1.3 PG1015+015

Wickramasinghe & Cropper (1988) reported a rotation period of 98.7 minutes for this object, based on variations in circular polarisation. We find that PG1015+015 is also photometrically variable at a level of $\sim 4.5\%$, with a period of $105\,^{+13}_{-7}$ mins (Figs 3.4 & 3.5). This is consistent with the previous value to within 2σ. Light curves folded on both 98.7 and 105 minutes look virtually identical and clearly show the variability in the star. The fit has a χ^2 of 32 over 22 dof, compared to a constant fit with $\chi^2 = 288$ over 25 dof.

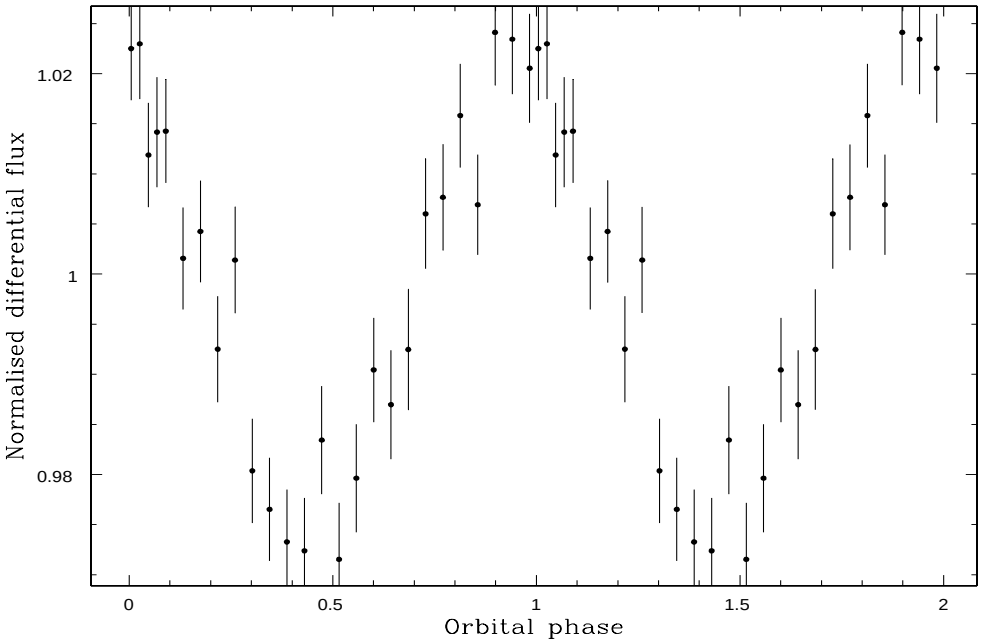

Figure 3.4: Light curve for PG1015+015 folded on the best period of 105 mins

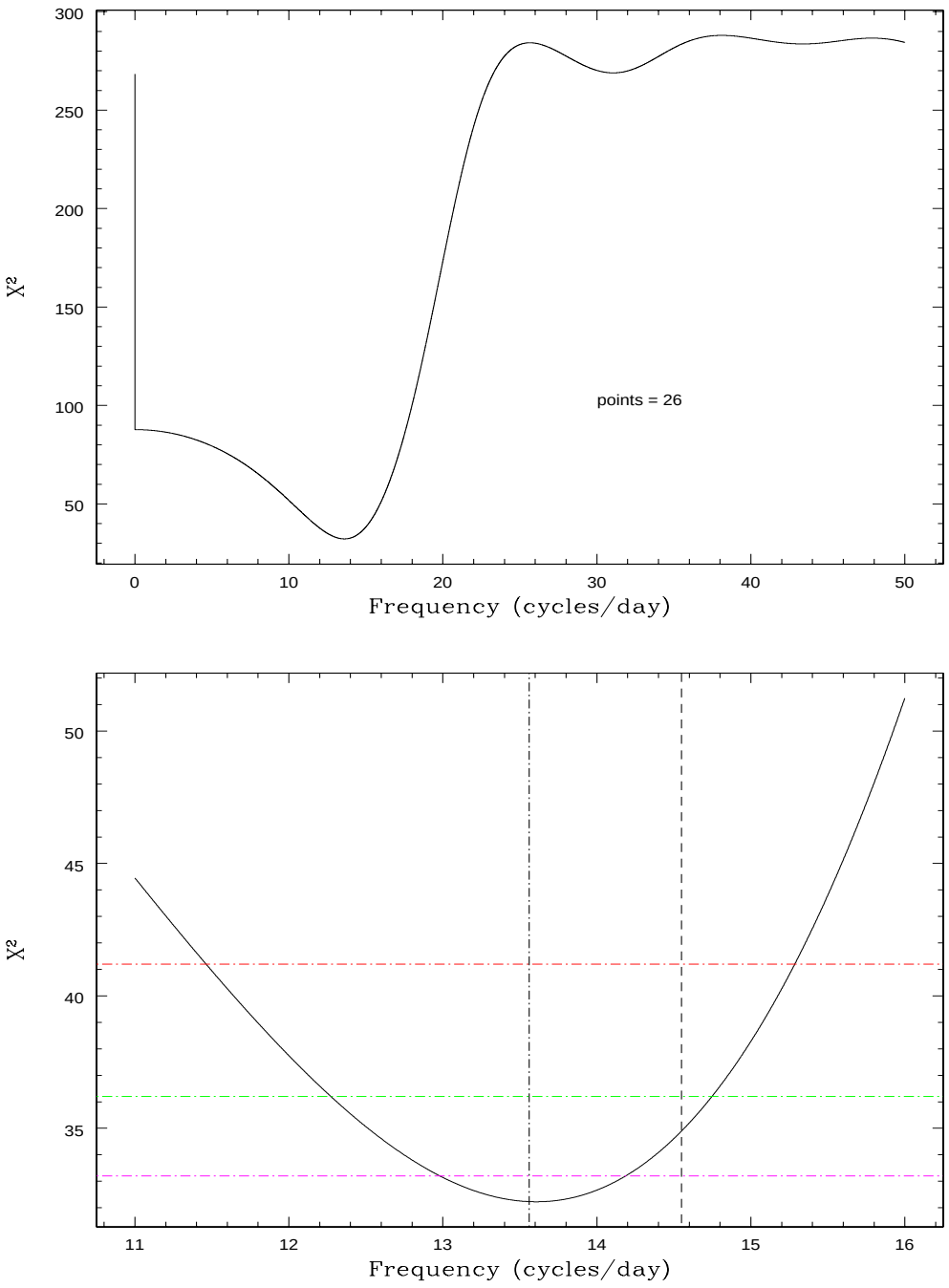

Figure 3.5: Top - periodogram for PG1015+015. Bottom - periodogram zoomed in on the best-fitting frequency of 13.7 cyc/day (P = 105 mins). The vertical lines show our best frequency and the previous frequency taken from the literature. Our period is consistent with the period from Wickramasinghe & Cropper (1988) to within 2σ error.

3.4.1.4 PG1031+234

Schmidt et al. (1986) reported that the optical light shows a high degree of polarisation ($P_{max} \simeq 6\%$, $V_{max} \simeq -12\%$) and a strong modulation with period 3.4 h, which they interpret as the rotation period. Our results indicate that PG1031+234 is indeed highly variable, with a full-amplitude of $\sim 15\%$, but that the period is 3.53 ± 0.05 h (Figs 3.7 & 3.6) and is inconsistent with the previously measured value. The best fit has $\chi^2 = 29$ over 20 dof, while a constant fit has $\chi^2 = 2401$ over 23 dof.

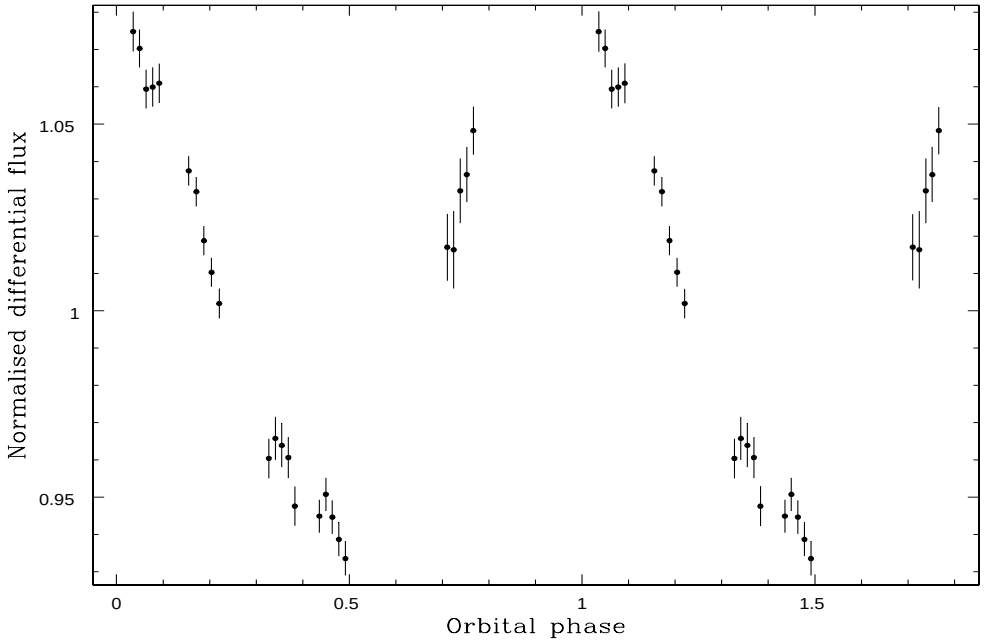

Figure 3.6: Light curve for PG1031+234, phase-folded on the best-fitting period of 3.53 hours.

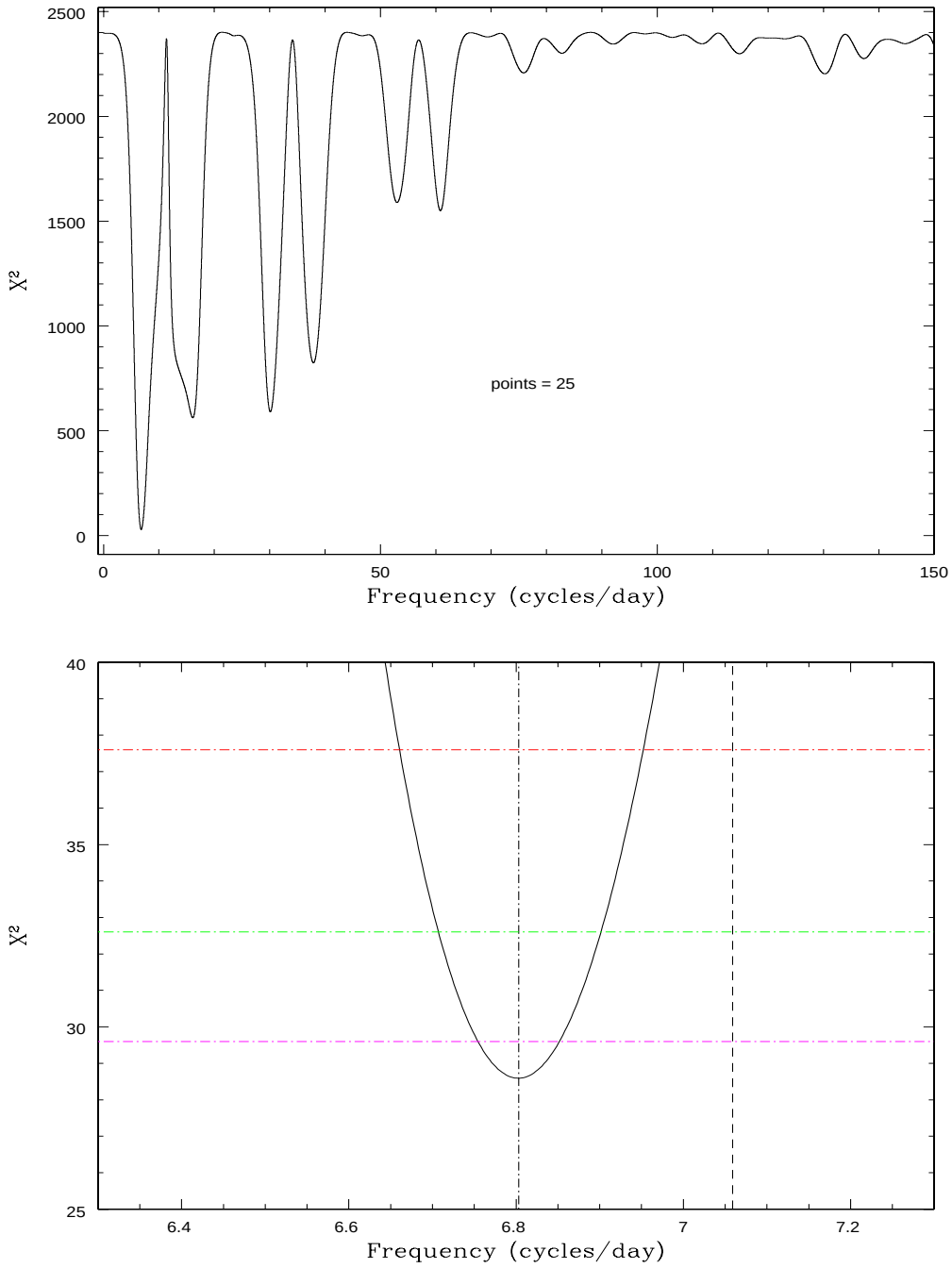

Figure 3.7: Top - periodogram for PG1031+234. Bottom - periodogram zoomed in on the best-fitting frequency of 6.803 cyc/day (P = 3.53 h). It can be seen that our rotational period is not consistent with the previously derived value.

3.4.1.5 PG1533-057

PG1533-057 was observed at all 3 epochs during our survey, but most of the data (326 points out of 413) were taken during May 2003. The periodograms for May 2003 and for all of the data both show a significant minimum at a frequency of $\sim$12.7 cyc/day, but the latter shows some aliasing structure. We believe that this is almost certainly due to low-level variability in the comparison stars over the year, and for the derivation of the rotational period, and when plotting the folded light curve, we use the data from May 2003 alone. We find that PG1533-057 is variable, with P = 1.890 ± 0.001 hours, and a full-amplitude of 1.4%. The χ^2 of this fit is 644 over 322 dof compared to a constant fit with 1050 over 325 dof.

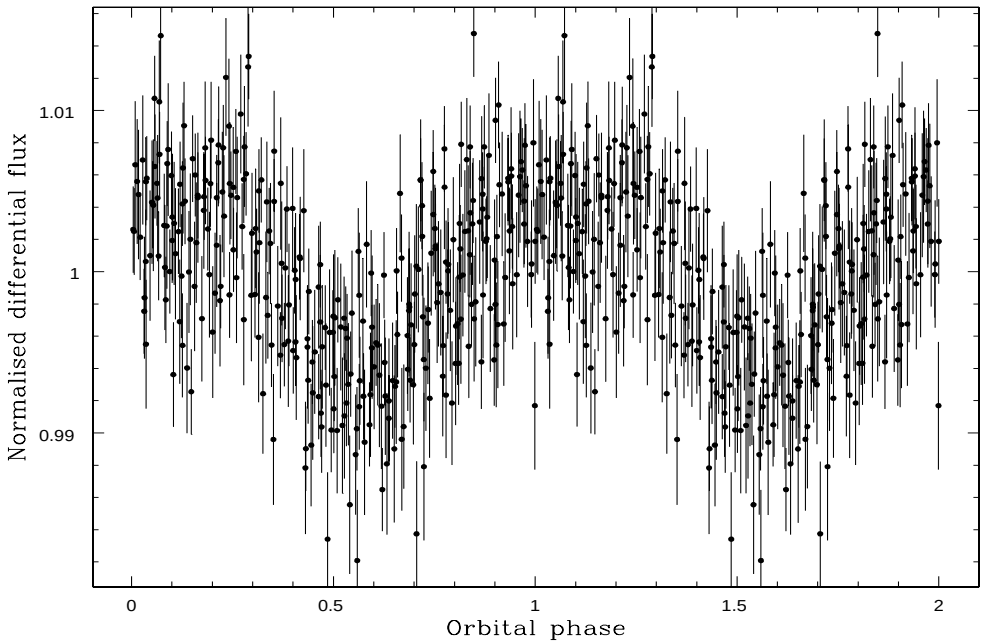

Figure 3.8: Light curve for PG1533-057 folded on the best period of 1.89 hours

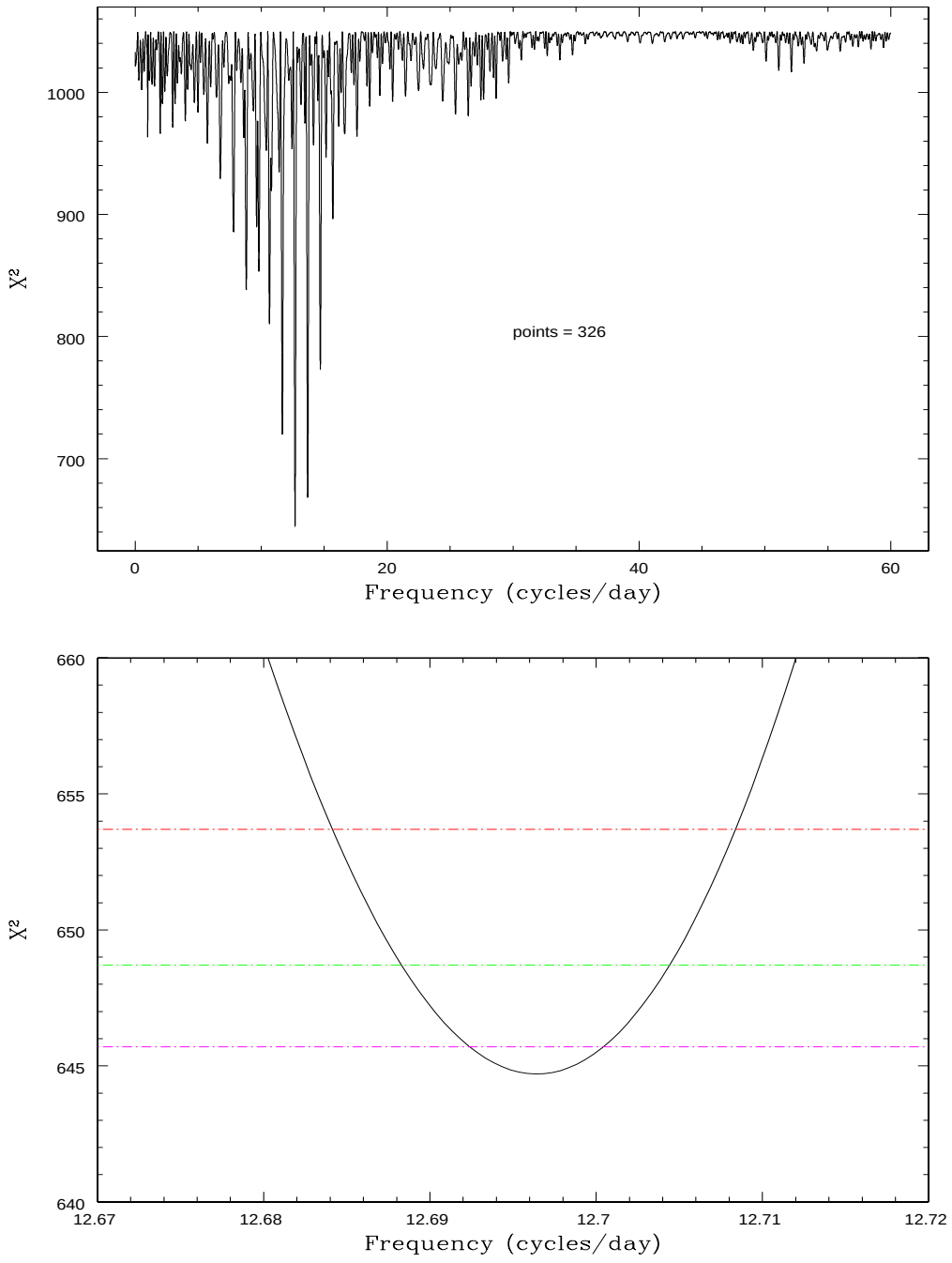

Figure 3.9: Top - periodogram for PG1533-057. Bottom - periodogram zoomed in on the best-fitting frequency of 12.7 cyc/day (P = 1.89 hours).

3.4.2 Targets displaying strong variability but undefined period

3.4.2.1 G99-47

We observed G99-47 during Feb 2003. Wickramasinghe & Ferrario (2000) reported a possible rotational period of $\sim$1h, although we have been unable to find further reference to this in the literature. Our first night of data on this object was affected by strong differential extinction, so we have therefore discarded this and concentrated on the other three nights. A constant fit to the data gives a χ^2 of 63 over 31 dof, in comparison to the global minimum of the periodogram at 53.65 cyc/day, with a χ^2 of 29 over 28 dof. The folded light curve is shown in Fig. 3.11 and can be seen to be very low-amplitude. There are a number of minima within the 2σ errors on the best frequency, so we find the period is between 26 and 27.5 mins, with a most likely period of 26.8 mins.

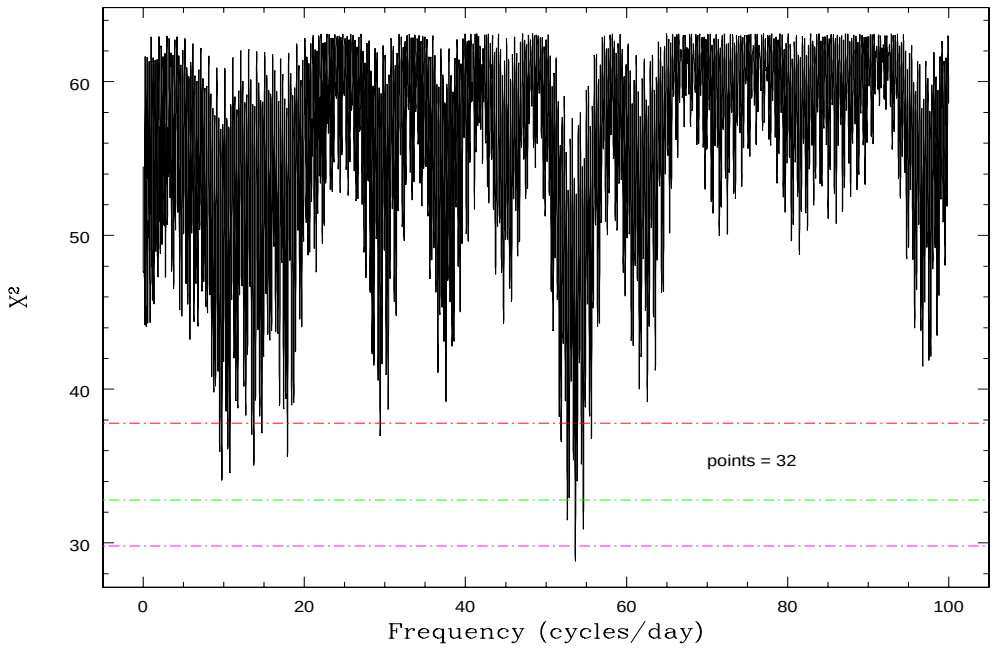

Figure 3.10: Periodogram for G99-47 with a best frequency of 53.65 cyc/day.

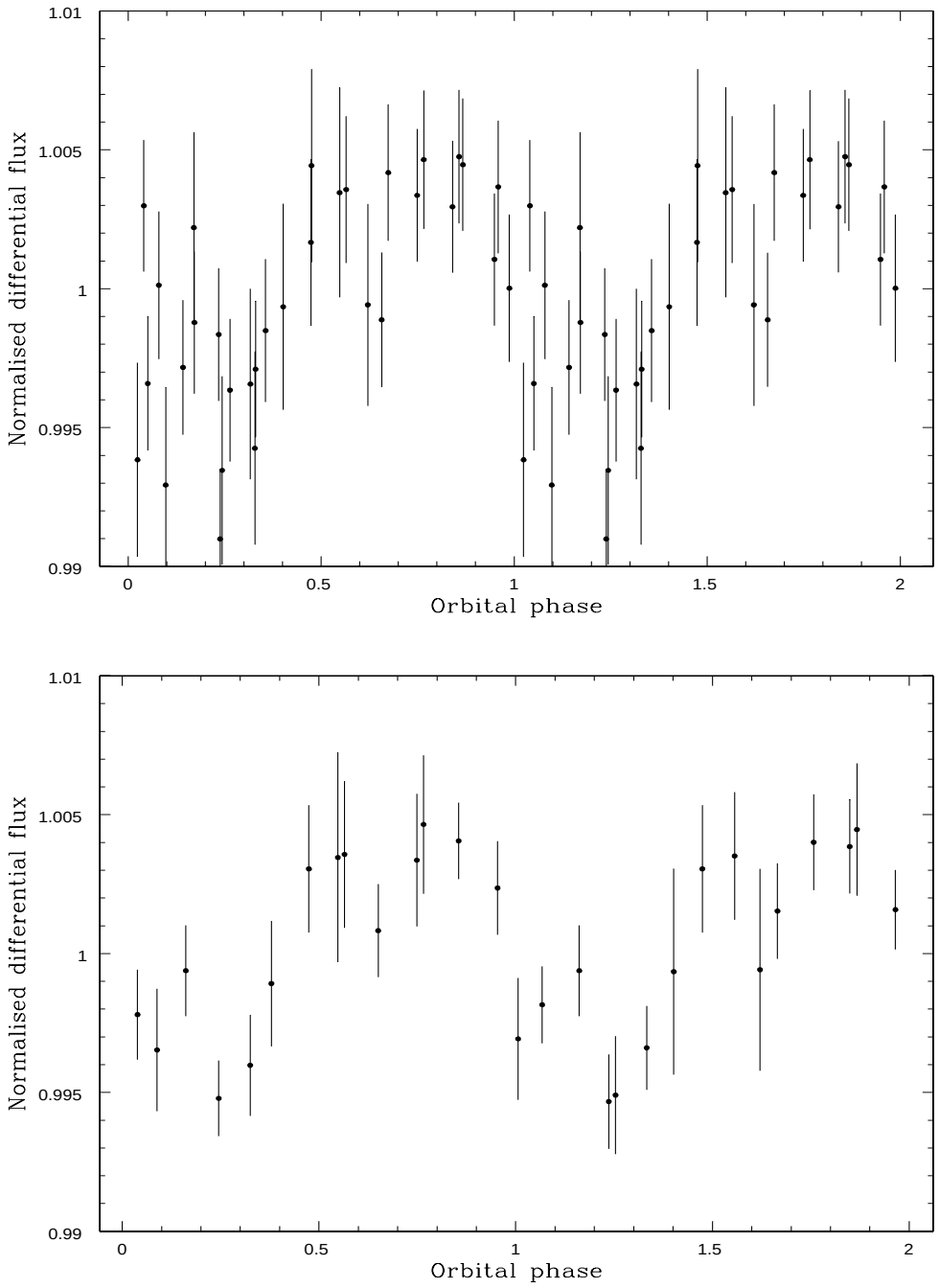

Figure 3.11: Light curves for G99-47 folded on the best fitting period from the periodogram (P = 26.8 mins). Lower plot is binned by a factor of 2.

3.4.2.2 G195-19

Angel (1978) reported a rotational period from polarisation of G195-19 of P = 1.33096 ± 0.00012 days. We have failed to find photometric modulation at the same period (see top of Fig. 3.13, but can confirm variability at a level of $\sim 4\%$. The period of the photometric variability has proved somewhat elusive. The global minimum of the periodogram is at 7.987 cyc/day and folding on this period initially looks promising, but it is a poor fit, with $\chi^2 = 525$ over 57 dof compared to a constant fit with $\chi^2 = 4915$ over 60 dof.

Moreover, this fit depends on a relatively large jump in flux ($\sim 4\%$) between the data taken in Feb and May 2003, which is not seen in either of the individual week-long data sets (Fig. 3.13). It is tempting to suspect only a long-term periodicity in this object, but constant fits through the individual week-long data sets have $\chi^2 = 174$ and $\chi^2 = 490$ over 26 and 33 dof respectively, indicating that G195-19 is almost certainly varying over a week. To test this, we removed the long-term variation by normalising the flux of the individual week-long data sets, then re-ran the periodogram on all the data. This gave a best-fitting frequency of 4.79 cyc/day (P = 5.01 hours), with $\chi^2 = 211$ over 58 dof. Again, we failed to find variability on the polarimetric period of 1.33096 days. The unmodified light curves folded on the polarimetric and our best-fitting periods are shown in Fig. 3.13, with the data points from each epoch plotted in different colours. Also shown is the normalised light curve, folded on the new best-fitting period. This is the only folded light curve to show a convincing variability not based on the flux difference between epochs. It is possible that there are two levels of variability in this object - one on short timescales and another over a period of $\sim$ months – years. More data are required on this object on both timescales.

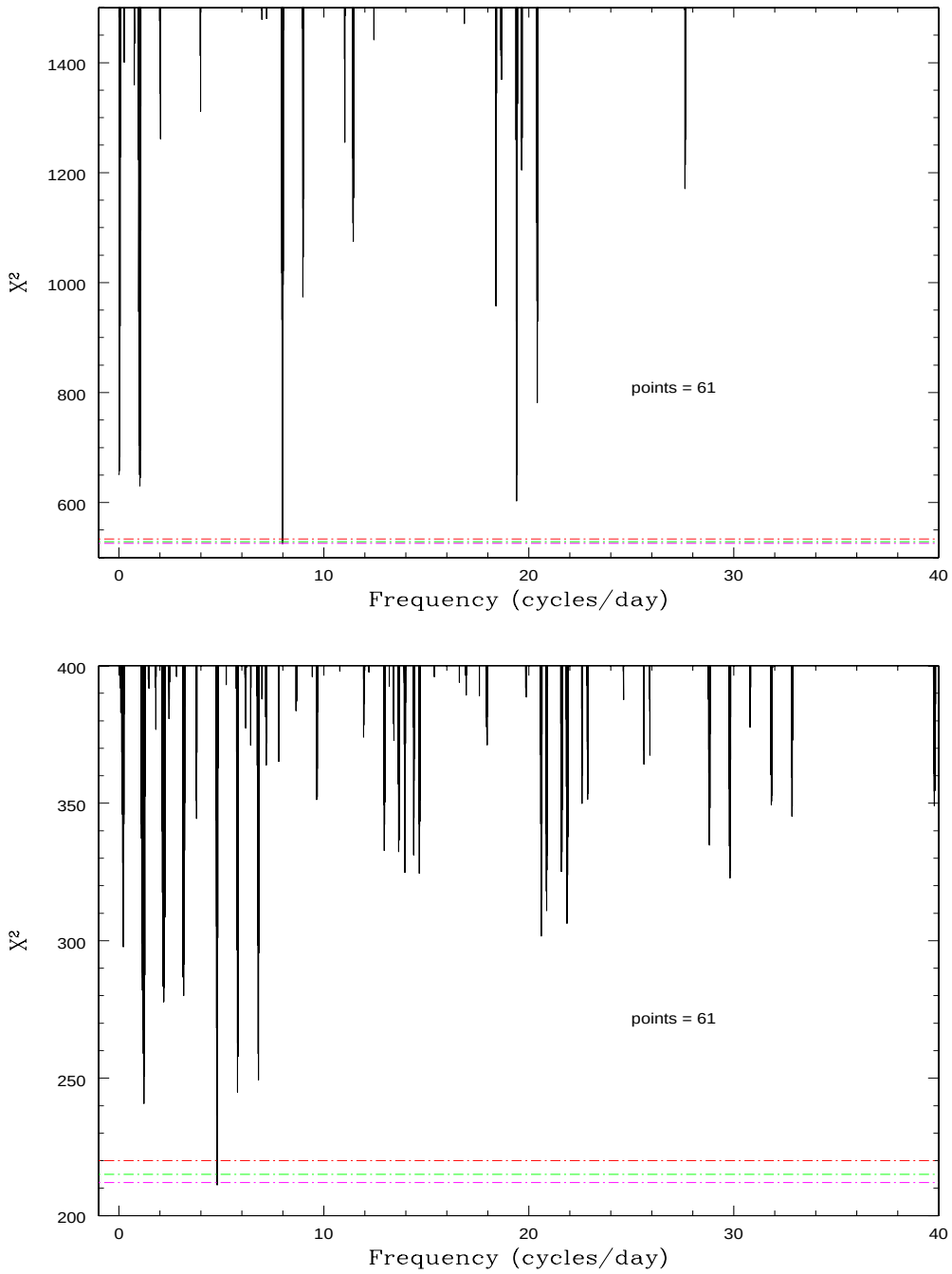

Figure 3.12: Top - periodogram for G195-19. Bottom - periodogram with the average flux of the separate epochs both normalised to 1, i.e. with the long-term variation removed.

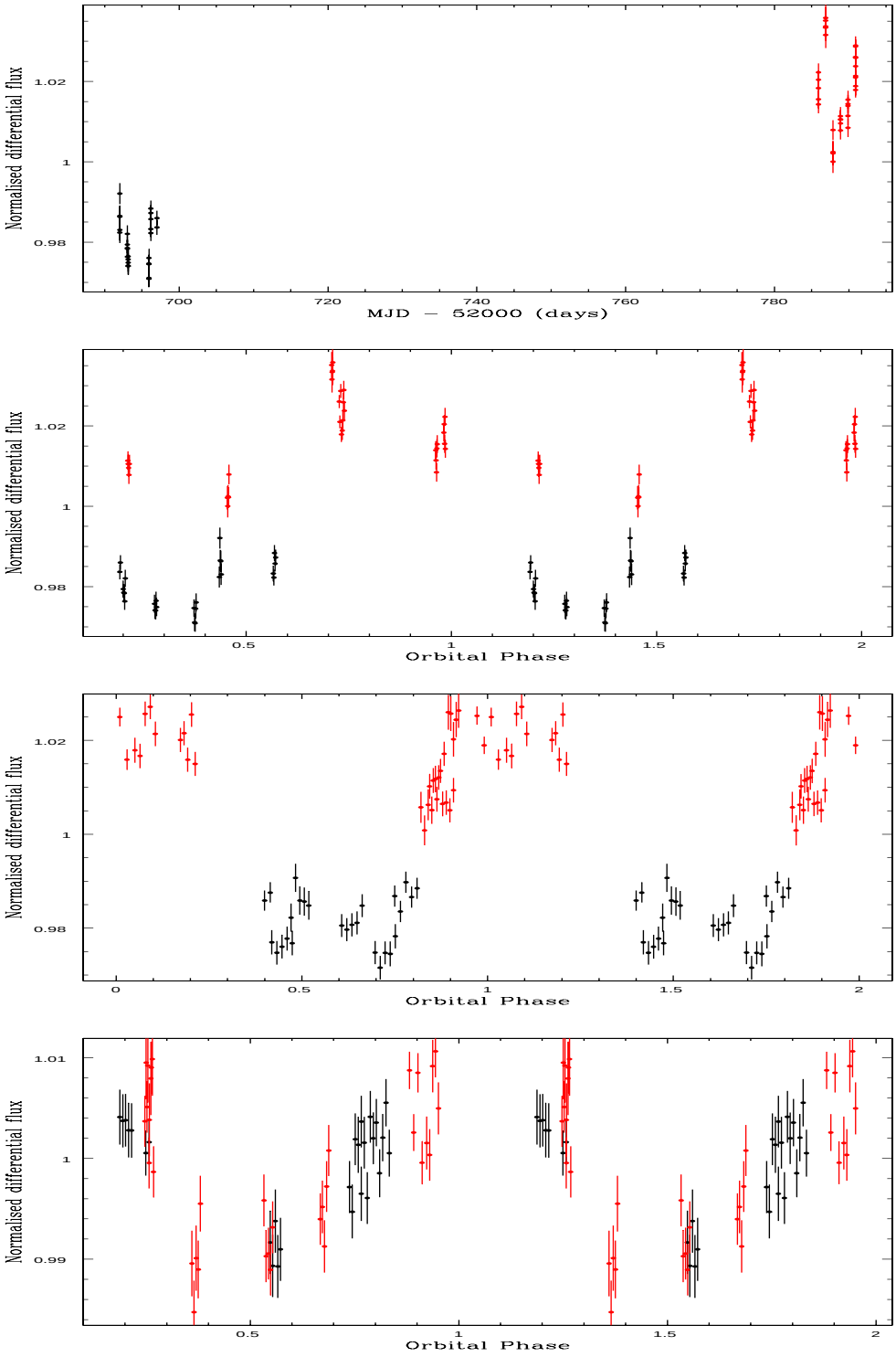

Figure 3.13: Top - unmodified data for G195-19, with different epochs plotted in different colours. The three plots below are the phase-folded light curves for G195-19. From the top down, they are the unmodified data folded on the old period from the literature (P = 1.33 days), the unmodified data folded on the best period P = 3.005 h, and the data with the long-term variation removed, folded on the new best-fit period of 5.796 hours.

3.4.2.3 G217-037

We observed G217-037 in August 2002. A constant fit to the data has $\chi^2 = 1977$ over 234 dof, compared to the periodogram which has a best-fitting frequency of 0.47 cyc/day (P = 2.12 days) with $\chi^2 = 713$ over 231 dof (Fig. 3.14). It is clear from this that the target is varying, although the best period is a poor fit and is dependent on the jump in flux between the first and second nights (see folded light curve, Fig. 3.15). In order to check for other periods, we masked out that first night of data and re-ran the periodogram on the other 4 nights. We find a best frequency at 4.97 cyc/day (P = 4.83 hours) with $\chi^2 = 457$ over 186 dof compared to a constant fit of $\chi^2 = 683$ over 189 dof. Again this indicates that the target is variable, but again the best period is a poor fit. The folded light curve with all the data (including the masked first night) can be seen in Fig. 3.15. We conclude that this target is variable over the week, but we have been unable to find the period.

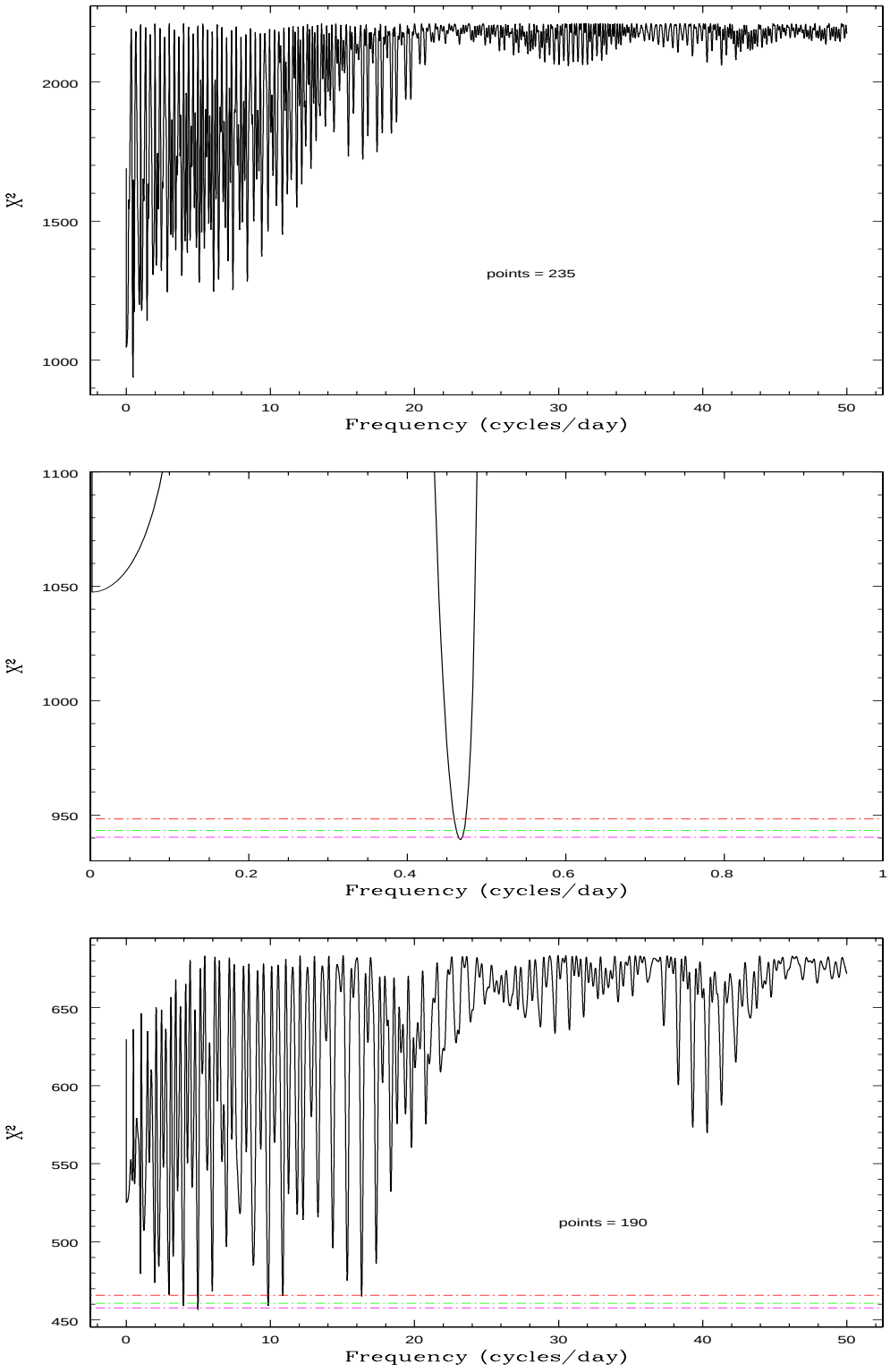

Figure 3.14: Top - periodogram for all the data for G217-037. Middle - periodogram zoomed in on the best-fitting period of P = 2.12 days. Bottom - periodogram for the last four nights of data only.

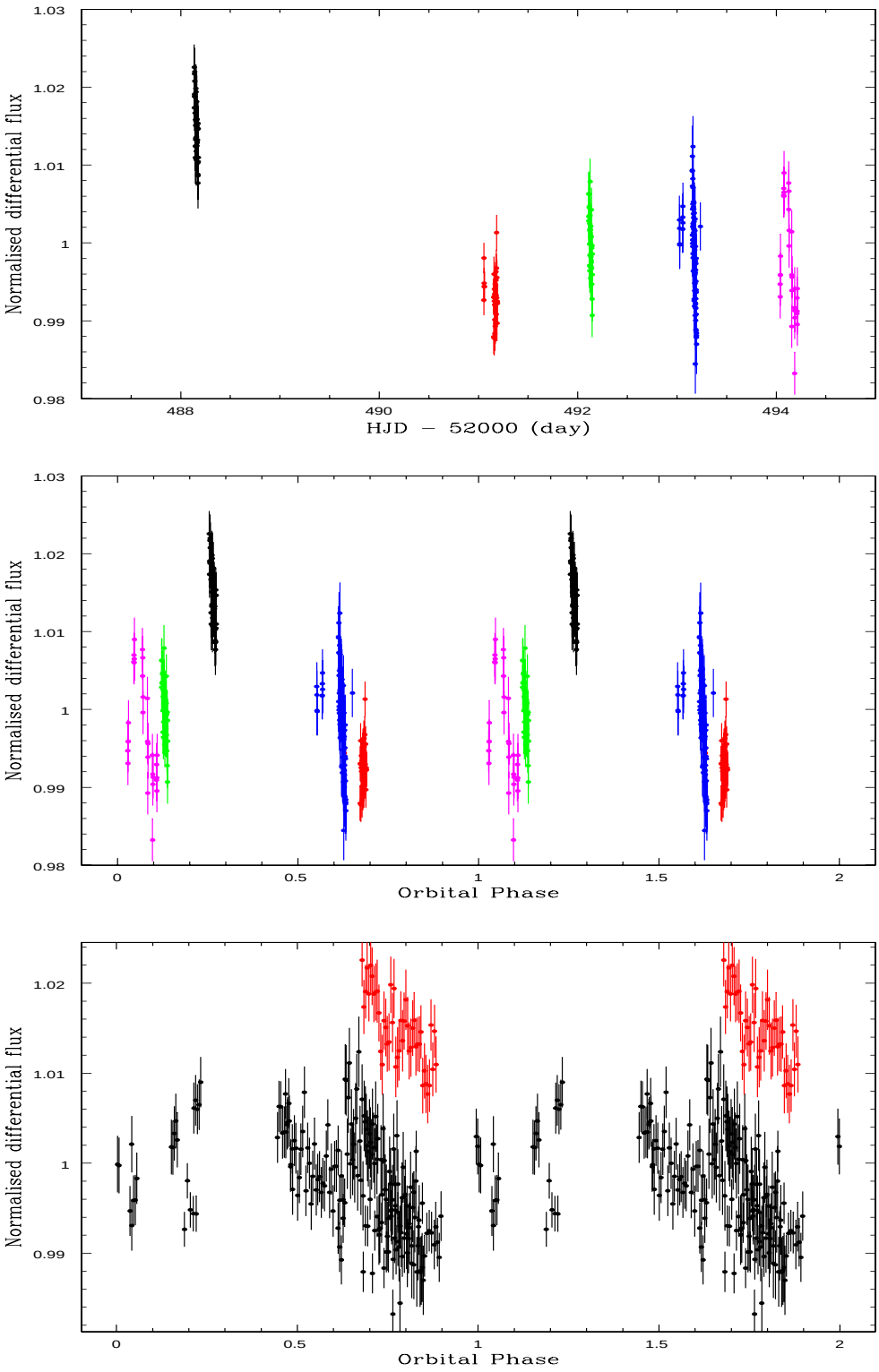

Figure 3.15: Top - data for G217-037 with different nights plotted in different colours. Middle - light curve folded on the best period for all the data of P = 2.12 days. Bottom - light curve folded on the best period for the last four nights (P = 4.8 hours). The first night's data is plotted in red.

3.4.2.4 G227-28

We find no evidence for variability in this object over short timescales, but find that G227-28 is almost certainly varying over the year. A constant fit to the data gives a χ^2 of 453 over 82 dof. The periodogram over the year suggests that long periods are favoured, and formally gives a better fit ($\chi^2 = 79$ over 78 dof, with P = 1.02 days), but the concentration of points over a small phase in the folded light curve (Fig. 3.16) suggests that this is not a true rotational period. In order to check for short periods we also ran a periodogram on the August data alone, which gave a period of 1.31 days with $\chi^2 = 54$ over 69 dof. A constant fit to the Aug 2002 data is not much worse at $\chi^2 = 66$ over 72 dof and the folded light curve again suggests that we have failed to find a real spin period for this source. We conclude that G227-28 is variable on timescales $\sim$ months – years, and have been awarded Liverpool Telescope time to monitor this object over the next 4 semesters.

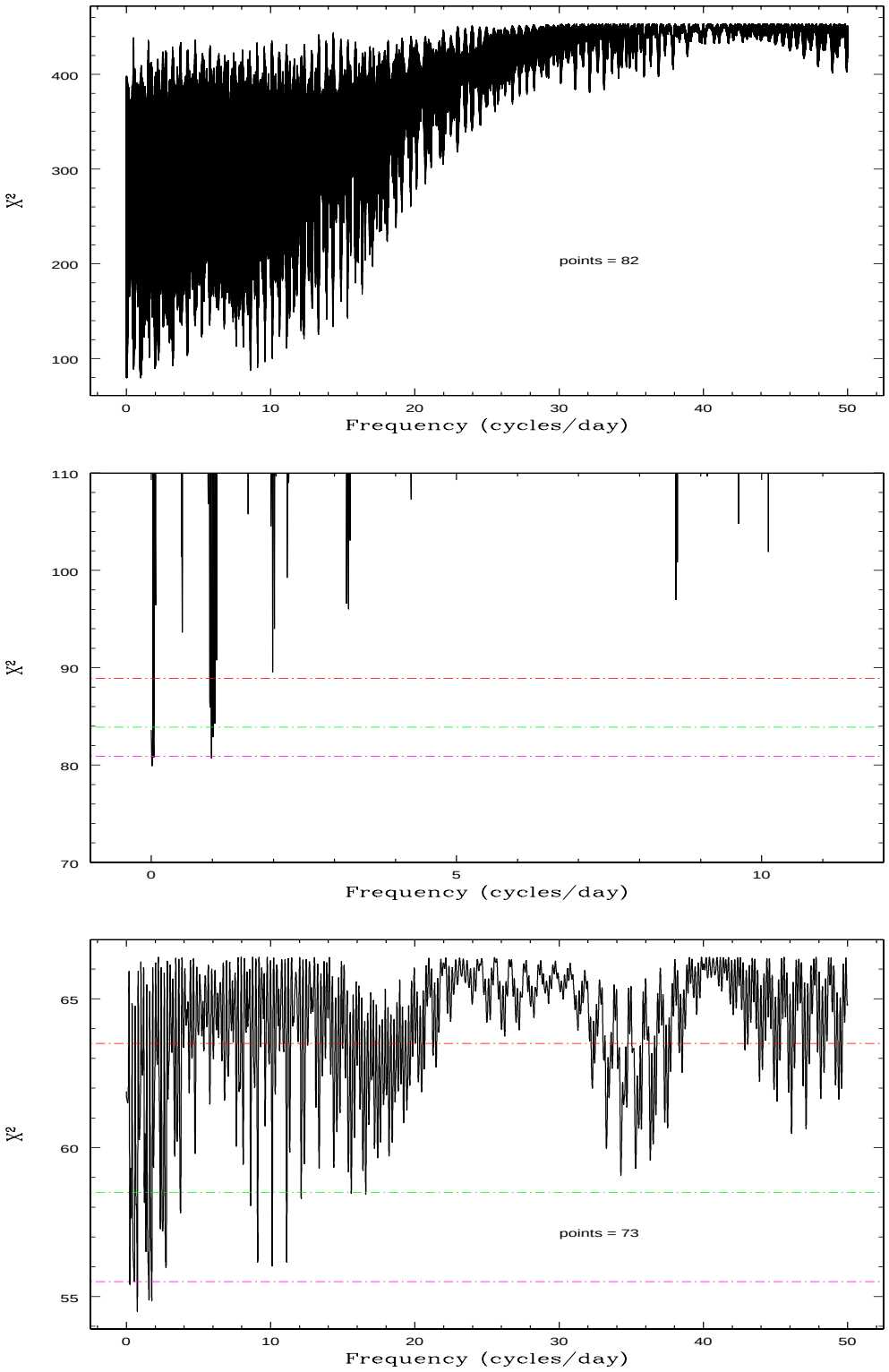

Figure 3.16: Top - periodogram for G227-28. Middle - periodogram zoomed in on the global χ^2 minimum. Bottom - periodogram for August data alone.

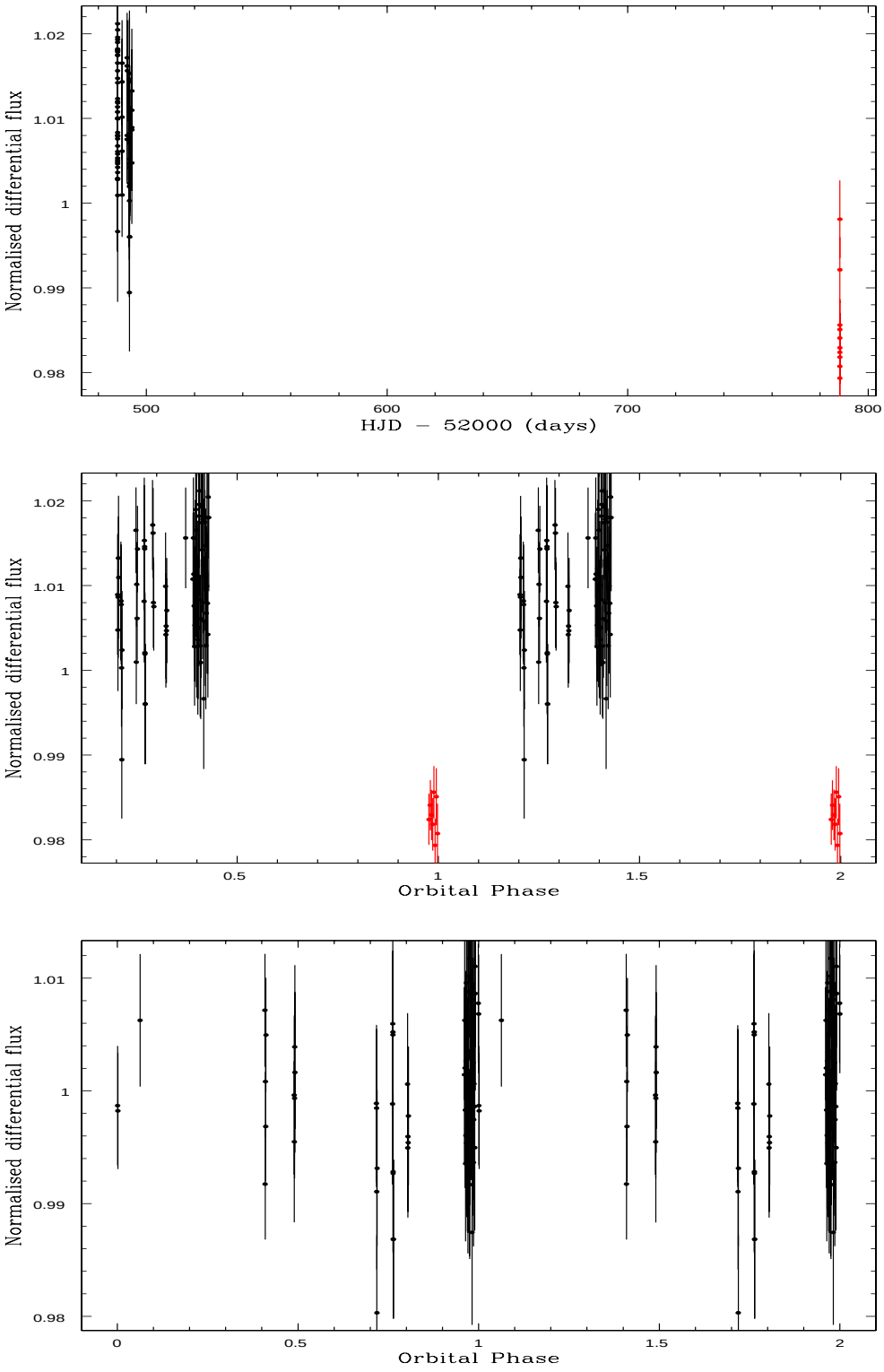

Figure 3.17: Top - all of the data on G227-28. Middle - light curve folded on the best period for all the data of P = 1.02 days. Bottom - August data only, folded on the best period of P = 1.31 days.

3.4.2.5 G234-4

We observed G234-4 on 3 nights in Feb 2003. We find that it is variable over the week above the level of the comparisons, with a scaled constant fit $\Delta\chi^2 = 20$ worse than the best-fit period (see top of Fig. 3.18 for a plot of the data), but we have been unable to derive a period of modulation. It can be seen from the periodogram, shown in Fig. 3.18, that the 3σ error covers most periods up to 50 cyc/day, and even the 1σ limit covers many periods. More data are required on this object.

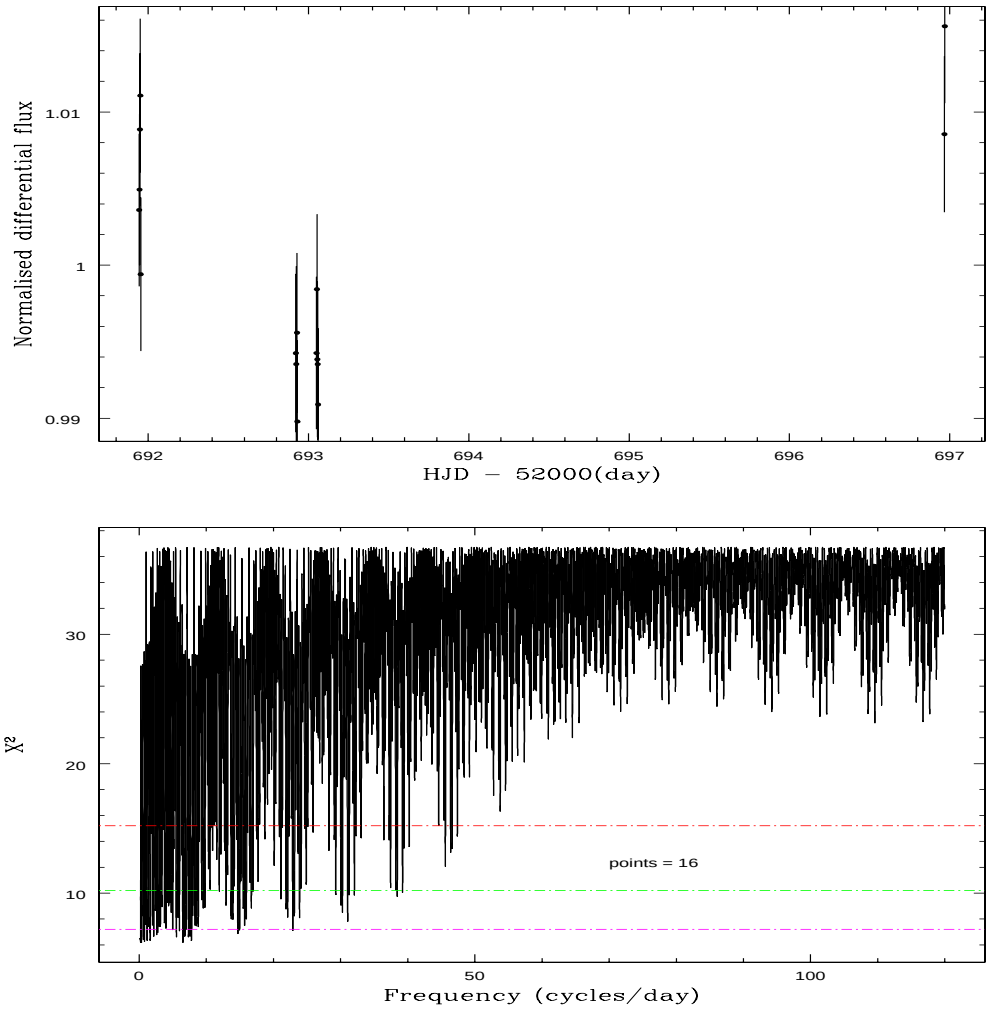

Figure 3.18: Top - plot of data on G234-4. Bottom - periodogram for G234-4.

3.4.2.6 G240-72

Berdyugin & Pirola (1999) reported extremely slow variability in the polarisation of this object, suggesting a rotational period of ≥ 100 years. We find no conclusive evidence for short-term variability in this star, as the RMS of the target light curve target is lower than the RMS of the comparisons. We do, however, see an increase in the differential flux of $\sim 2.5\%$ over the 10 months between Aug 2002 and May 2003, well above the RMS level of the comparisons, and the scaled χ^2 of the best-fitting period is $\Delta\chi^2 = 1382$ better than for a constant fit. The global minimum in the light curve for all the data is at 4.859 cyc/day (Fig. 3.19), although the general shape merely suggests long-term variability. When folded on the best period, the light curve is entirely dominated by the change in flux between epochs (Fig. 3.20). We also ran a periodogram on just the August data to check for short-term periodicity buried in the scatter. We found no significant minima below the Nyquist frequency and the χ^2 of a constant fit is 51 over 52 dof. We conclude that there is no evidence for short-term variability, but that this object is seen to vary over 10 months. We have been awarded Liverpool Telescope time to follow up this object over the next 4 semesters.

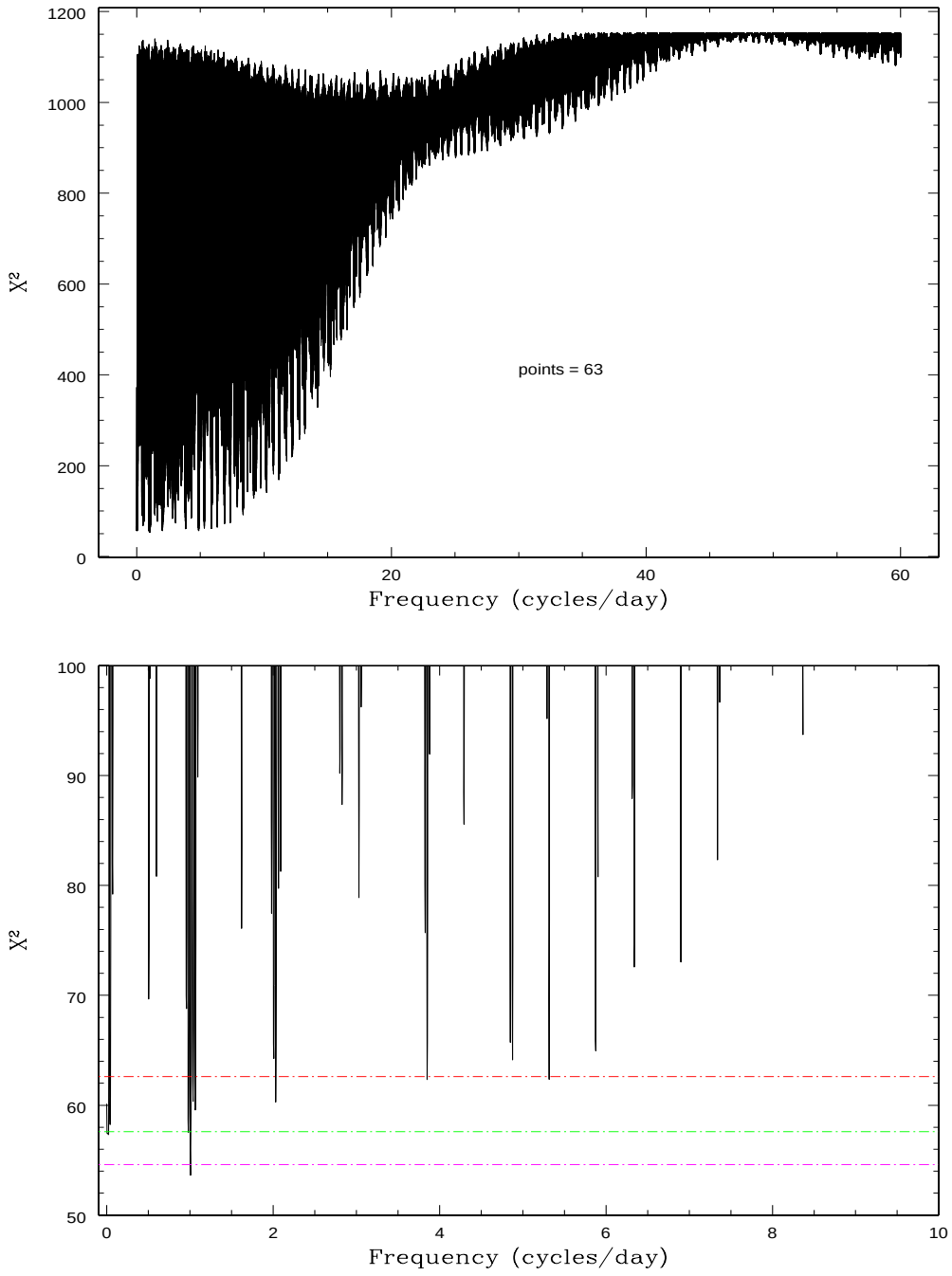

Figure 3.19: Top - periodogram for G240-72. Bottom - periodogram zoomed in on the global χ^2 minimum.

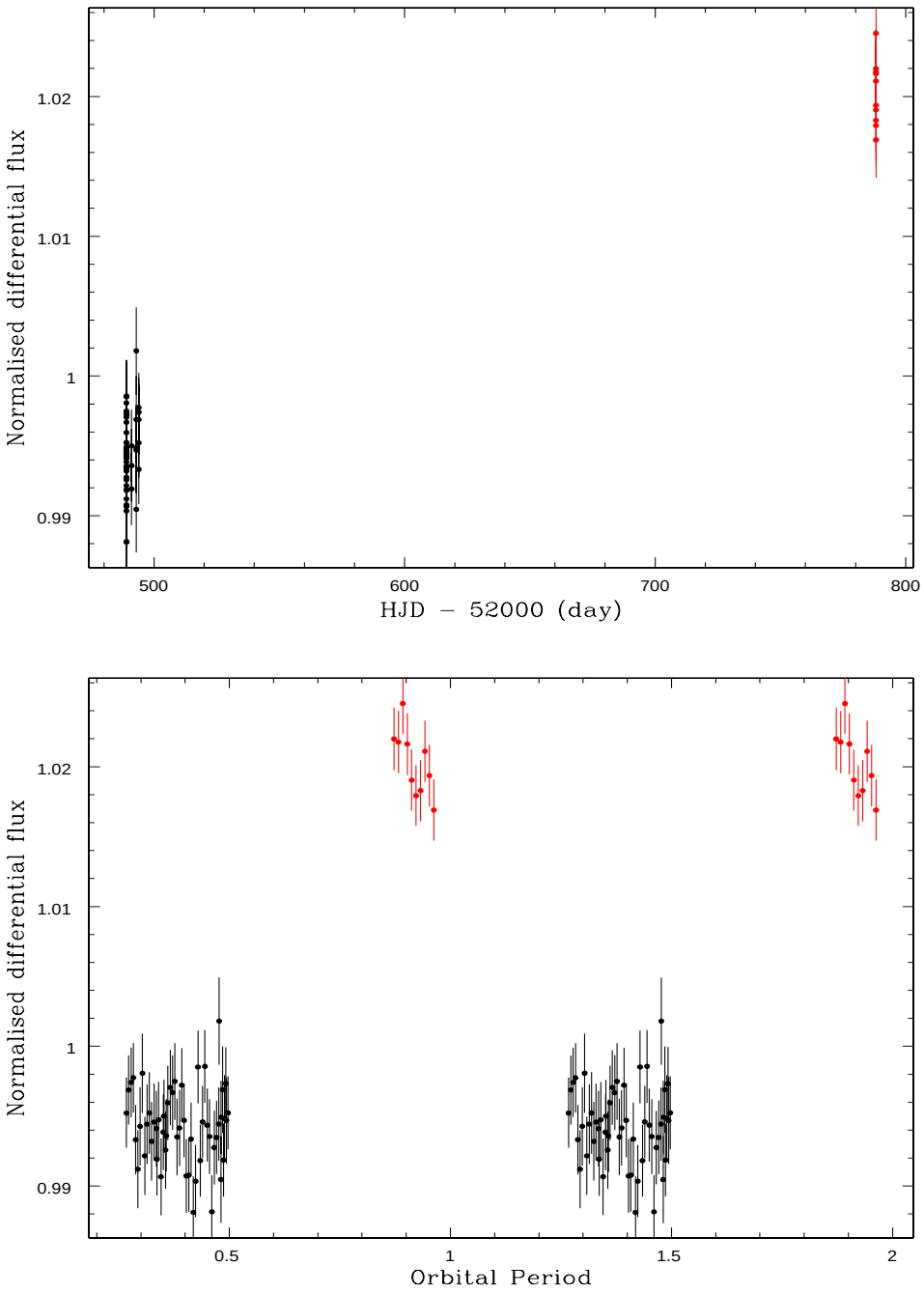

Figure 3.20: Top - data for G240-72. Bottom - the light curve folded on the best-fitting period of 4.9 hours is dominated by the difference in flux between epochs.

3.4.2.7 LB8827

We have discovered variability on LB8827 at a level of about 4%. The periodogram displays a heavy aliasing structure, which has made it difficult to select a best-fitting period. For the floating-fit periodogram, the global minimum occurs at a frequency of 2.11 cyc/day, with a χ^2 of 22 over 26 dof compared to a constant fit with $\chi^2 = 426$ over 29 dof. The light curve folded on this period looks reasonable, but the same can be said about the next 3 best-fitting frequencies, at 9.18, 1.04 and 4.17 cyc/day. We therefore also tested the data using a Lomb-Scargle periodogram, which showed a change in the best period, giving the two best-fitting frequencies as 9.18 & 4.17 cyc/day. We conclude that LB 8827 is variable, with a period between 2 h – 1 day. Light curves folded on the 3 best-fitting frequencies of 2.11, 9.18 and 4.17 cyc/day (P = 0.47 d, 2.6 h and 5.8 h respectively) are shown in Fig. 3.22.

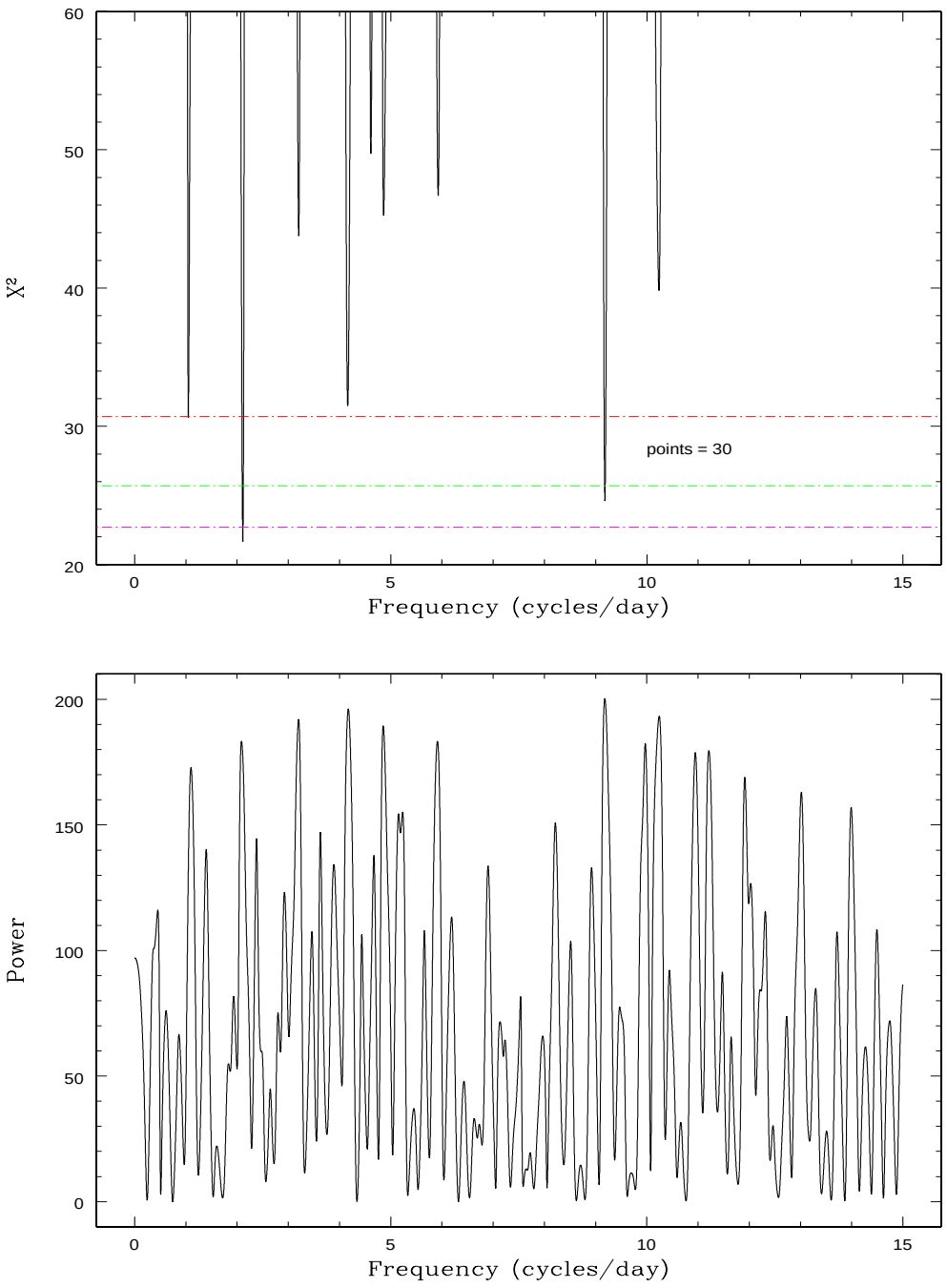

Figure 3.21: Top - floating fit periodogram for LB8827. Bottom - Lomb-Scargle periodogram showing a different best-fitting frequency

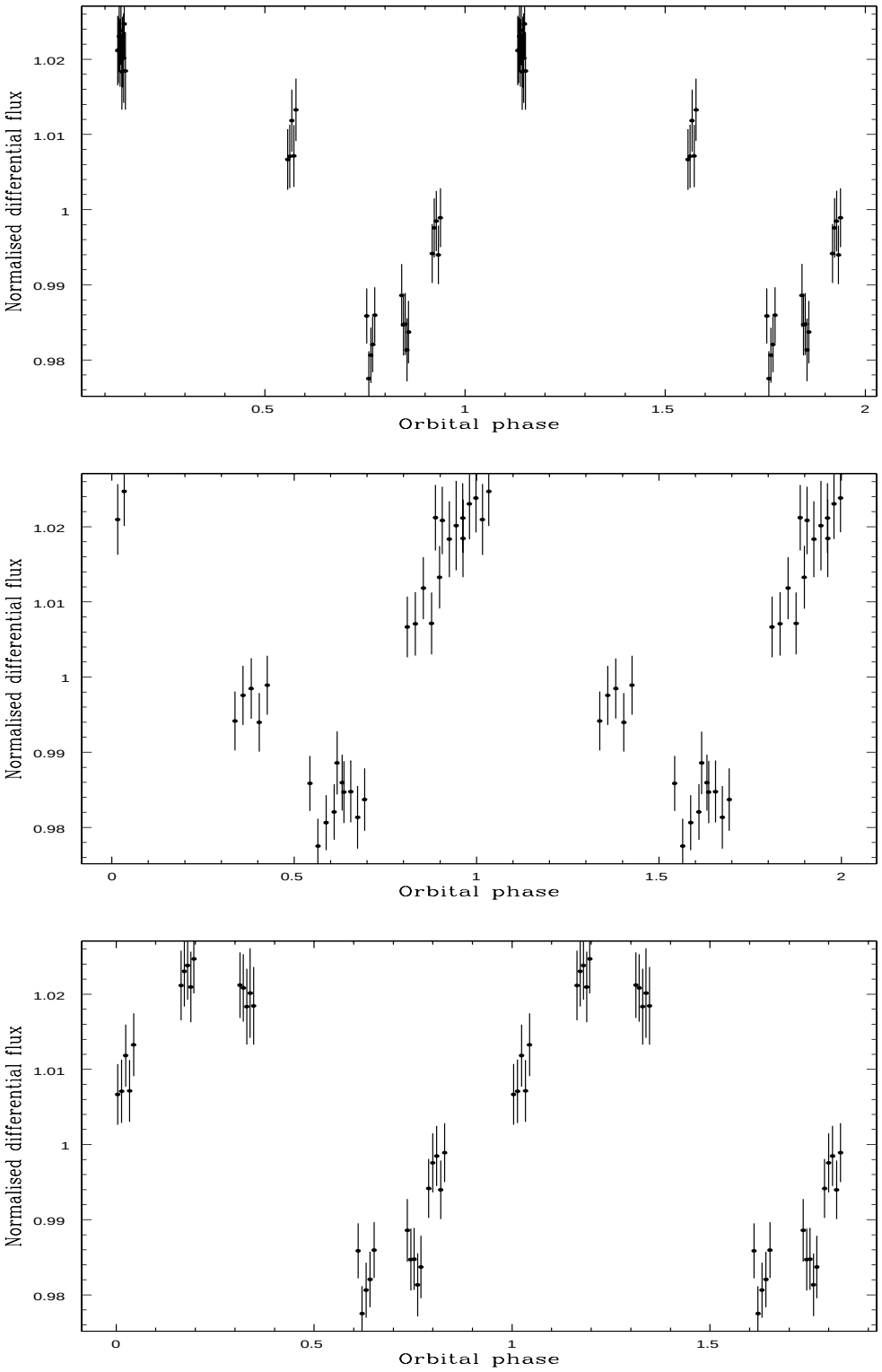

Figure 3.22: Phase-folded light curves for LB8827. From the top down, the light curves are folded on the three best-fitting periods of 0.47 days, 2.6 hours and 5.8 hours.

3.4.2.8 LHS2273

See Fig. 3.23 for the periodogram and folded light curve. This source was observed over 5 nights during May 2003. We find that LHS 2273 is variable well above the level in the comparison stars, and the scaled χ^2 in the periodogram is an improvement of $\Delta\chi^2 = 19$ over a constant fit. The periodogram shows several peaks within the 3σ error on the global minimum. Folding on the best period of 40.86 mins (35.24 cyc/day) gives a reasonable folded light curve, shown at the bottom of Fig. 3.23. We conclude that LHS2273 is probably varying, with a period around 35 – 45 mins.

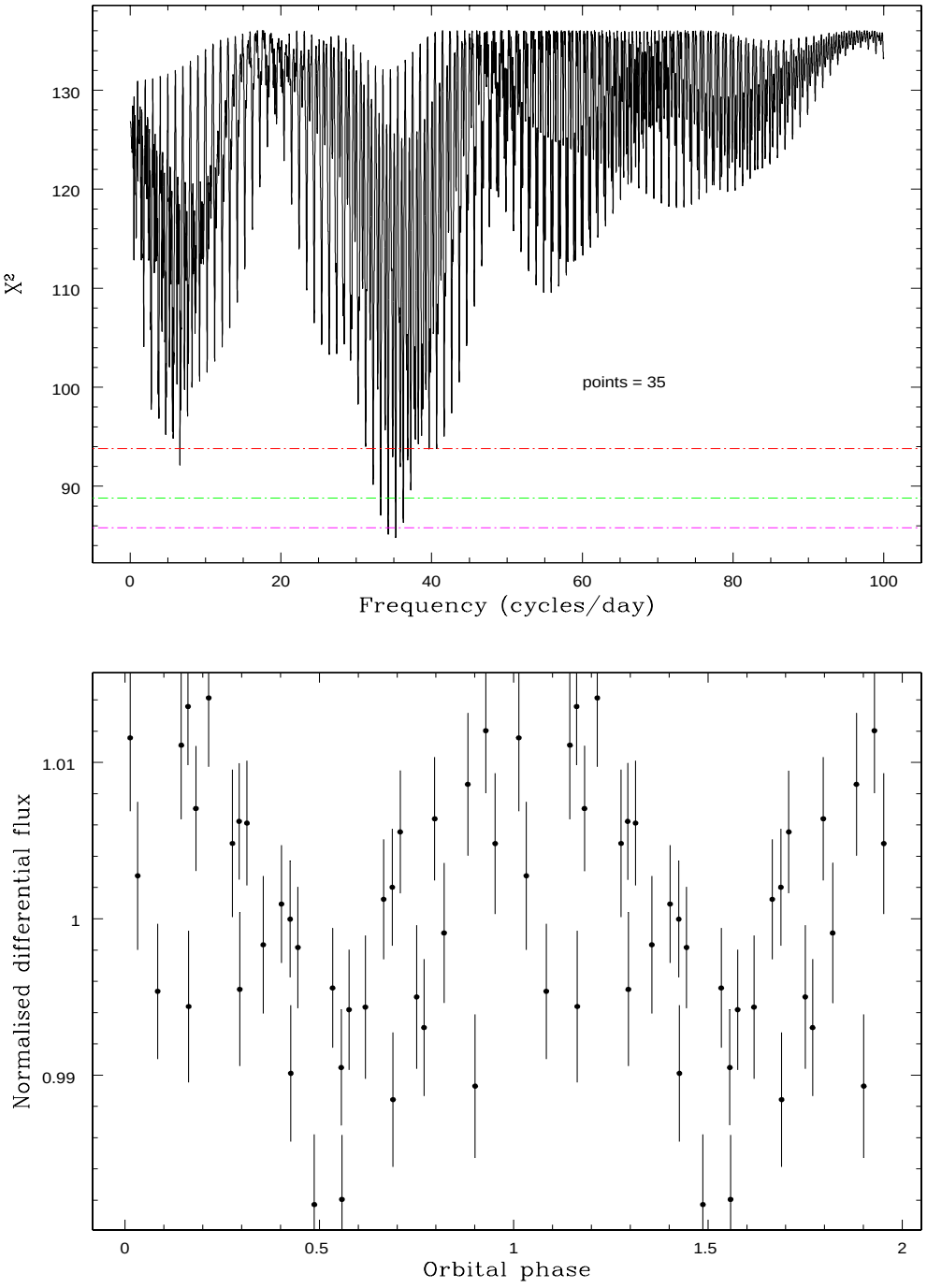

Figure 3.23: Top - periodogram for LHS2273. Bottom - light curve folded on the best period of 40.9 mins.

3.4.2.9 LHS5064

See Fig. 3.24 for the periodogram and light curve. We observed LHS5064 over 5 nights in Feb 2003 and have discovered significant photometric variability in the star, on a level of about 4.5%. The best-fit period is 1.645 cyc/day ($\chi^2 = 32$ over 29 dof), corresponding to a period of 14.6 hours. This is an improvement in χ^2 of 344 compared to a constant fit. A Lomb-Scargle periodogram gives the same best-fitting period. When folded on this period, the light curve looks approximately sinusoidal, although there are a number of other periods around the best-fit value which are within the 3σ error and give plausible folded light curves. We conclude that LHS5064 is variable, with a period of between 9 hours and 6 days, but a most likely period of $\sim$15 hours.

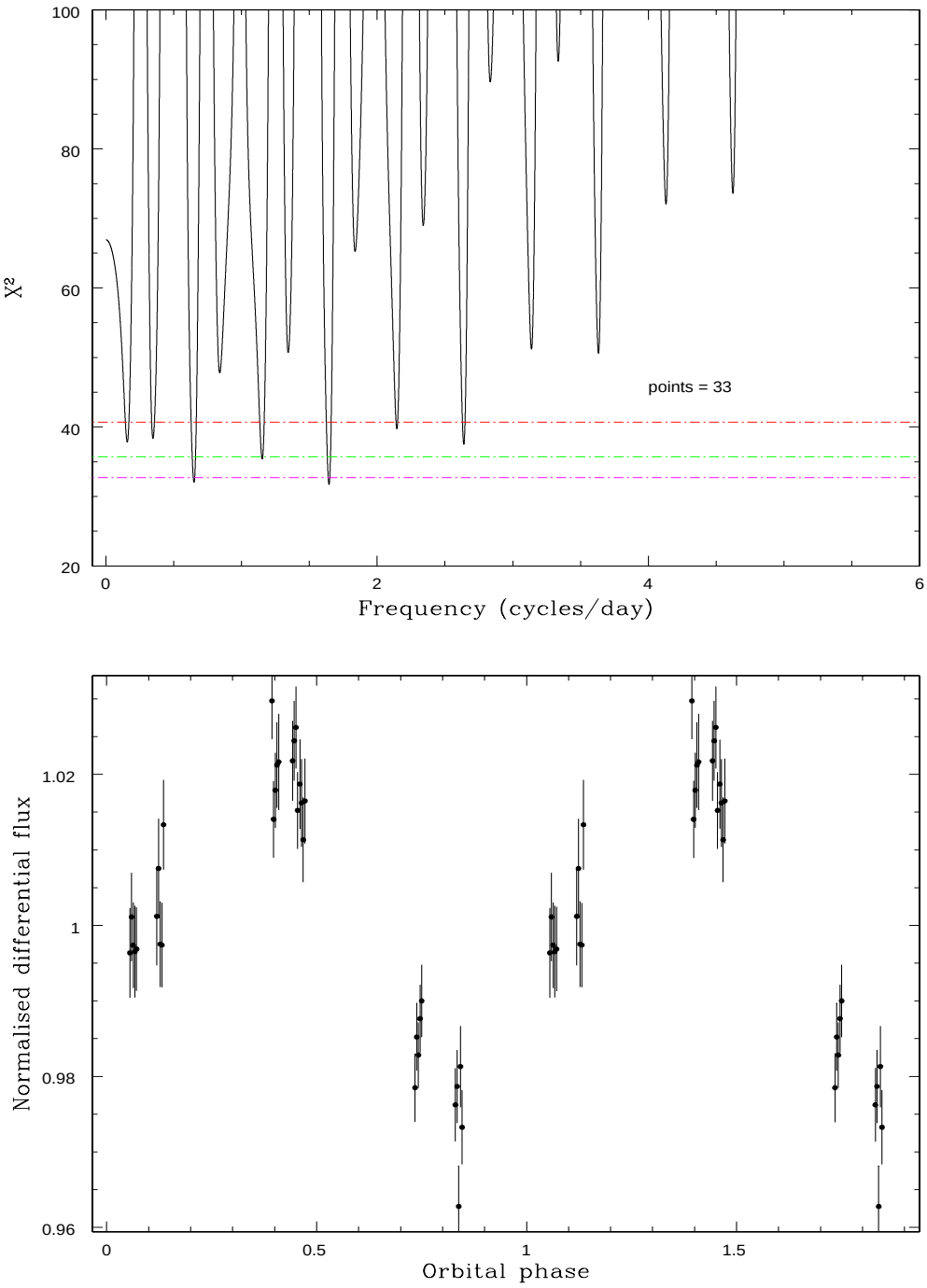

Figure 3.24: Top - periodogram for LHS5064. While the best frequency is at 1.65 cycles/day, there are a number of other signals within an error of 3σ. Bottom - light curve folded on the best period of 14.6 hours.

3.4.2.10 LP907-037

See Fig. 3.25 for a plot of the data. The differential light curve of LP907-037 shows variability in this object at a level of $\sim 2\%$, but we find that the comparison stars are also varying with respect to each other at the lower, but not insignificant level of $\sim 1.2\%$. While we conclude that the variability in the target is real as it is above the RMS level in the comparisons, we are cautious in identifying a rotational period for this source as the comparisons may affect the results from the periodogram. Formally, the best-fitting period is at P = 6.7 hours, with a scaled improvement of $\Delta\chi^2 = 98$ compared to a constant fit. The periodogram and folded light curve are shown in Fig. 3.26

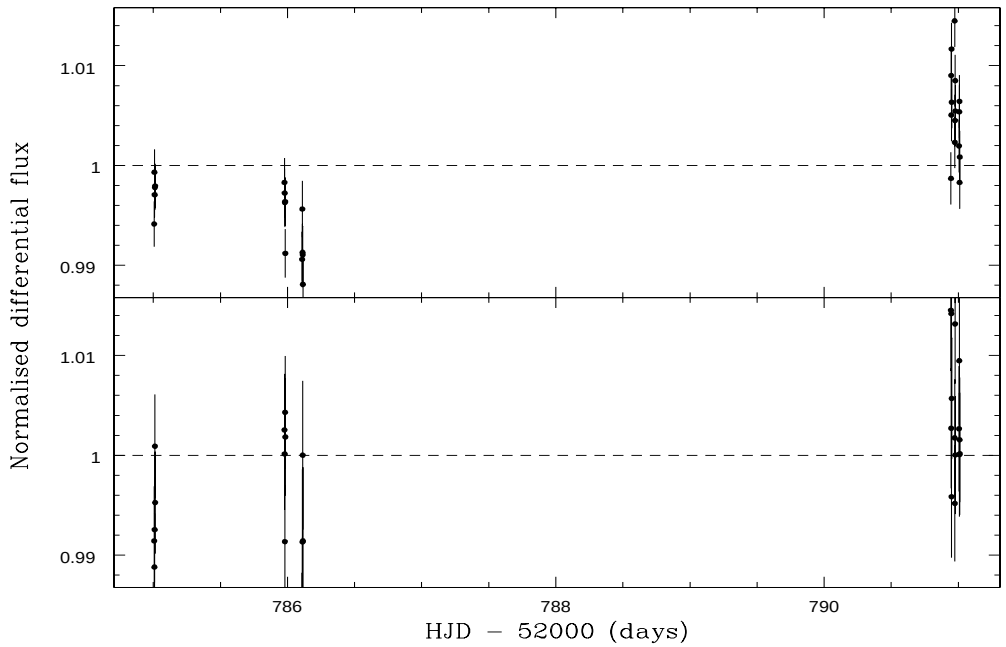

Figure 3.25: Differential light curves for LP907-037 vs comparison 2 (top) and comparison 2 vs comparison 3 (bottom).

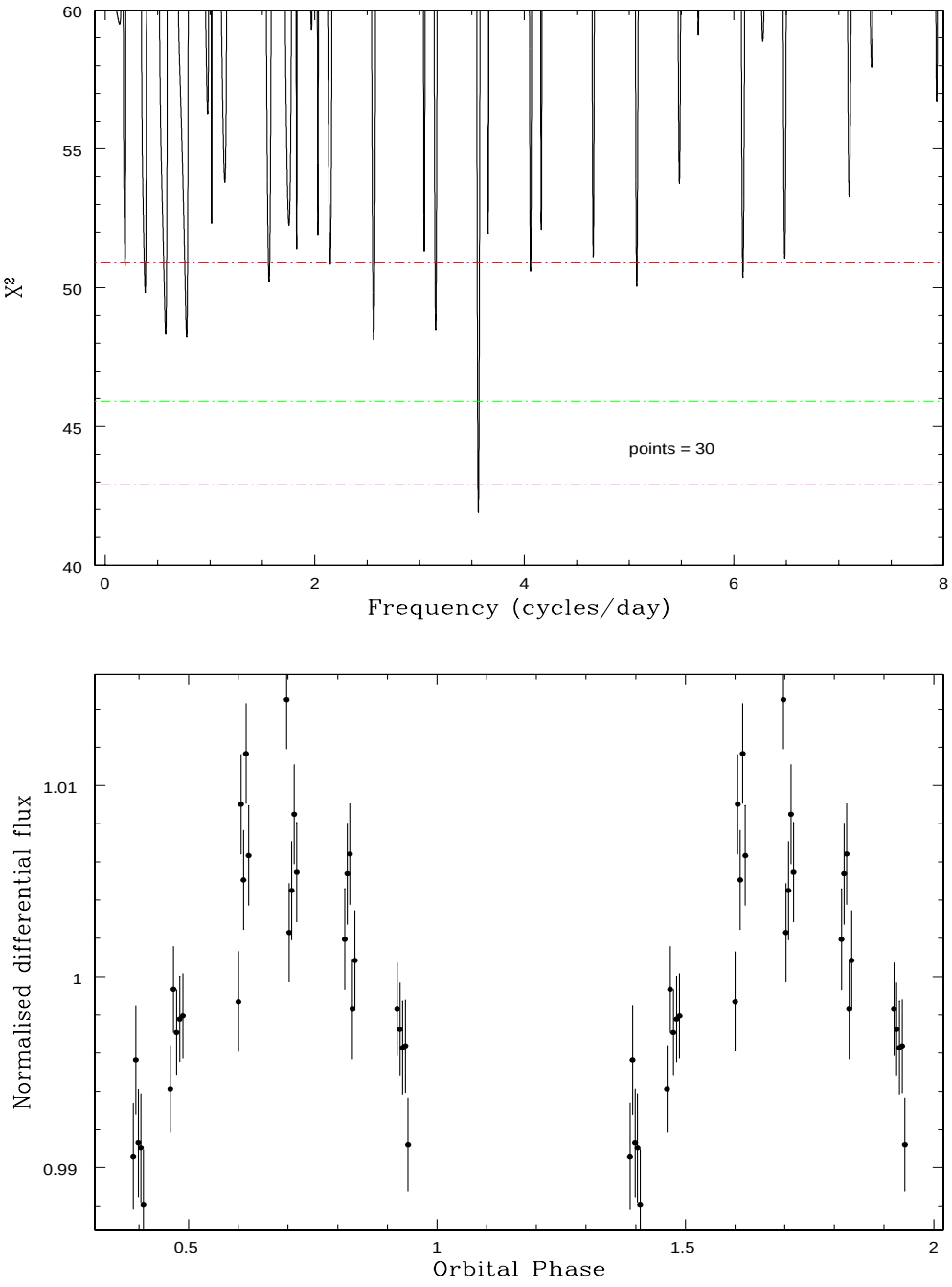

Figure 3.26: Periodogram and folded light curve for LP907-037

3.4.2.11 PG1658+441

PG1658+441 was observed during August 2002 and again, briefly, in May 2003. We find that the star is variable above the level in the comparison stars, and the χ^2 of a constant fit is 363 over 63 dof, while the global minimum in the periodogram has a χ^2 of 77 over 60 dof (Fig. 3.27). We find that there are several peaks in the periodogram within 3σ of the χ^2 minimum. When folding the light curve on these periods, we find that they all rely on a shift in the mean flux between the two datasets (see Fig. 3.28), seen in the clumping of the data from the two epochs, and therefore probably do not represent a real rotational period. We therefore simply conclude that PG1658+441 is probably variable with a period between 6 hours and 4 days.

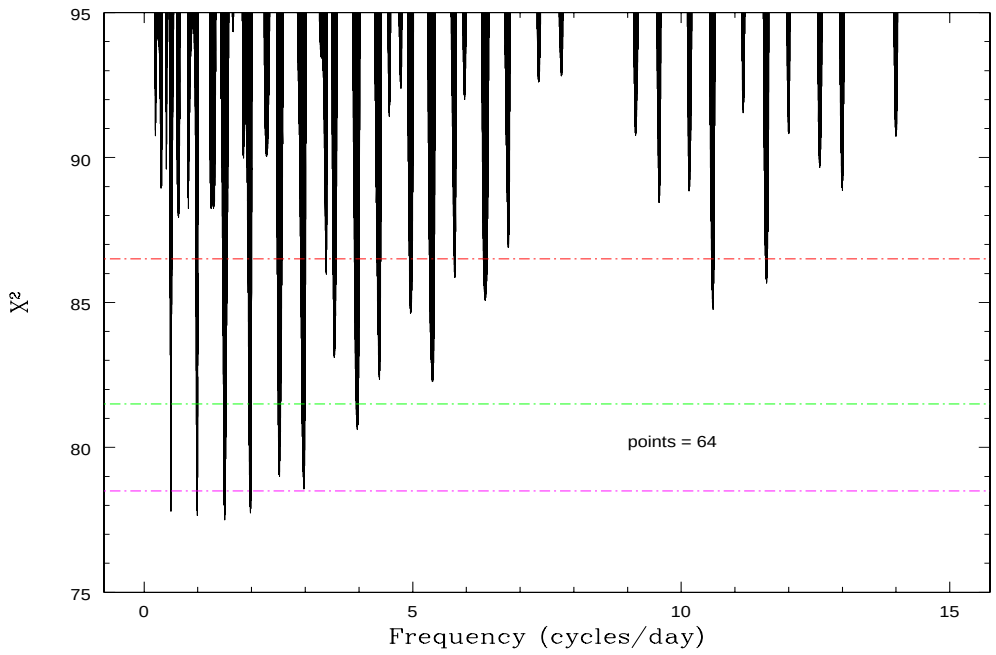

Figure 3.27: Periodogram for PG1658+441. We have been unable to construct a decent folded light curve for this source, so simply conclude that it is probably varying with a period between 6 hours and 4 days.

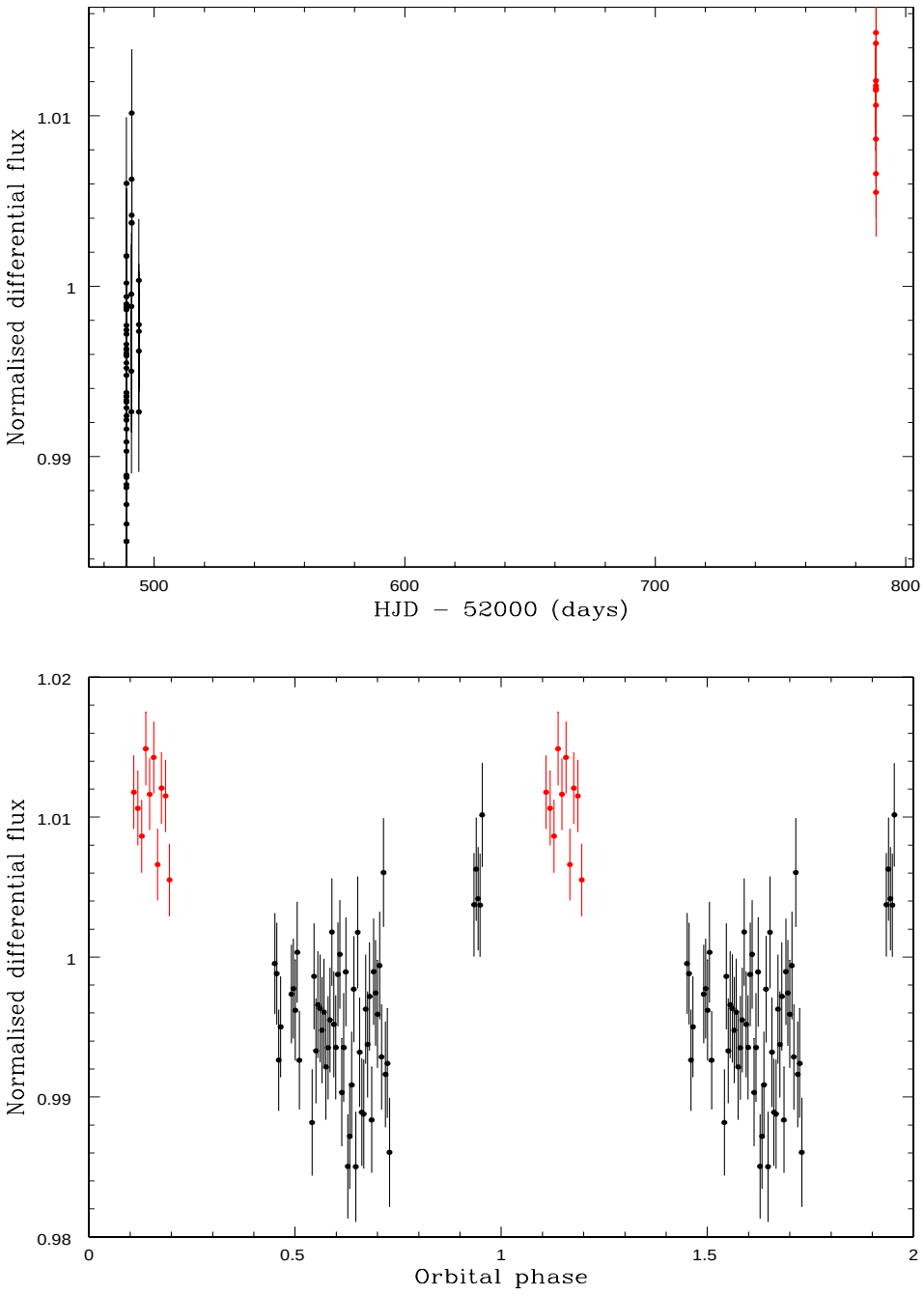

Figure 3.28: Top - data for PG1658+441, with the two separate datasets marked in different colours. Bottom - folded light curve with the datasets marked in the same colours as before. It can be seen from the clumping of the two datasets that this period detection relies on a shift in mean flux between the two epochs, and therefore is probably not a genuine rotational period.

3.4.2.12 PG2329+267

PG2329+267 was observed over the week in August 2002, and again, briefly, in May 2003 to check for long-term variability. A constant fit through the data gives a χ^2 of 483 over 152 dof, suggesting that the system is varying. However, the global minimum in the periodogram (P = 20.3 hours) has a χ^2 of 339 over 148 dof, so is a poor fit (Fig. 3.29). Since the scaled χ^2 for the sinusoidal fit is $\Delta\chi^2 = 237$ better than for a constant fit, we conclude that the system is varying. The light curve folded on the best period for all the data looks terrible (Fig. 3.30, top), so we cut out the May data to check for periodicity over the week only. This shifted the best period to P = 1.8 hours, with a χ^2 of 324 over 145 dof. The folded light curve for the August data looks good and is shown in Fig. 3.30. Due to the poor χ^2 of the sinusoidal fit we are cautious in claiming a definite period for this object, but conclude that we have detected variability in PG2329+267 with a probable period of P = 1.8 hours.

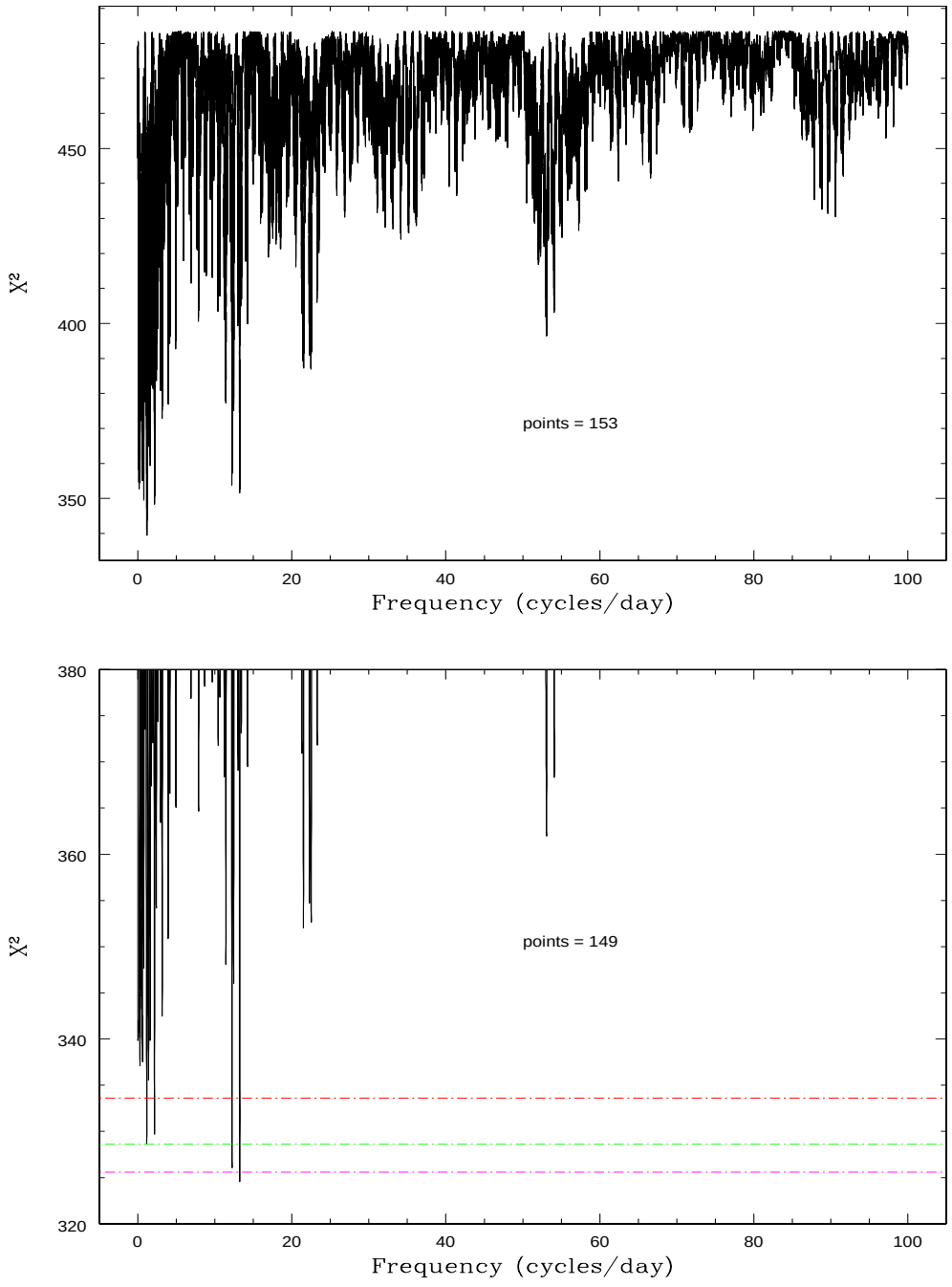

Figure 3.29: The periodograms for all of the data on PG2329+267 (top) and for the August data only (bottom).

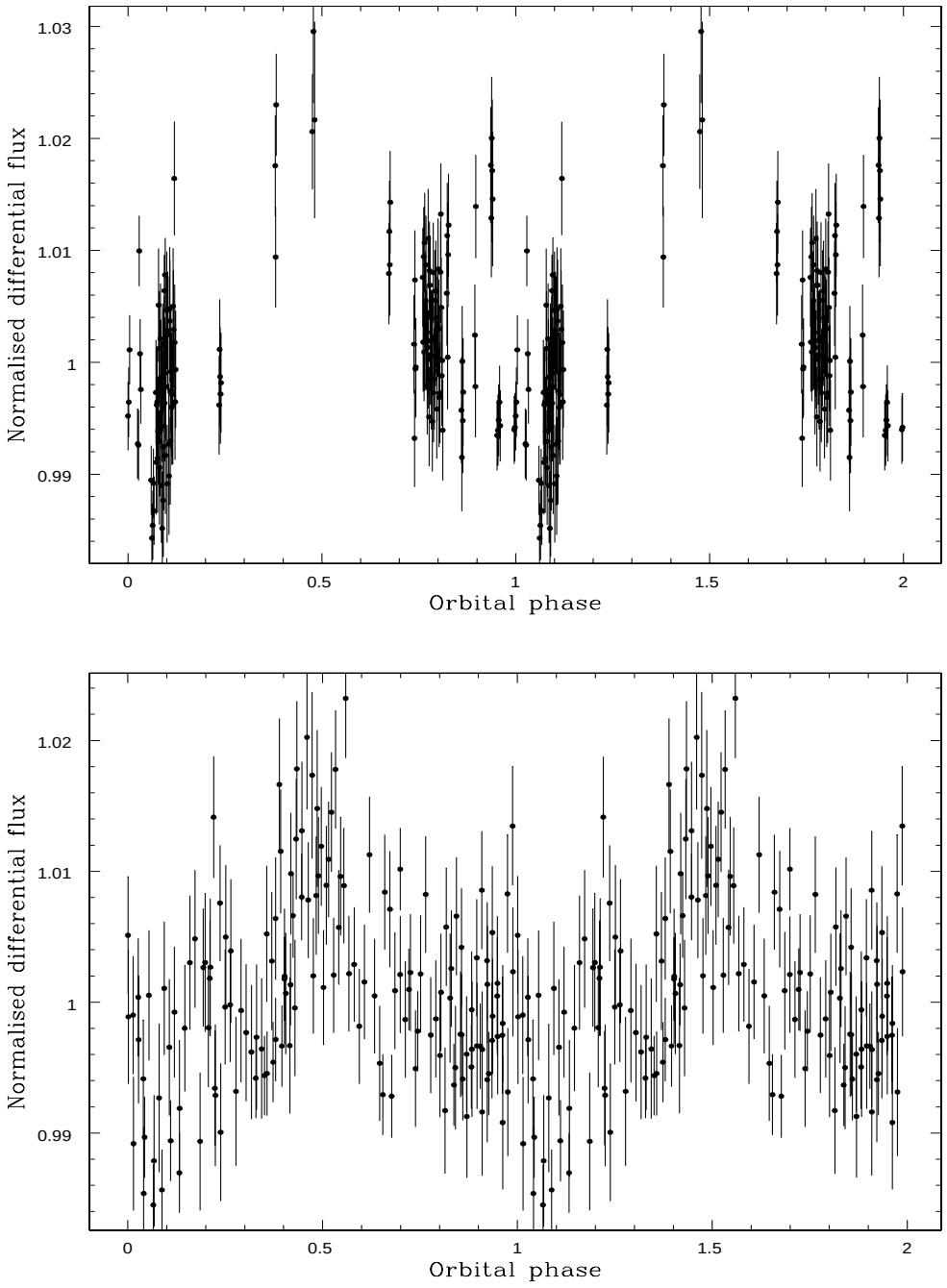

Figure 3.30: The light curves folded on the best period for all of the data (top, P = 20.3 hours) and for the August data only (bottom, P = 1.8 hours).

3.4.3 Targets with possible variability

3.4.3.1 EUVE J1439+75.0

(Vennes et al., 1999) found that this system is a double-degenerate, therefore we exclude it from the analysis of this survey. Unfortunately we were only able to extract photometry for one comparison star in the field due to bad pixels near the other comparison stars, and therefore we have no way of testing it for variability. We are unable to derive any conclusions from our data. The light curve of EUVE J1439+75.0 is shown in Fig. 3.31 with respect to our only comparison star.

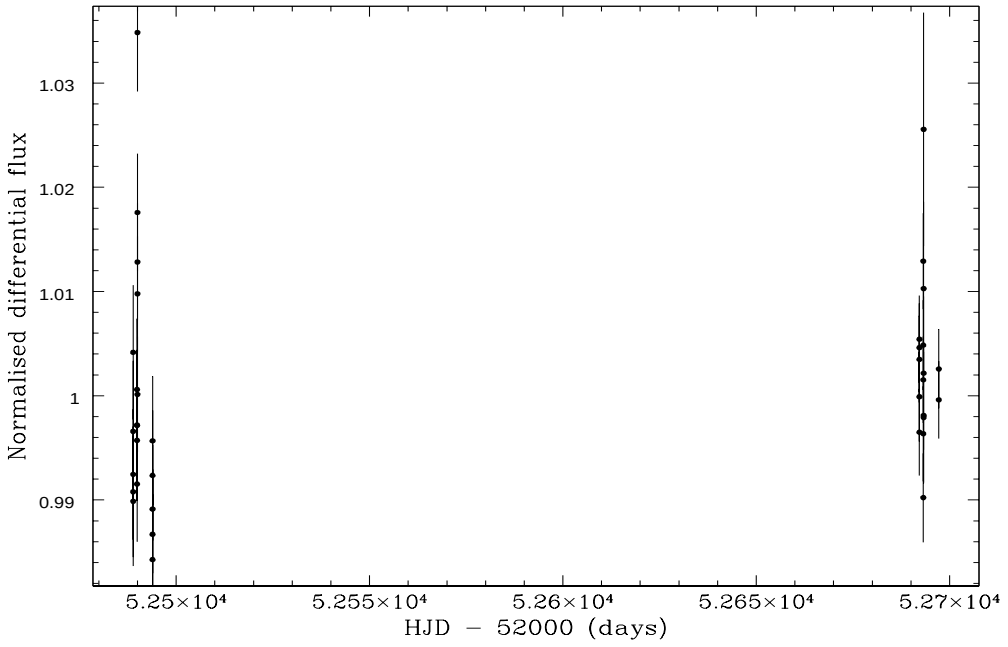

Figure 3.31: Light curve for EUVE J1439+75.0 vs our only comparison star. We cannot determine whether it is the target or the comparison that is varying.

3.4.3.2 G99-37

We observed this target during February 2003. Initially the source appeared to be variable, with a constant fit to the data of $\chi^2 = 39$ over 20 dof and a periodogram with a best-fitting frequency of 45.39 cyc/day and a $\chi^2 = 11$ over 17 dof (Fig. 3.32. The folded light curve can be seen in Fig. 3.33. However, upon closer inspection of the comparisons, we found that they also displayed low-level variability, with a similar amplitude and frequency. Folding the comparison star data on this frequency shows that the light curve is very similar to that of G99-37, so we conclude that the variability in this object is most likely to be due to the comparisons rather than a genuine intrinsic variability in the target. Unfortunately this means that we have been unable to test G99-37 for intrinsic variability.

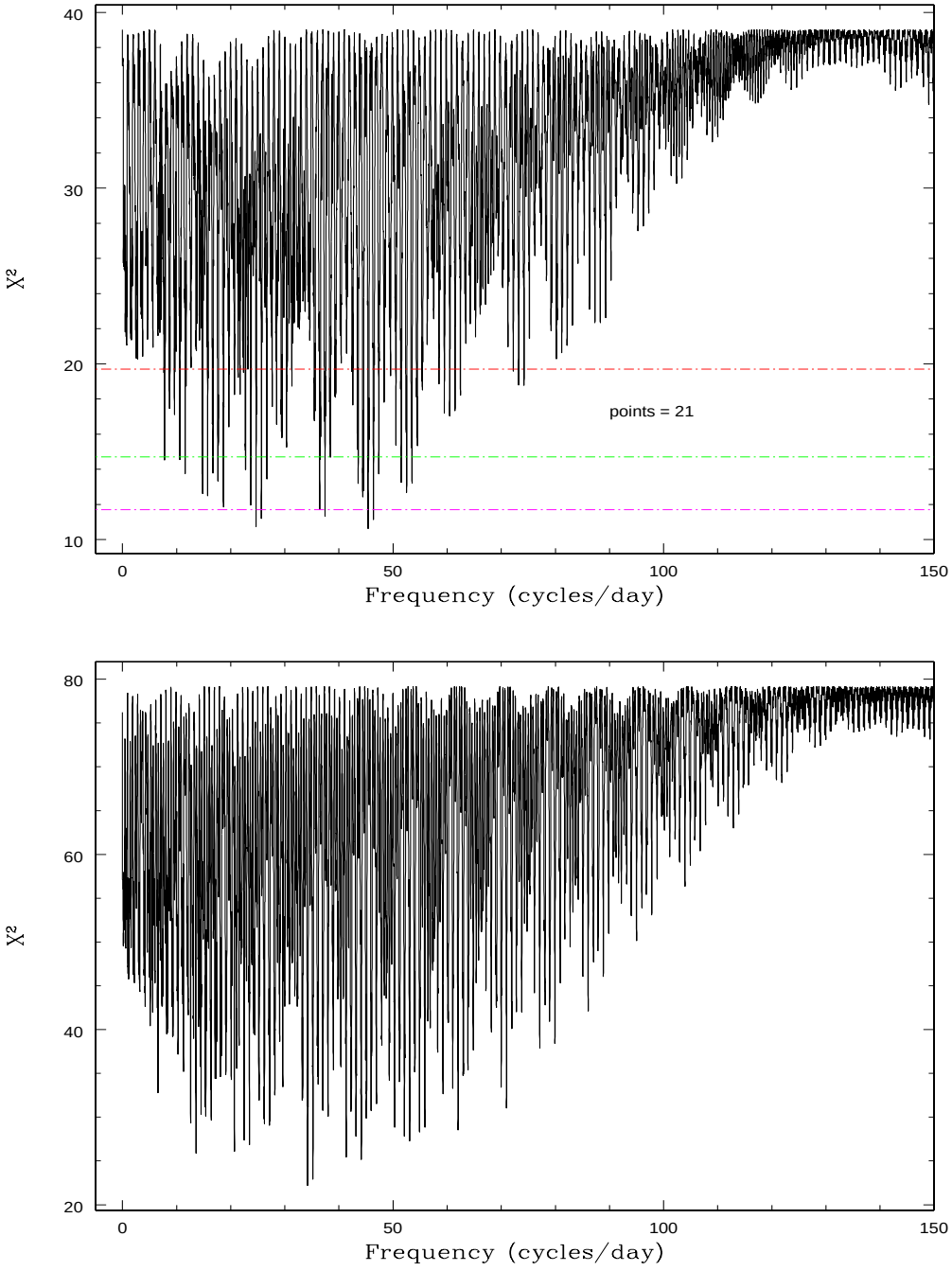

Figure 3.32: Top - periodogram for G99-37. Bottom - periodogram for comparison star 2 vs comparison star 3.

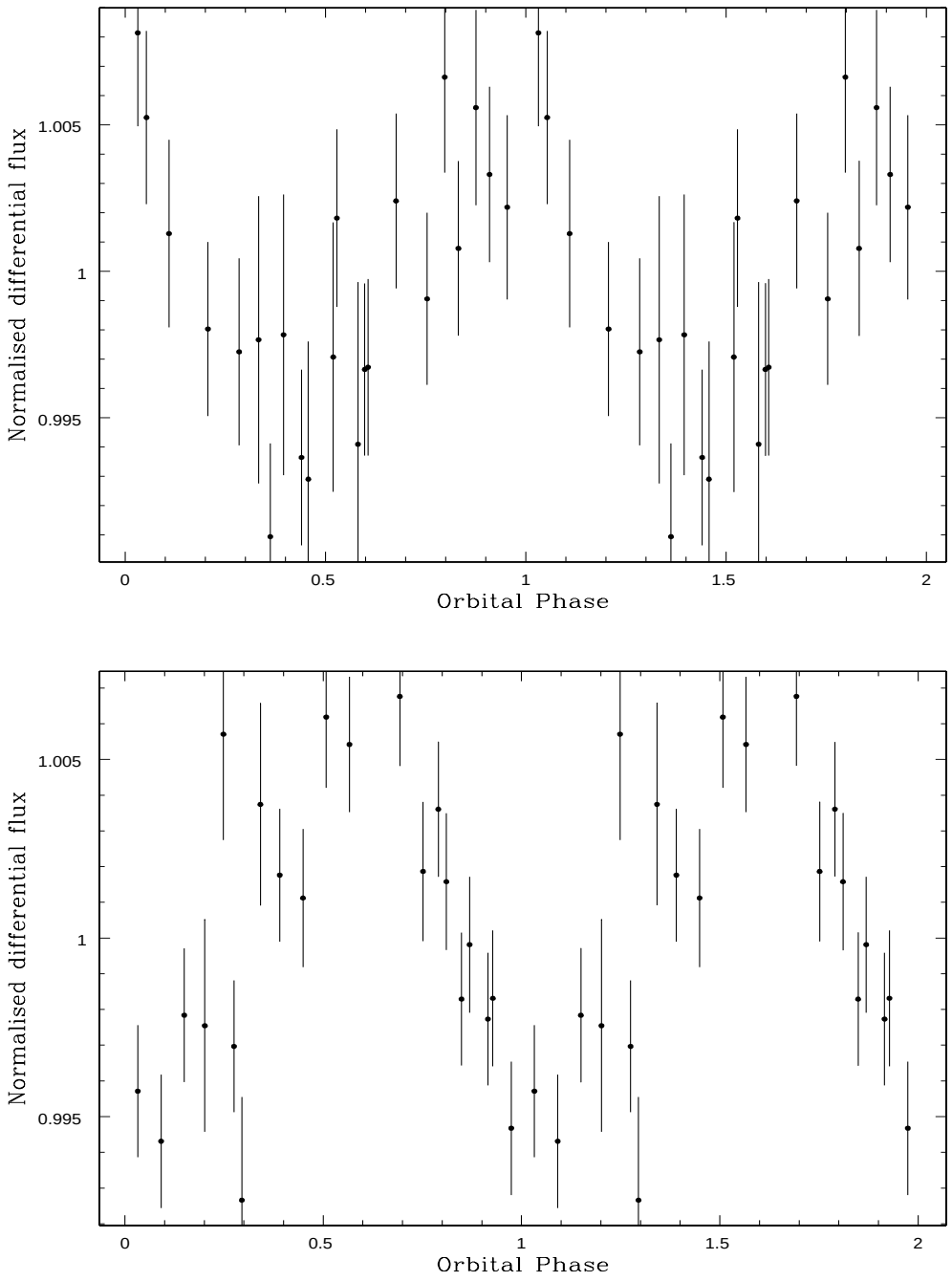

Figure 3.33: Top - folded light curve for G99-37. Bottom - folded light curve for comparison star 2 vs comparison star 3.

3.4.3.3 G141-2

Bergeron et al. (1997) reported that G141-2 may be a double-degenerate system, so we therefore exclude it from our correlation analysis. They also reported that the spectrum is rotationally modulated on a period $\sim$ years. We believe that our brightest comparison star is varying, so we have performed the differential photometry with respect to a combined comparison 2 + comparison 3. We find that a constant fit to the data gives a χ^2 of 212 over 54 dof, formally suggesting variability in this target. The global minimum in the periodogram is at 0.836 cyc/day, with a χ^2 of 54 over 52 dof (Fig. 3.34). However, when we checked for low-level variability in our other comparisons, we found that the RMS of the comparison data was at the same level as the RMS of the target data, ruling out any reliable detection of variability in the target. We also tested the August data alone to check for short-term variability, but found no evidence to support this either. A constant fit to the week gives a χ^2 of 81 over 44 dof, while the minimum in the periodogram has $\chi^2 =$ 33, but again the RMS of the target data is equivalent to that of the comparison stars. We conclude that our data contain no evidence for variability in this system on timescales of less than 10 months, which is consistent with the suggestion by Bergeron et al. (1997) that G141-2 is varying over $\sim$ years, but that the system may be variable at a level lower than that observed in the comparison stars. We have been awarded Liverpool Telescope time over the next 4 semesters to search for long-term variability.

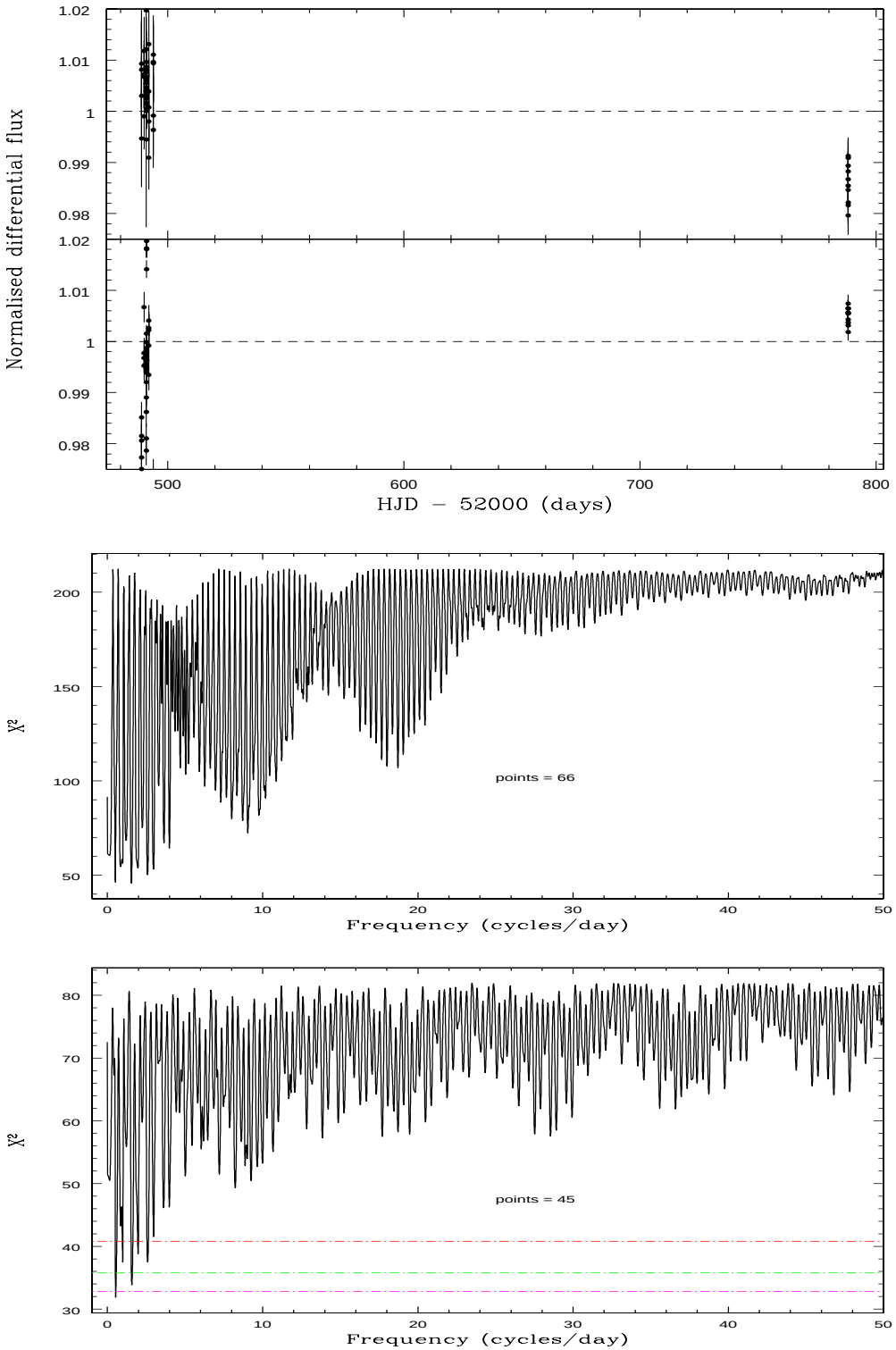

Figure 3.34: Top - Data for target vs comparison stars and comparison 2 vs comparison 3 for G141-2. Middle - periodogram for all the data. Bottom - periodogram for the August 2002 data only. Our data do not support variability on either timescale.

3.4.3.4 G158-45

Putney (1997) reported polarimetric variations in G158-45, suggesting a rotational period of between 11 hours and a few days. We observed the system over 6 nights during the August run, and found tentative evidence for photometric variability in the star on a period of 1.44 hours with a χ^2 of 118 over 78 dof. The light curve folded on this period (Fig. 3.36) looks nice, despite the very low-amplitude of $\sim$1.3%, and a constant fit to the data is significantly worse, with a χ^2 of 148 over 81 dof. It should be noted that G158-45 is at the faint end of our sample (15.9 mag) and so the errors on the data points are relatively high. Observations using a bigger telescope would be useful in determining the true level of variability in this star.

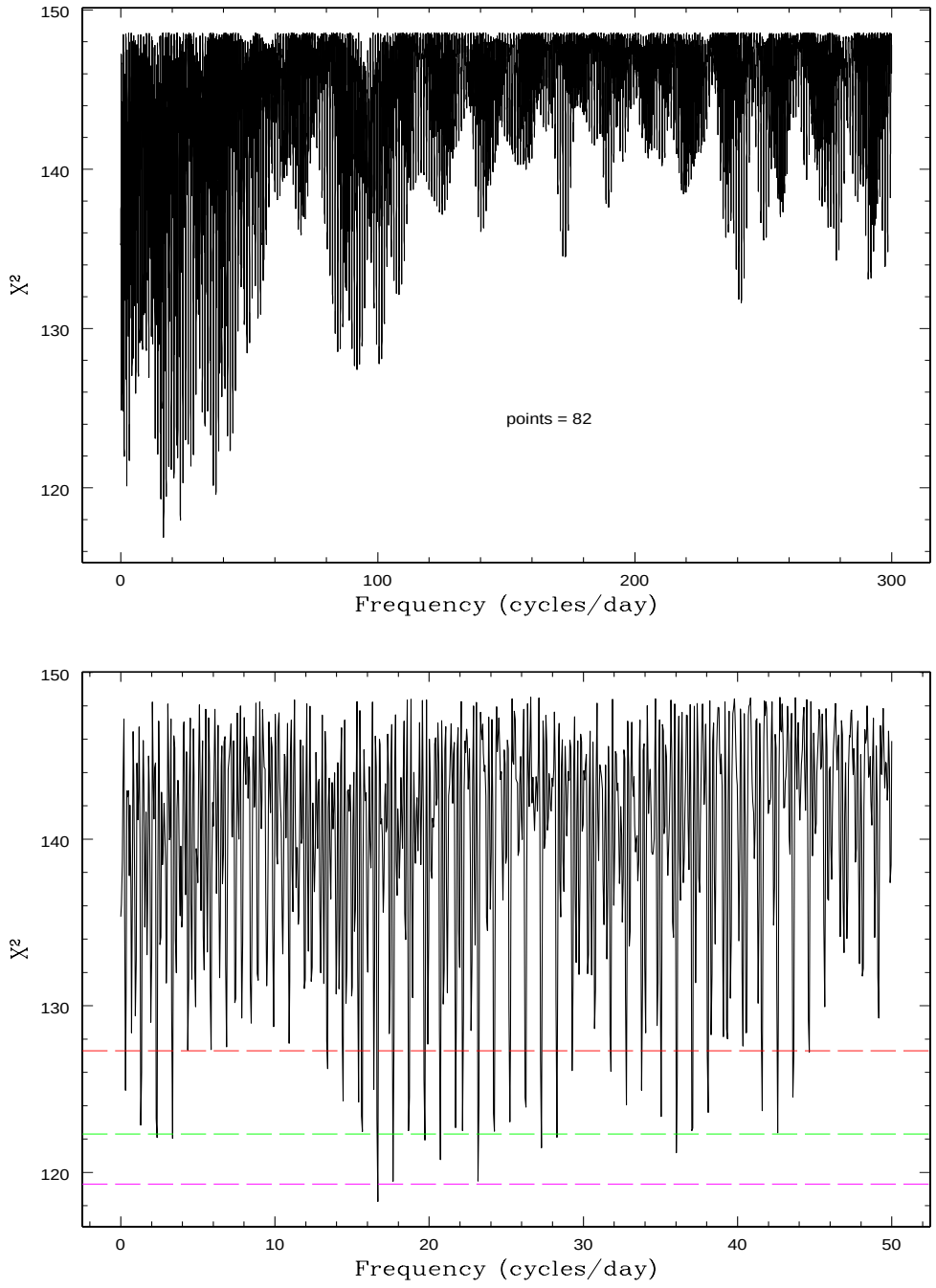

Figure 3.35: Top - periodogram for G158-45. Bottom - periodogram zoomed in on the global χ^2 minimum.

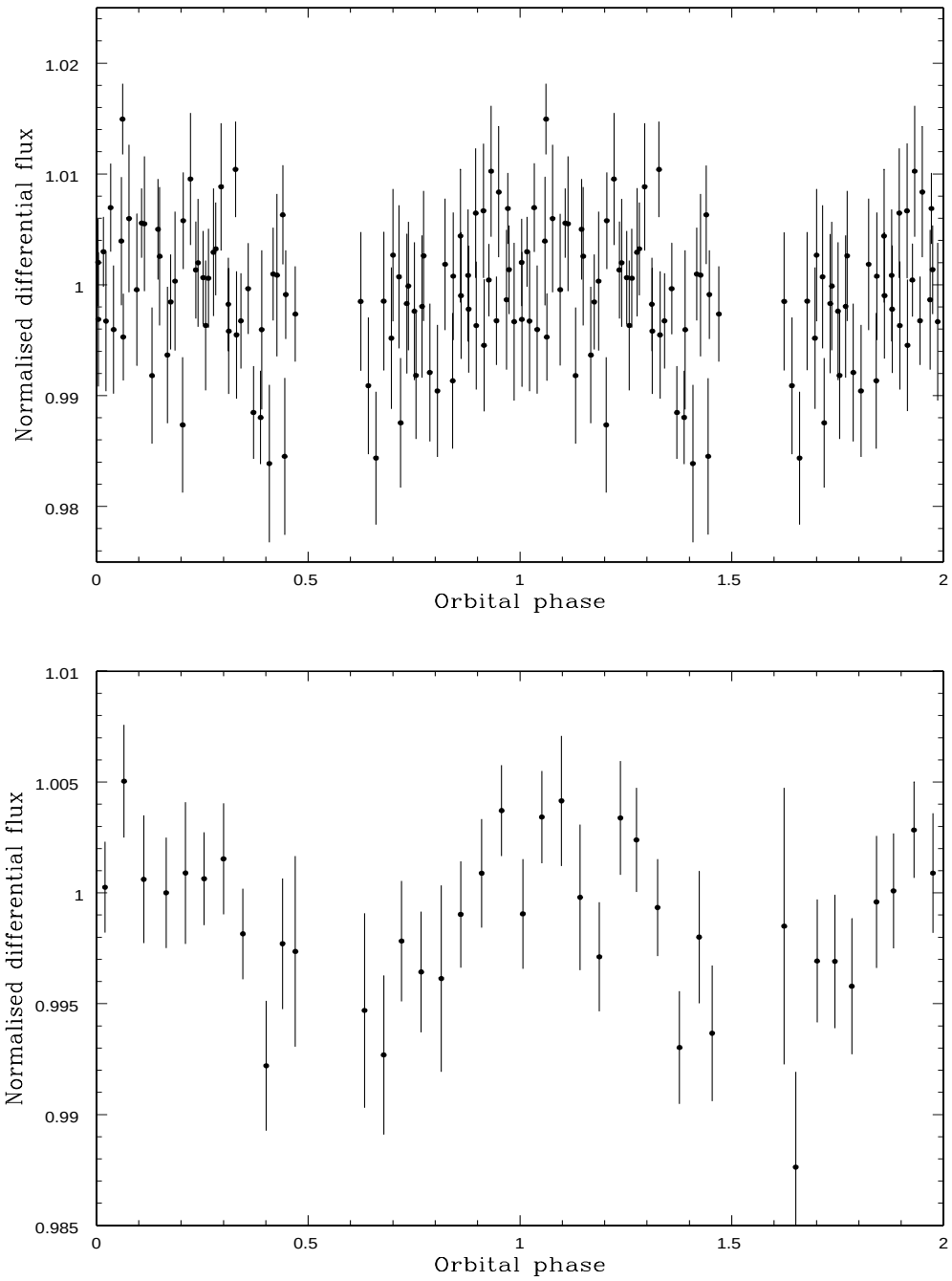

Figure 3.36: Top - light curve for G158-45, folded on the best period of 1.44 hours. Bottom - folded light curve binned by a factor of 4.

3.4.3.5 G227-35

Cohen et al. (1993) pointed out a lack of variability in the polarisation of G227-35 over 2 nights, and 5, 13 and 18 year intervals, concluding that this is either a very slow rotator, or the magnetic and rotation axes are nearly aligned and the field is rotationally symmetric. Unfortunately we were unable to test this star for variability as our comparison stars were varying with respect to each other at a greater level than any variability in the target (see Fig. 3.37). This target will need to be re-observed with different comparisons in the field of view.

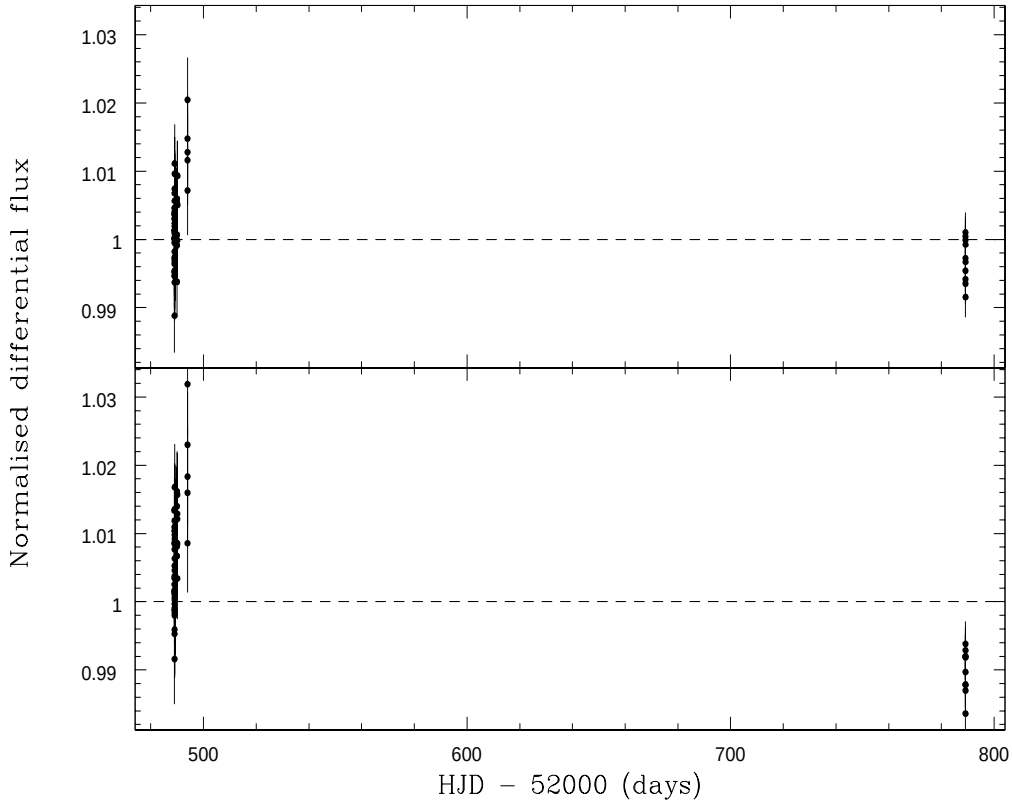

Figure 3.37: Data for G227-35. Top - target vs comparison stars. Bottom - comparison 2 vs comparison 3.

3.4.3.6 G256-7

We have found no evidence for variability in this object. A constant fit has $\chi^2 = 44$ over 35 dof, while the periodogram shows a global minimum at a frequency of 4.84 cyc/day, with $\chi^2 = 26$ over 33 dof (Fig. 3.38. While this would formally suggest that G256-7 is variable, the RMS of the comparison data is greater than the RMS of the target (Fig. 3.39), so we conclude that we have found no evidence for variability in this target, but it may exist below the level of variability in the comparisons.

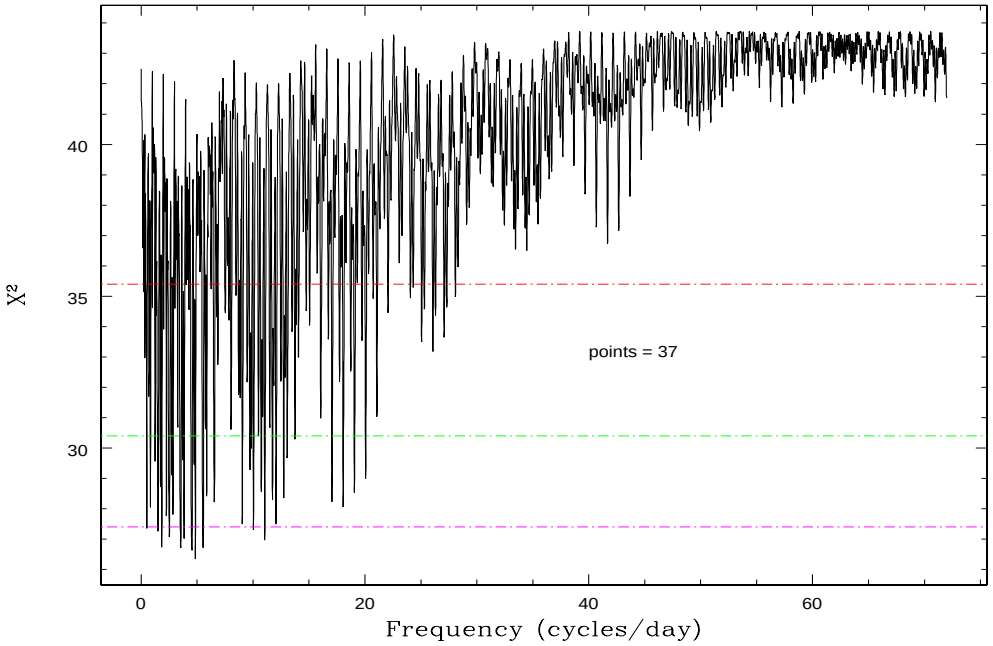

Figure 3.38: Periodogram for G256-7.

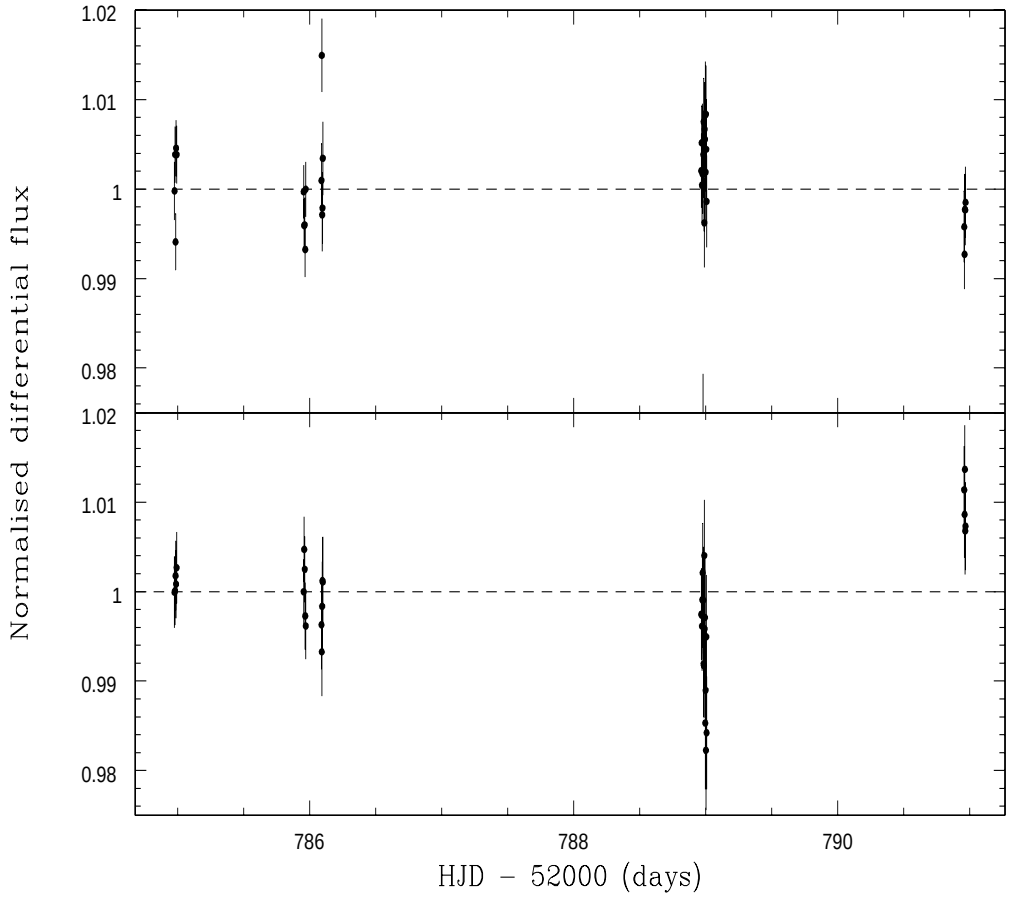

Figure 3.39: Target data vs comparison data for G256-7 (top) and comparison 2 vs comparison 3 (bottom).

3.4.3.7 GD90

We only took 16 useful observations of GD90, all during the February 2003 run, and we find no conclusive evidence for variability over the week. The periodogram shows that the 3σ error in the best frequency (P = 7.7 minutes) covers almost all of the plotted frequency range (Fig. 3.40). A constant fit gives a χ^2 fit of 23 over 16 dof, while the best-fitting frequency in the periodogram of 187.7 cyc/day has a χ^2 of 8 over 13 dof. When scaled this gives a $\Delta\chi^2 = 23$, putting it above our level of significance for a detection of variability. We conclude that our sparse data formally shows evidence of variability, but that more data are needed to verify this, especially considering the poor observing conditions on the first and last nights.

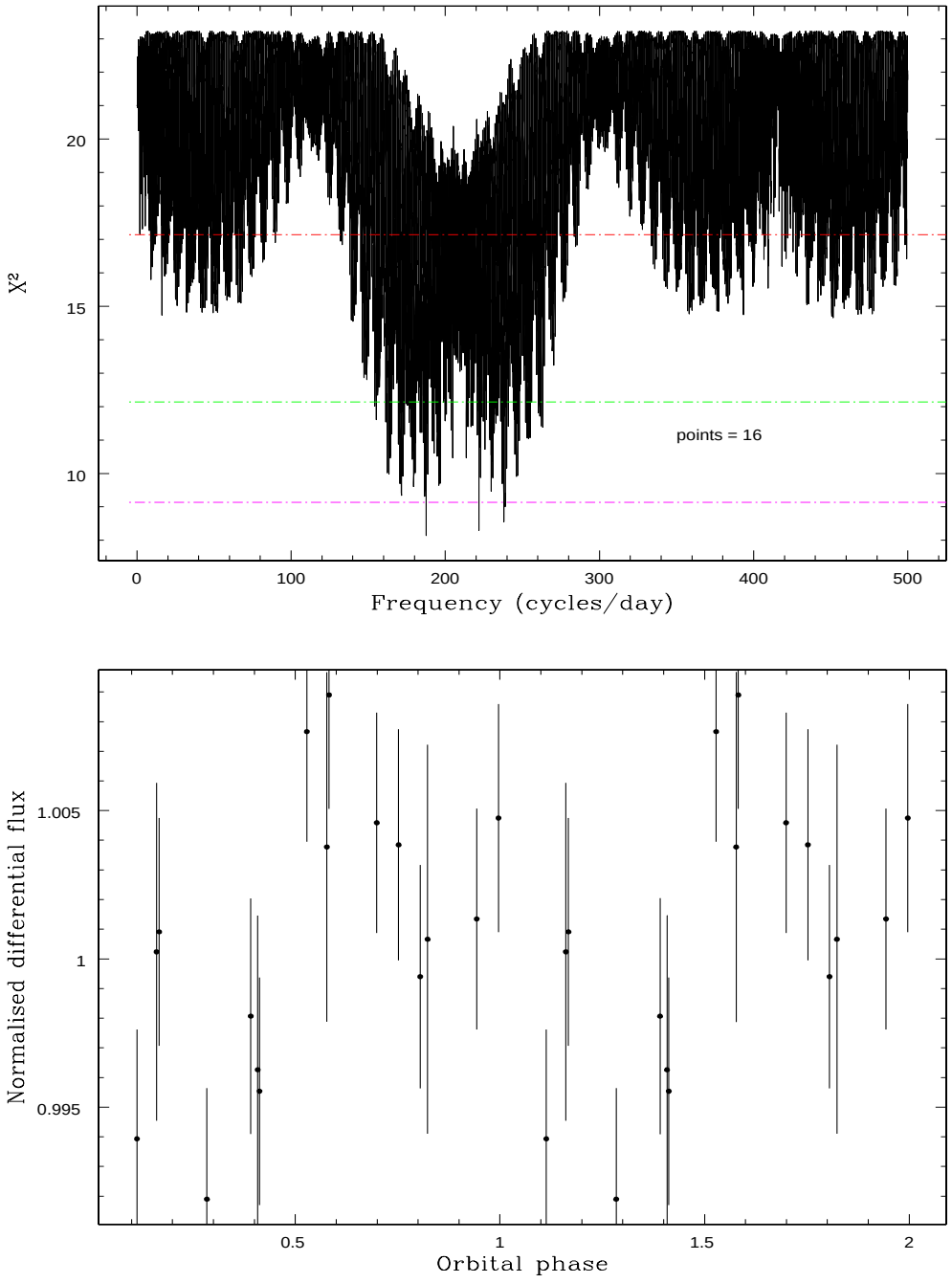

Figure 3.40: Periodogram and folded light curve for GD90, with a best period of 7.7 minutes.

3.4.3.8 GD229

Differences in the spectrum of the star in the decade between the studies by Green & Liebert (1981) and Schmidt et al. (1990) were assumed by the latter group to be due to rotation of the WD during that time. Observations taken over two years by Schmidt et al. (1996) showed no such variability, suggesting that the rotation period is of order decades. This was confirmed by a review of all polarimetry of GD229 by Berdyugin & Pirola (1999) who concluded that the star is definitely variable over about 10 years, with a probable modulation period of 80-100 years. We find no reliable evidence for variability over a year or shorter timescales. The χ^2 of a constant fit is surprisingly high, at 263 over 64 dof, but the RMS of the target flux is on the same level as the RMS of the comparison flux, so this may be entirely due to variations in the comparison flux and any result from the periodogram will be unreliable (Fig. 3.41). The light curve folded on the best-fitting period of 10.7 hours (Fig. 3.42) shows that the sinusoidal fit is reliant upon changes in flux from night-to-night rather than during each set of observations.

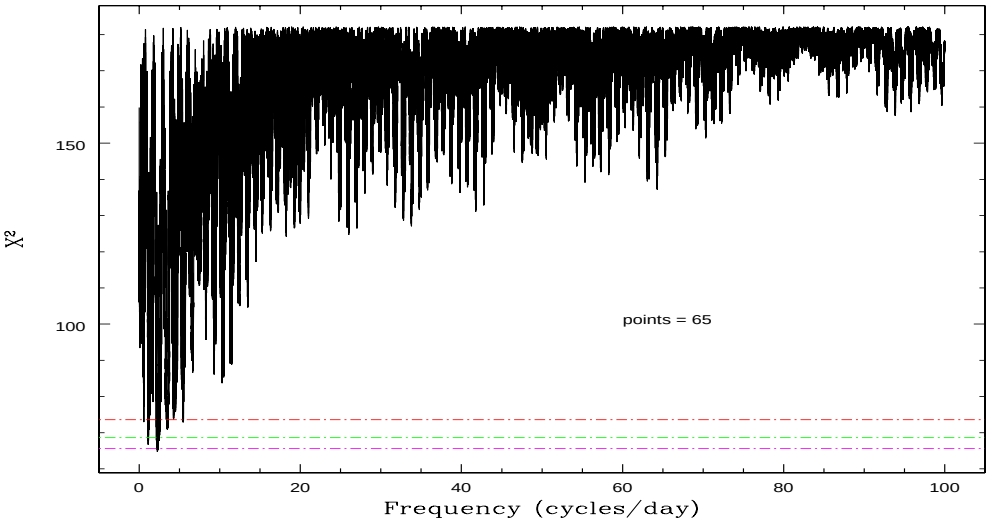

Figure 3.41: Periodogram for GD229.

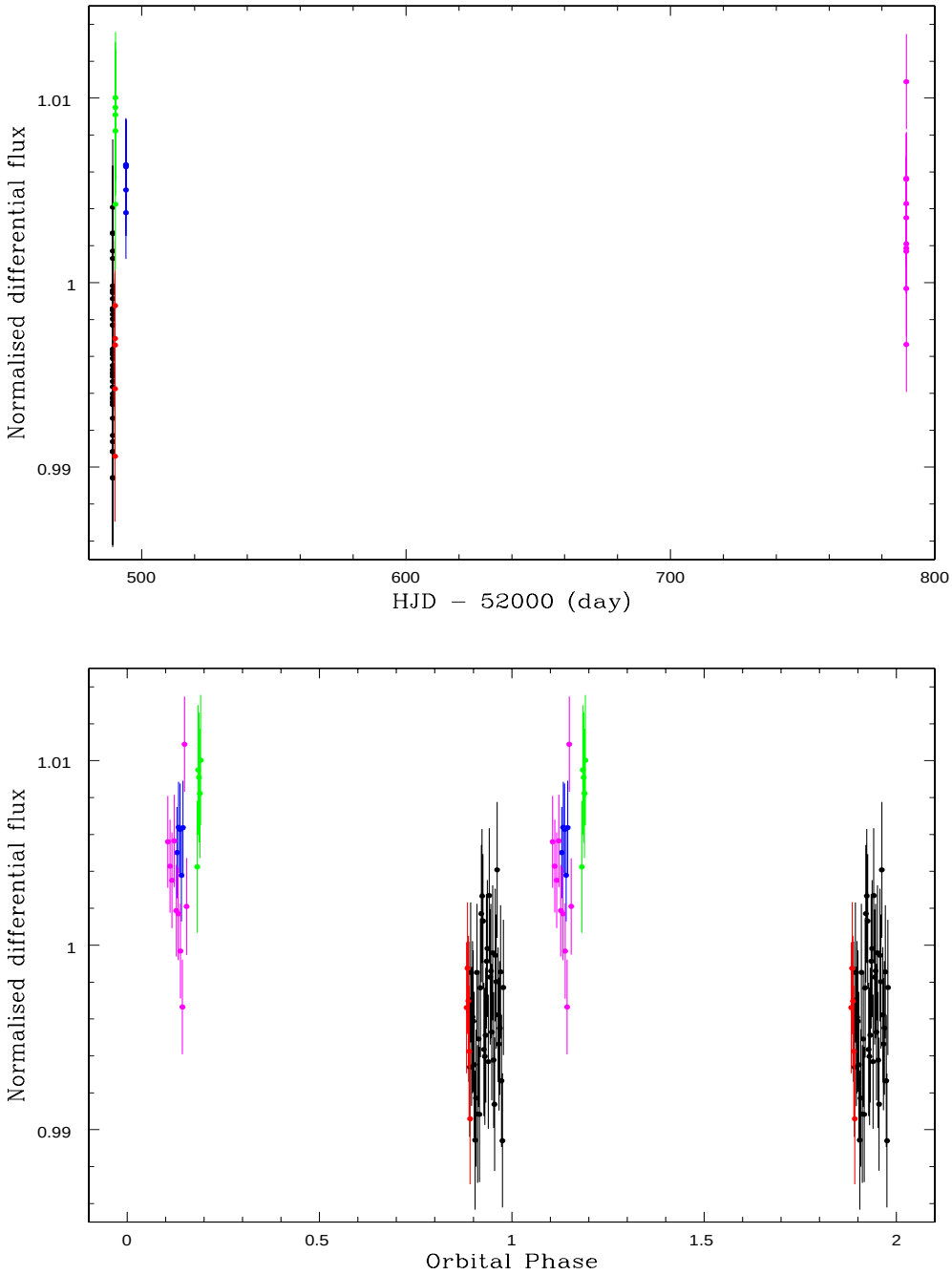

Figure 3.42: Data and folded light curve for GD229. Different nights of data are plotted in different colours. Lower light curve is folded on the best period of 10.7 hours.

3.4.3.9 Grw +70°8247

The polarisation curves for this star have remained unchanged over 25 years of observations, suggesting that this star is a very slow rotator, with a period of ≥ 100 years. We took data over the week of the August 2002 run, plus one set during May 2003 to check for any long-term variations over the year. A constant fit to the data has a χ^2 of 472 over 148 dof, while the best-fit period from the periodogram at 0.248 cyc/day has $\chi^2 = 318$ over 146 dof. This very low frequency points to a long-term trend rather than a short-term period. The RMS of the target flux is smaller than the RMS of the comparisons, which would explain both the poor constant fit and the poor fit of the best period (Fig. 3.43). We have not found any reliable evidence for variability or periodicity in the target, but note that the periodogram (Fig. 3.44) points to long-term trends that may be picked up by our observing programme with the Liverpool Telescope.

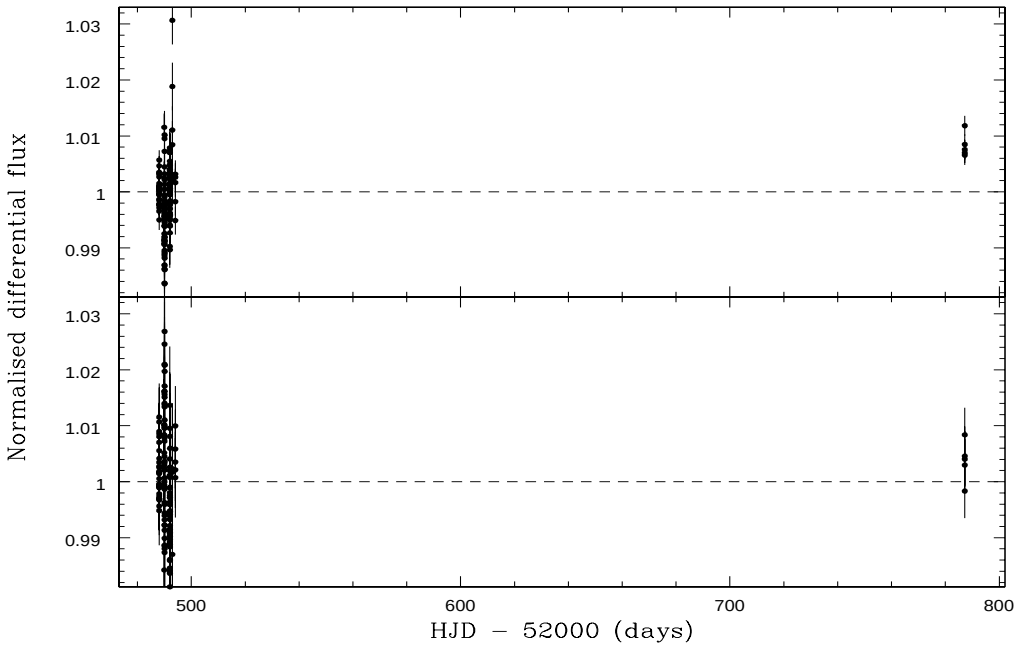

Figure 3.43: Data for Grw +70°8247. Target vs comparisons (top) and comparisons vs each other (bottom)

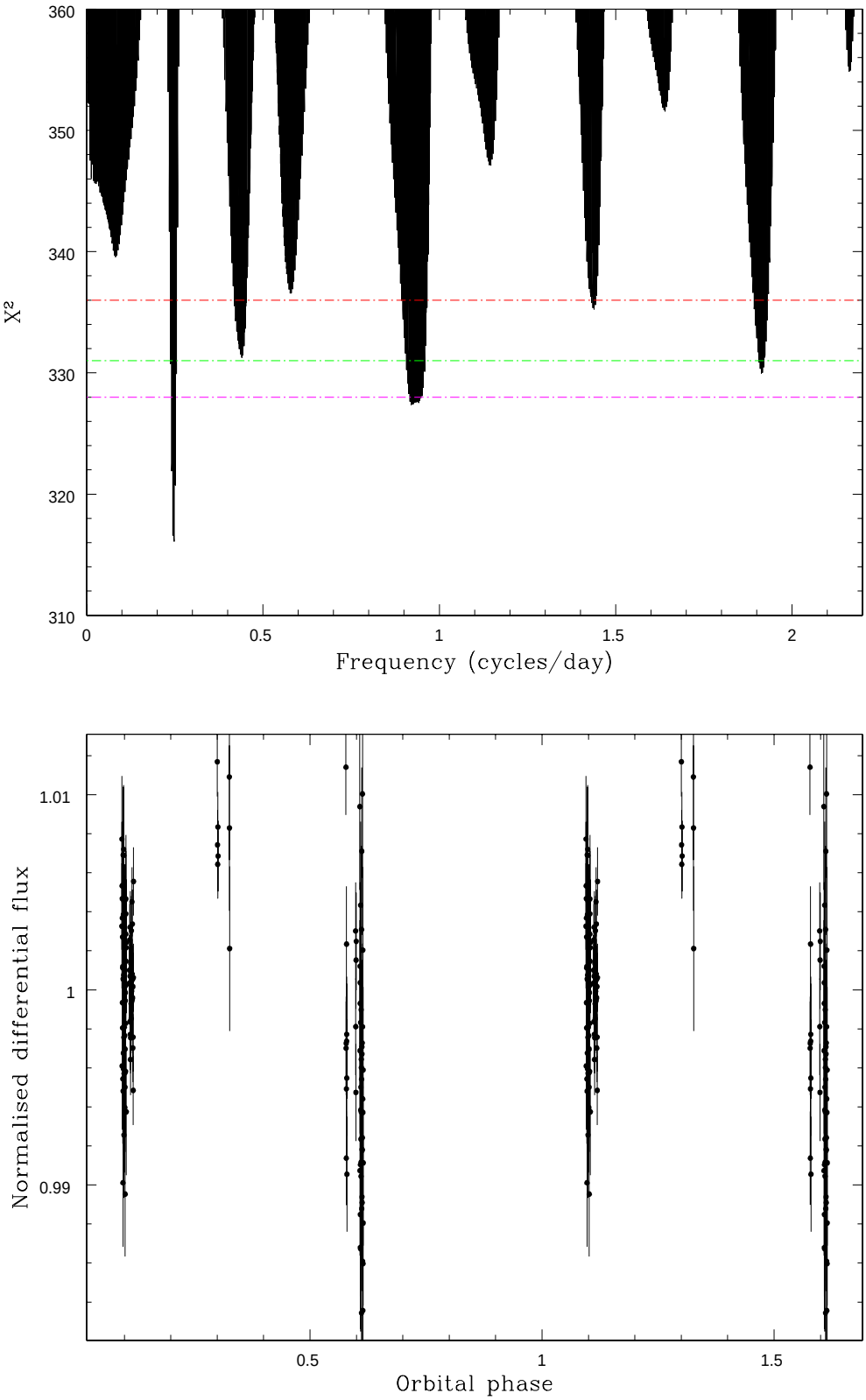

Figure 3.44: Periodogram and folded light curve for Grw +70°8247. Light curve is folded on the best period of 4.03 days.

3.4.3.10 HE0107-0158

The magnetic field of HE0107-0158 was discovered by Reimers et al. (1998), but their discovery was based on a single low-resolution spectrum. Schmidt et al. (2001) believe that this system is a non-magnetic WD-cool dwarf pair, and on the basis of this we exclude it from the correlation analysis of this survey. The evidence for variability in this system is tenuous. The periodogram (Fig. 3.45) contains no clear best-fit period within the 2σ errors, although we note that the minimum scaled χ^2 value at a frequency of 6.813 cyc/day is $\Delta\chi^2 = 18$ lower than that for a constant fit. The data and the light curve folded on the best period are shown in Fig. 3.46. While it is possible that the source may be varying, we have certainly not been able to determine its period. This target would benefit from higher signal-to-noise observations on a bigger telescope.

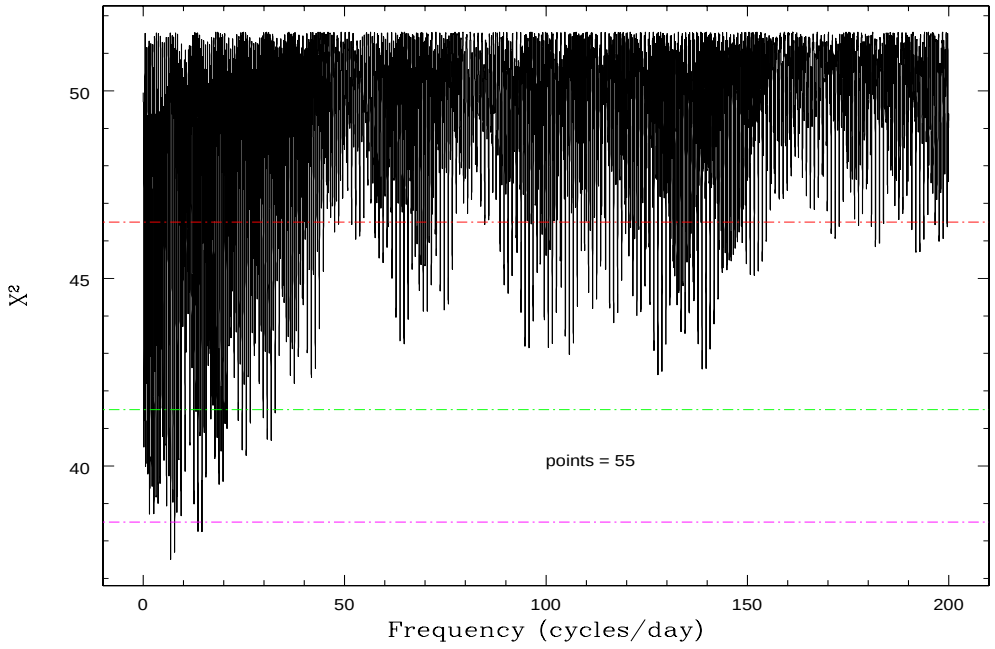

Figure 3.45: The periodogram for HE0107-0158, showing no significant minima with respect to the other periods

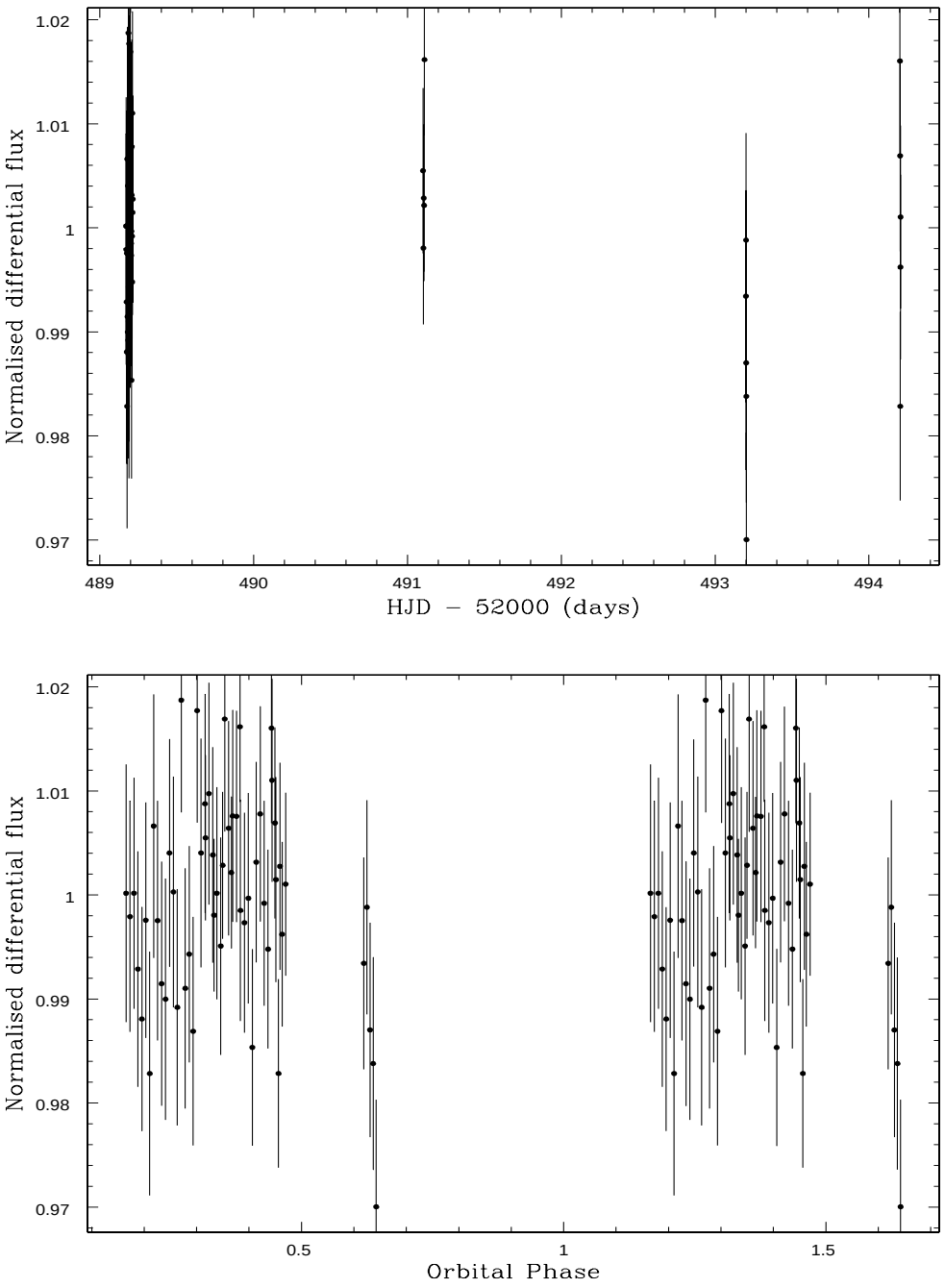

Figure 3.46: Top - the data for HE0107-0158. Bottom - light curve folded on the best period of 3.5 hours.

3.4.3.11 HE1045-0908

Schmidt et al. (2001) report variability in their spectroscopy of HE1045-0908, and suggest a rotational period for the star of between 2 – 4 hours. The target is among the faintest in our survey (only 16.8 mag), and our data have poor signal-to-noise and considerable scatter, but we find no evidence for variability on the timescale from the literature. We find that the χ^2 for a constant fit is 42 over 40 dof and the global minimum in the periodogram is not much better at 29 over 37 dof (Fig. 3.47). When scaled, however, $\Delta\chi^2 = 17$, indicating that formally this target is variable. The best period from the periodogram is 14.3 hours, although when folding on this period, the data from the separate nights is clustered into two separate blocks, suggesting that this may just be a night-to-night systematic effect rather than real variability (Fig. 3.48).

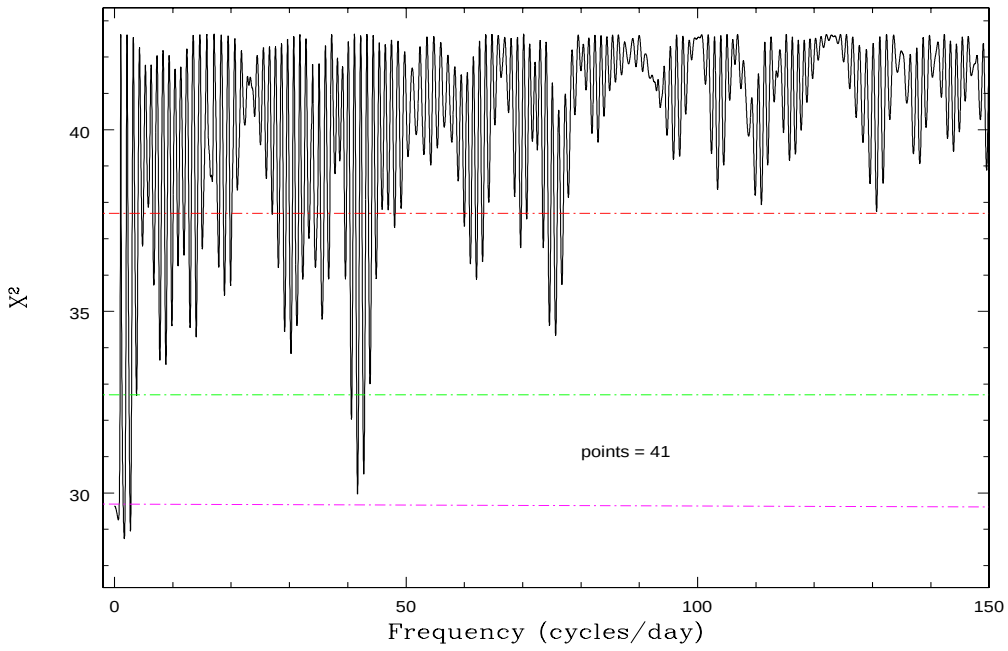

Figure 3.47: Periodogram for HE1045-0908

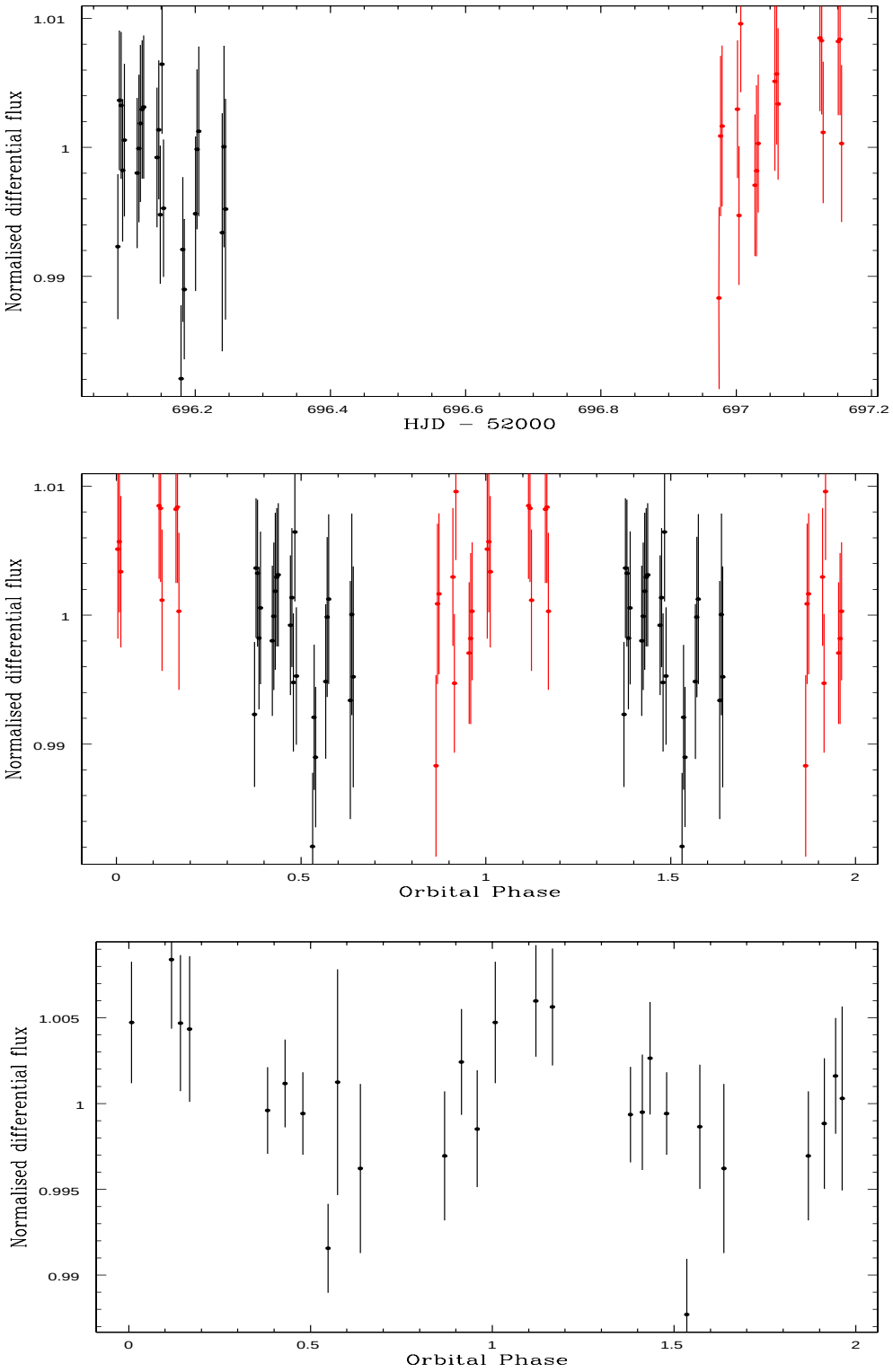

Figure 3.48: Top - data for HE1045-0908 with separate nights plotted in different colours. Middle - light curve folded on the best period of 14.3 hours. Bottom - folded light curve binned by a factor of 4.

3.4.3.12 LB11146

LB11146 is a double-degenerate binary system, and is therefore excluded from our correlation analysis. We find no evidence for variability in this system, although this is based on only 16 data points. A constant fit gives a χ^2 of 12, while the global minimum in the periodogram has a χ^2 of 3.4, but no significant minima (Fig 3.49). Moreover, we find that the RMS of the target flux is lower than the RMS for the comparison stars flux, so any sinusoidal fit will not be reliable.

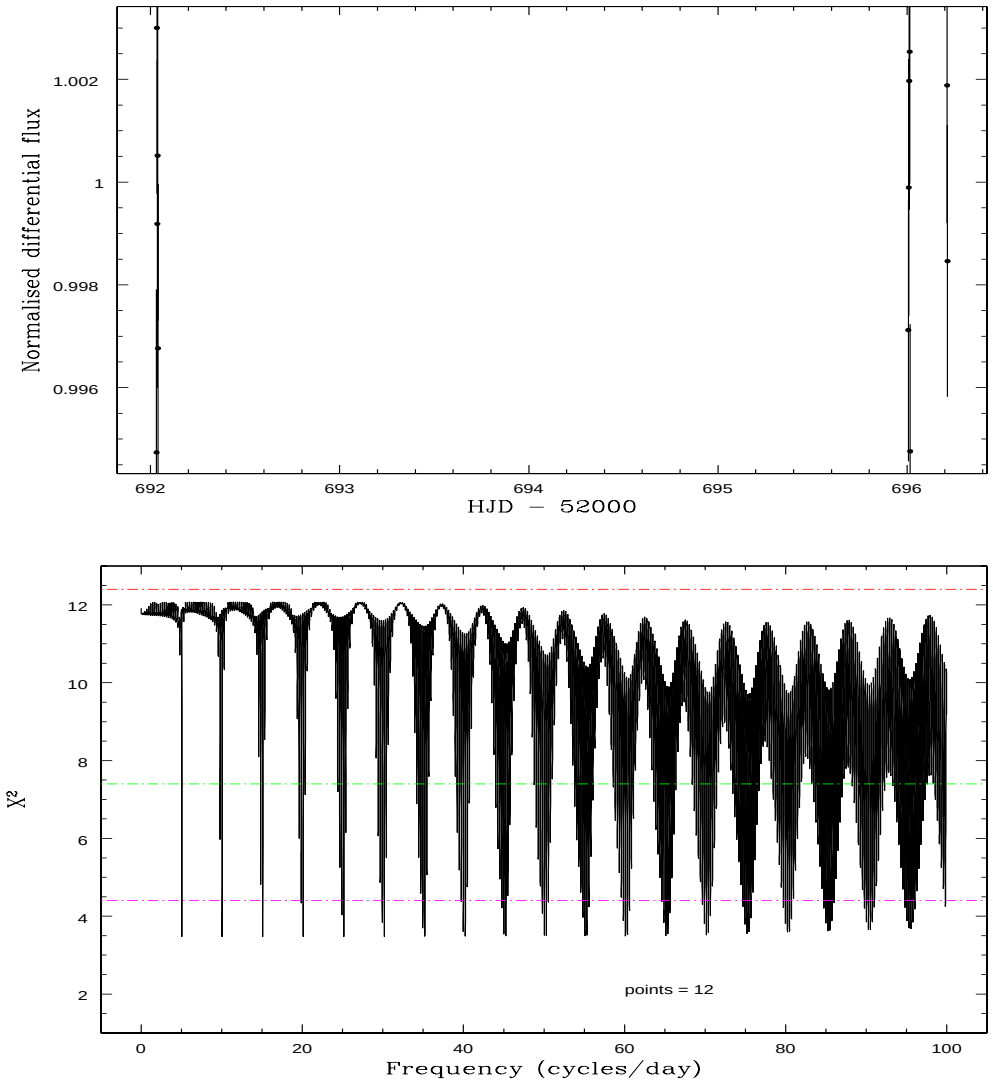

Figure 3.49: Data and periodogram for LB11146

3.4.3.13 PG0136+251

We find tentative evidence for variability in this object. The periodogram shows a global χ^2 minimum of 39 over 57 dof at a frequency of 53.9 cyc/day (P = 26.7 mins) and when scaled, the $\Delta\chi^2 = 17$, just above our limit for variability. However, the periodogram also shows a heavy aliasing structure and the 3σ error covers most frequencies (Fig. 3.50). The folded light curve is shown in Fig. 3.51. We conclude that we may have found low-amplitude variability in this object with a period of 27 mins.

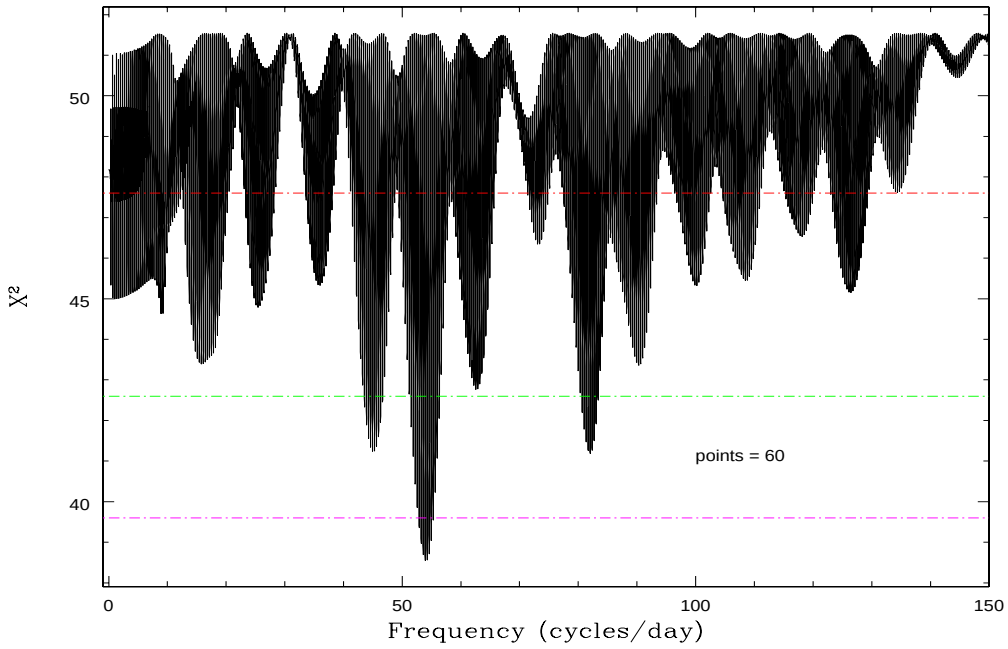

Figure 3.50: Periodogram for PG0136+251.

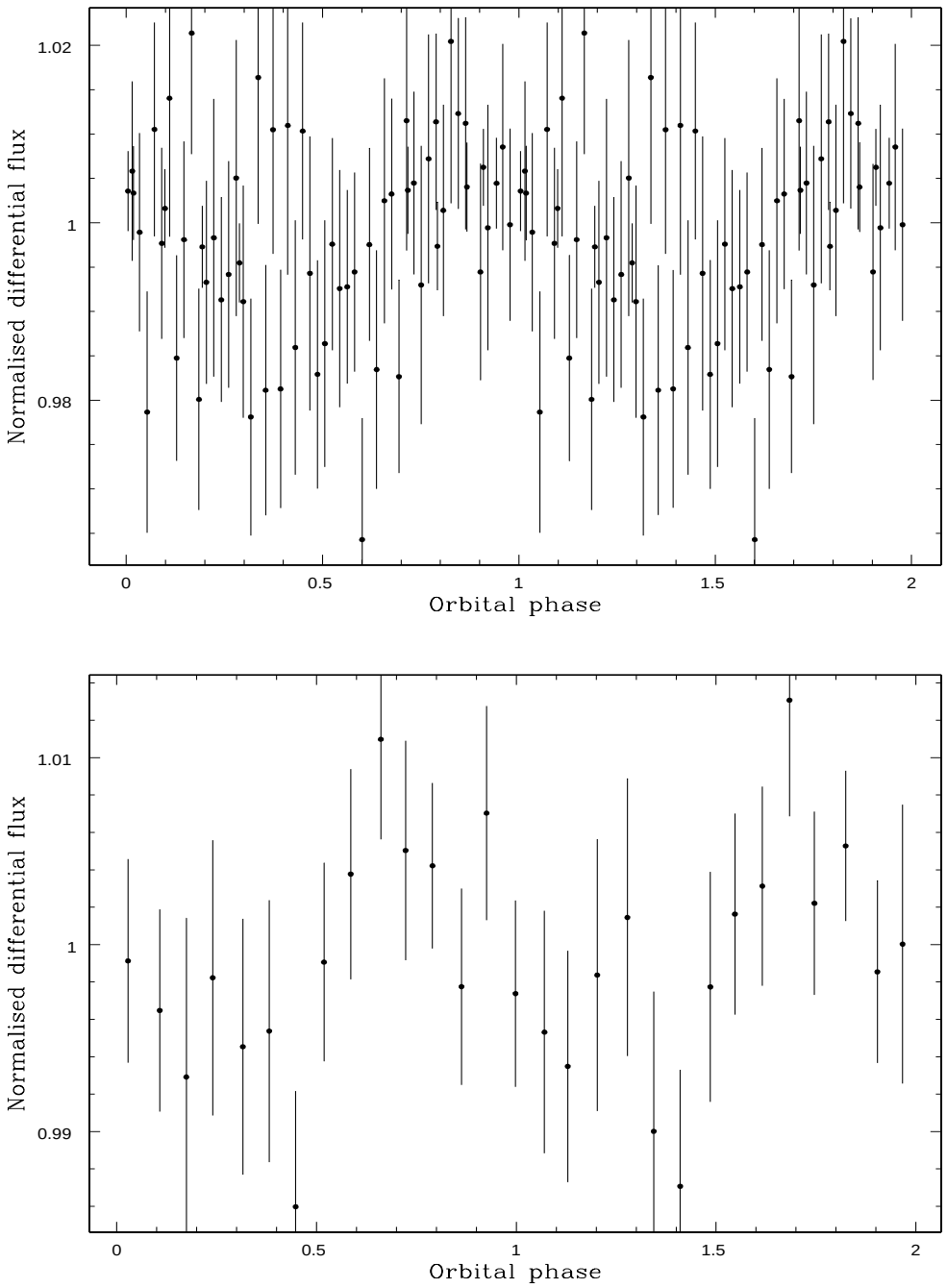

Figure 3.51: Periodogram and folded light curve for PG0136+251. Light curve is folded on a period of 26.7 mins.

3.4.3.14 PG1220+234

We find no evidence for variability in this object over timescales of a week. There are no significant minima in the periodogram and a difference in χ^2 of $\sim$12 covers all frequencies. A constant fit has a χ^2 of 17 over 16 dof. We note that while we have not found any evidence for variability in PG1220+234, we only have 17 poorly-spaced data points over a week and so we cannot rule it out on any timescale.

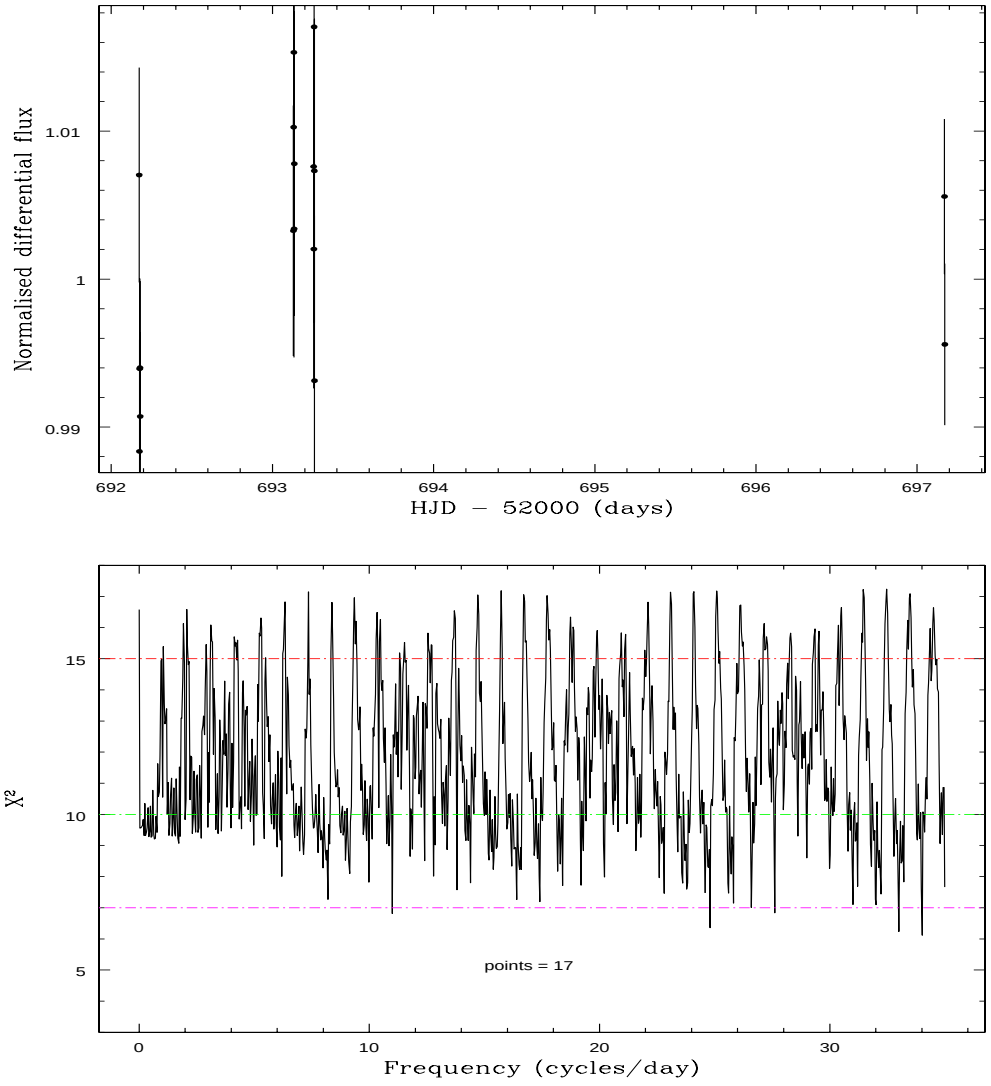

Figure 3.52: Periodogram for PG1220+234, without any significant minima.

3.4.3.15 SBSS1349+545

We have no conclusive evidence for variability in this object, since the RMS of the data is only just above the RMS of the comparison stars. The χ^2 of a constant fit through the data (71 over 48 dof) is significantly worse than the minimum χ^2 in the periodogram of 42 over 46 dof (Fig. 3.53), but the 2σ errors cover a range of periods. The light curve folded on the best period of P = 5.84 hours is shown in Fig. 3.54. We must conclude that if this object is varying, the level of variability in our comparison stars may have affected the location of the global χ^2 minimum in the periodogram, so our best-fitting period is not reliable.

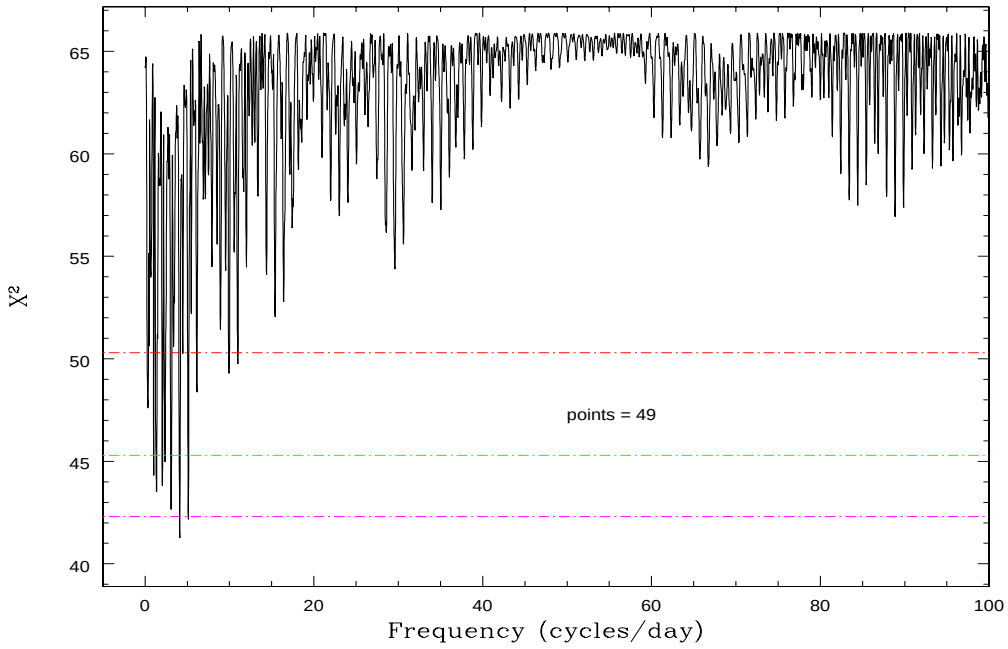

Figure 3.53: Periodogram for SBSS1349+545.

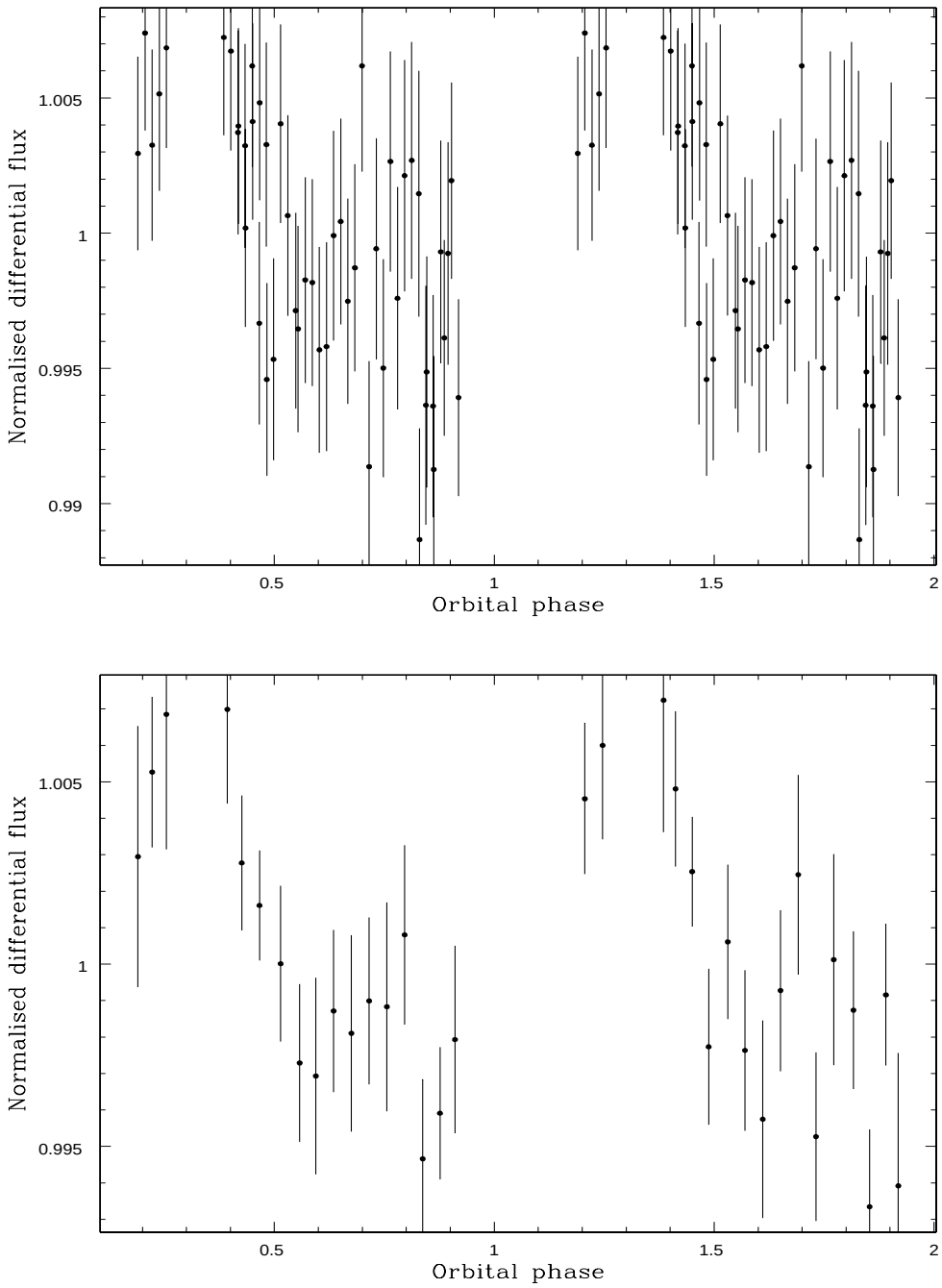

Figure 3.54: Lights curves for SBSS1349+543 folded on the best-fitting period of P = 5.84 hours. Lower plot is binned by a factor of 3.

3.4.4 Targets that are not seen to vary

3.4.4.1 G183-35

Putney (1997) reported possible rotation of this object with a period between 50 minutes and a few years. From our photometric data, taken over a week in Aug 2002 and a further week in May 2003, we find no evidence of rotation on timescales of less than a year. A constant fit to the data gives a χ^2 of 122 over 152 dof, compared to a χ^2 minimum in the periodogram of 101 over 149 dof (Fig. 3.55). We folded the light curve on the best-fitting frequency of 2.67 cyc/day, but this appears to be flat over the year (Fig. 3.56). We conclude that G183-35 is not varying on timescales of less than a year, and have been awarded Liverpool Telescope time to follow up this object on longer timescales.

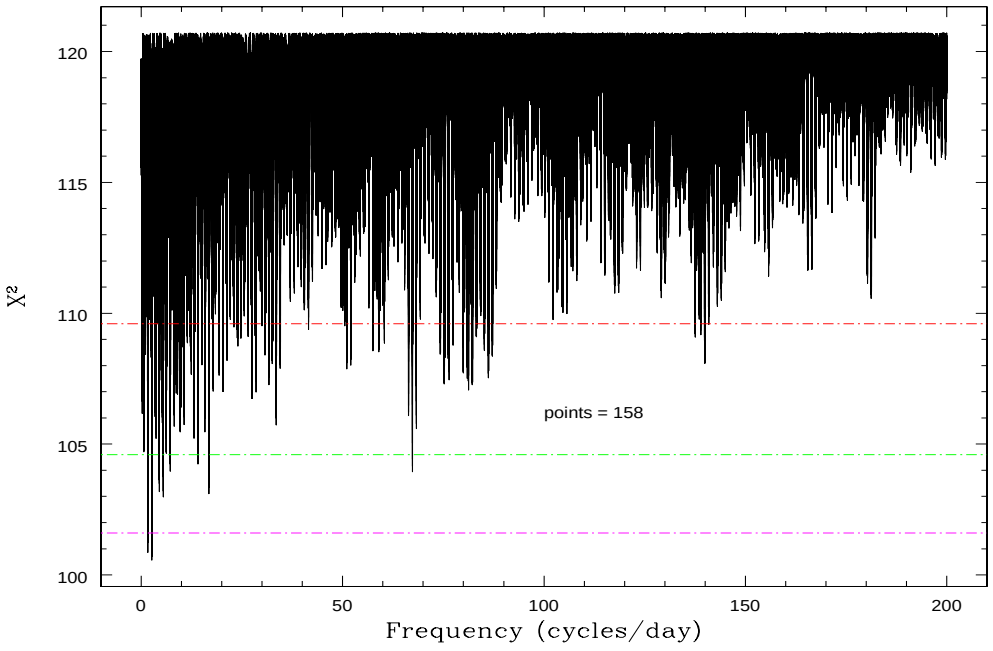

Figure 3.55: Periodogram for G183-35.

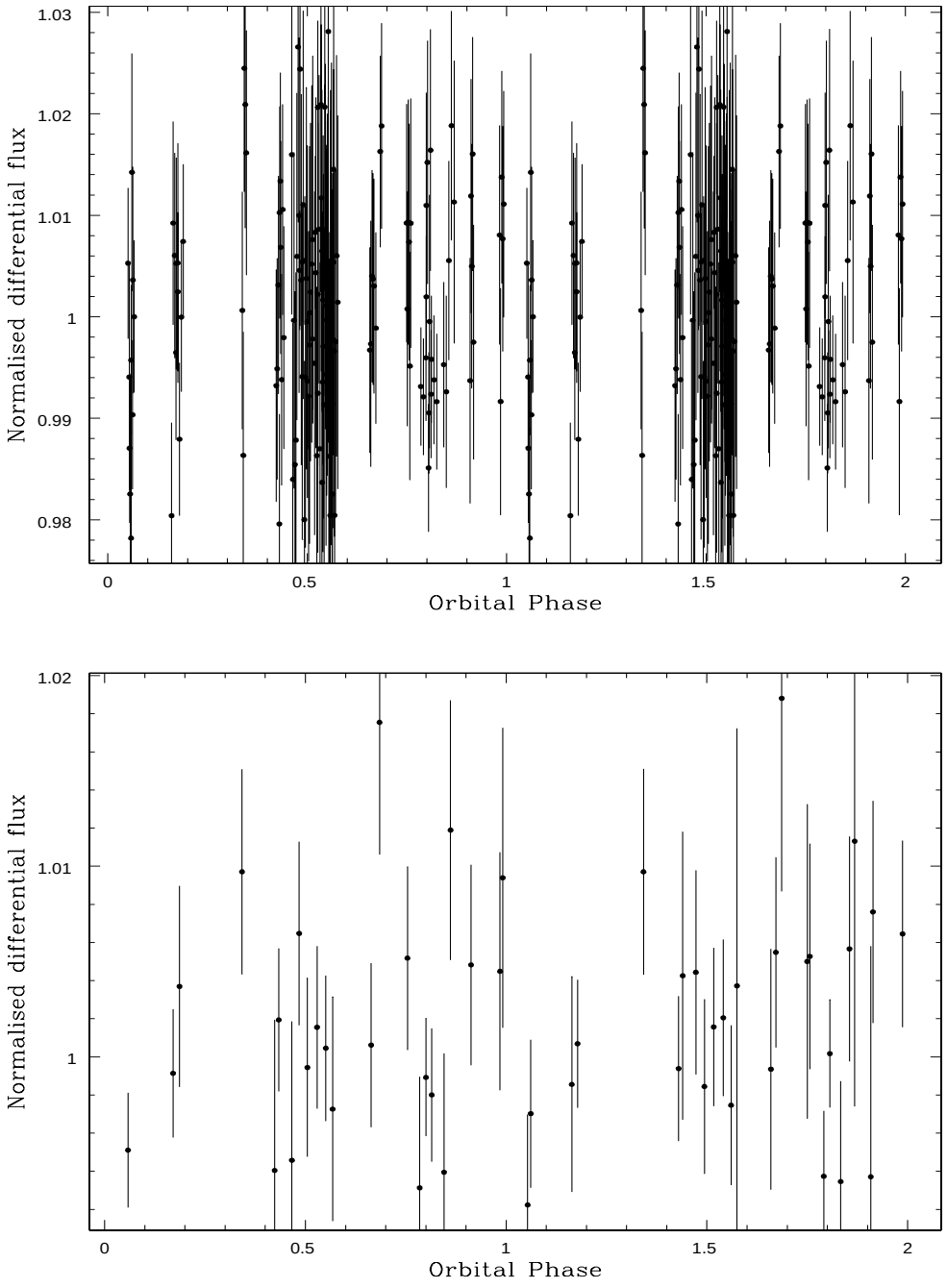

Figure 3.56: Folded light curve for G183-35 with all the data points (top) and binned by a factor of 3 (bottom). Light curve is folded on a period of 8.99 hours

3.4.4.2 GD77

GD77 was observed over 5 nights during the February run. We find no evidence for variability in our data. The periodogram shows two minima at 0.335 and 1.339 cycles/day (Fig. 3.57), but the 3σ errors on these encompass most of the periodogram. The folded light curves show that the data points are clustered into nightly observations, making it more likely that the periodicity is based on night-to-night systematic effects rather than an intrinsic variability in the target (Fig. 3.58). The minimum χ^2 from the periodogram is 54 over 41 dof, while a constant fit gives a χ^2 of 72 over 44 dof. Scaling these to give a reduced $\chi^2 = 1$ in the periodogram gives a $\Delta\chi^2 = 14$ between the sinusoidal and constant fits, below our significance threshold. We conclude that there is no evidence for variability in GD77.

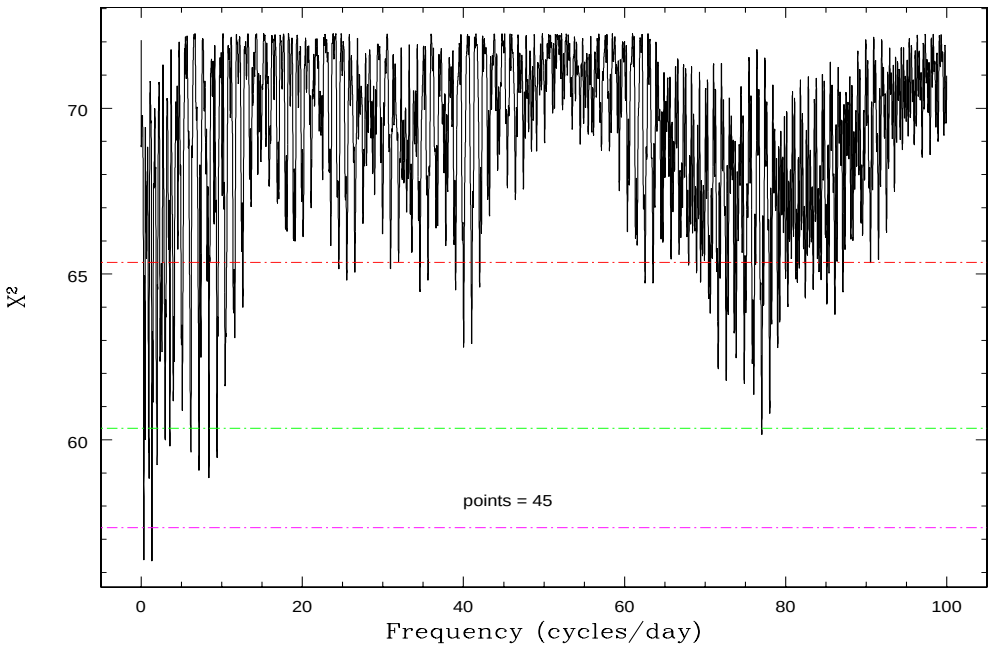

Figure 3.57: Periodogram for GD77.

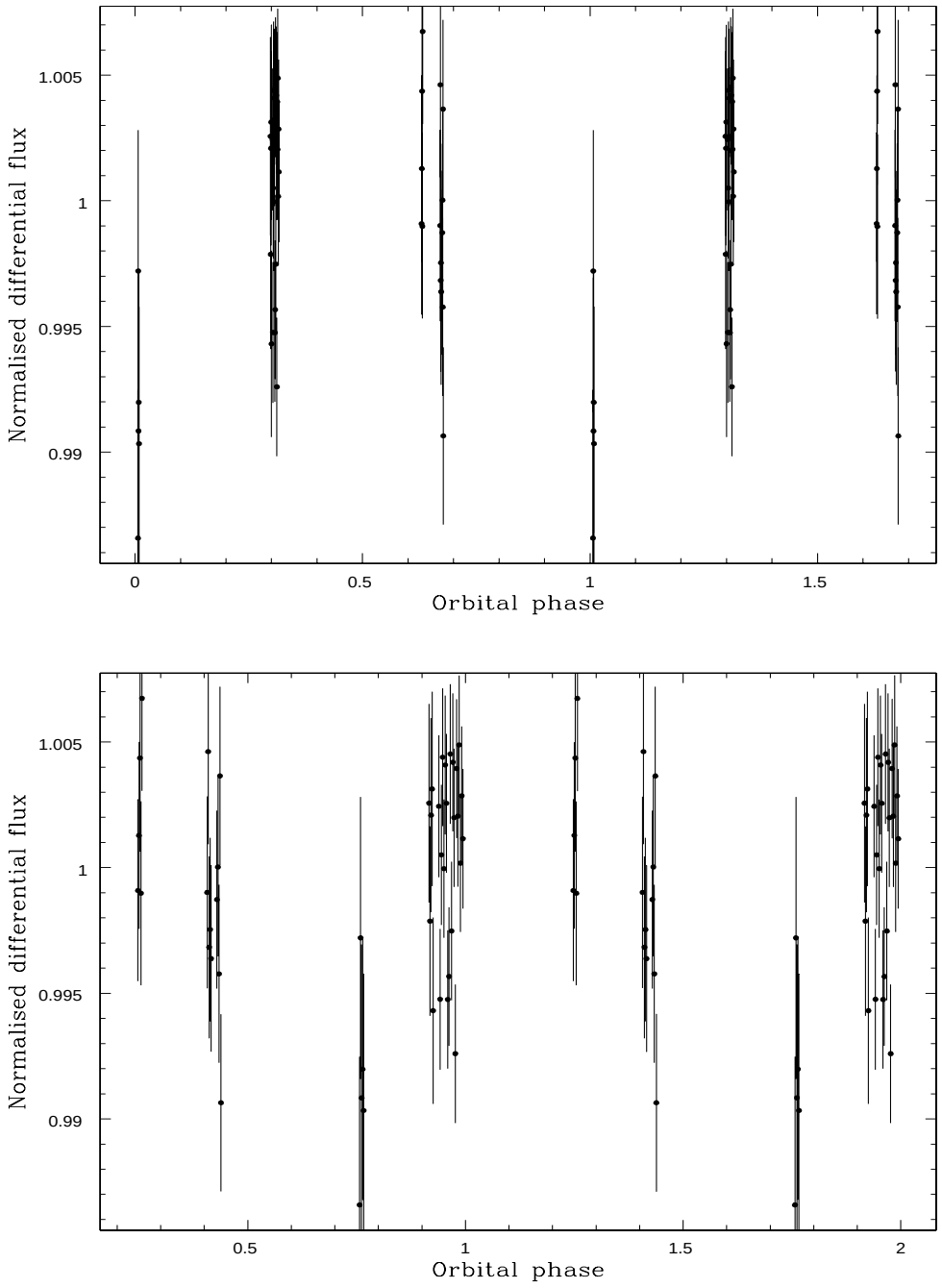

Figure 3.58: Light curves for GD77 folded on the two best periods of 2.98 days (top) and 17.9 hours (bottom).

3.5 Discussion

Of our 34 successfully observed targets, 4 are believed to be binary systems (HE0107-0158, G195-19, EUVE J1439+75.0 and G141-2), and are therefore excluded from any further analysis. Of the remaining 30 magnetic white dwarfs, we have found that five (17%) are variable with reliably derived periods, 12 (40%) are variable but we were unable to determine an exact period, and a further 11 (36%) may or may be not variable. We were able to rule out variability over our observed timescale in 2 objects (7%). 1 of these was observed over the full baseline of 10 months and is therefore either a long-period rotator, variable at a very low level, or its magnetic fields is rotationally symmetric and aligned with the spin axis. We have been awarded Liverpool Telescope time over the next 4 semesters to follow up those sources we believe to be rotating on timescales $>$ month. The updated period distribution for magnetic white dwarfs can be found in Fig 3.59. While this appears to be bimodal, this is partly an artificial effect, as magnetic white dwarfs have not been observed for variability on timescales of months, and the longer-period variables have been grouped into a single class with an estimated period of 5 years. The distribution at low periods is real. We expect the peak between $4 < \log(\mathrm{P}) < 5$ to be smoothed out as we determine exact periods from the Liverpool Telescope data.

One of the flaws in our method for detecting the periods is the sensitivity of the periodograms to the amplitude of the variability. The greater the amplitude, the more likely the minimum χ^2 in the periodogram at that frequency will be a significantly better fit than other periods, so we should be heavily biased towards determining periods for the highly variable sources compared to those varying on lower levels. A plot of the distribution of amplitudes of the variability in our sources is shown in Fig. 3.60 and shows that we have been successful in detecting variability

Target	B_p (MG)	T_{eff}	Mass $M_\odot$	Comp	V	Age (Gyr)	P_{lit}	P_{new}	Refs
G111-49	180-220:	8500	1.07	H	16.2	...	...	$6.68^{+0.02}_{-0.03}$ h	3,9,15
HE1211-1707	50	12-23000	...	He	16.8	...	∼2h	$1.77^{+0.43}_{-0.23}$ h	5,26
PG1015+015	120	12-14000	...	H	16.3	...	98.7 mins	105^{+13}_{-7} mins	19,20,21
PG1031+234	500: - 1000:	15000:	...	H	15.8	...	3.40h	3.53±0.05h	24
PG1533-057	31	20000	...	H	15.3	...	∼1d	1.890±0.001h	31,23
G99-47	20	5790	0.71	H	14.1	4.11	1 hr?	26 – 27.5mins	1,9,10,11,12
G195-19	100:	7160	0.75	He	13.8	2.54	1.33 days	5.8h? & months – yrs	1,17,18
G217-037	≃0.2:	6540	0.74	H	14.4	2.97	2-20? hr	hrs-2.5days	1,2
G227-28	≤0.1:	4780	0.48	H	15.7	4.68	...	months-yrs	1,3
G234-4	0.1:-0.3	4500:	...	H, He	16.3	...	...	mins – days	3
G240-72	≥100	5590	0.81	He	14.2	5.86	≥100y:	months – yrs	1,33,17
LB8827	1:	<20000	...	He	15.8	...	...	2h – 1 day	3
LHS2273	∼10	7160	0.59	H	16.6	1.51	...	35-45mins	22,23
LHS5064	≤ 0.2	6680	0.57	H	15.9	1.60	...	9h – 6days	1,9
LP907-037	≤0.1	9500	1.08	H	14.6	...	...	6.7h:	30,2
PG1658+441	3.5	30000	1.31	H	14.6	...	...	6h – 4days	32,6
PG2329+267	2.3	10000	0.9:	H	15.3	...	...	1.8h:	40
EUVE J1439+75.0	14.8	39500	0.9-1.2	H; DD	15.4	0.005-0.3	...	?	44,9
G99-37	10-20:	6400	0.78	He	14.6	3.90	...	?	1,9
G141-2	3:	6340	0.26	H; DD	15.9	0.93	years?	years	1,34,22
G158-45	16.7	6010	0.71	H	15.9	3.65	11h - 1day	1.44h	1,3
G227-35	170-180	6280	0.90	H	15.5	4.76	≥100y	?	12,1,35
G256-7	4.9	5600	...	H	16.0	...	...	> week	28
GD90	5.5	14000	0.66:	H	15.6	...	...	7.7mins::	3,14,16
GD229	500	16000	≥1.0	He	14.8	...	≥100y	>year	37,38,33,39
Grw+70°8247	320	12070	0.95	He	13.2	0.94	≥100y	>year	1,36,20
HE0107-0158	10:-30:	...	...	He; Bin?	16.4:	...	...	?	4,5
HE1045-0908	20-31	9200	...	H	16.7	...	2-4 hours?	14.3h::	5,25
LB11146	670	16000	0.9	H, He; DD	14.3	...	...	> week	41,42,43
PG0136+251	≤0.1	39190	1.20	H	15.8:	...	...	26.7mins:	6
PG1220+234	3:	27200	0.81	H	15.6	...	...	?	23,27
SBSS1349+545	760	11000:	...	H	16.4	...	...	5.8h::	29
G183-35	14:	6500	...	H, He:	16.9	...	50mins - few yrs	> year	3,28
GD77	1.2	13900	0.63:	H	14.8	...	...	>week	9,13,14

Table 3.3: REFERENCES: (1)Bergeron et al. (2001), (2)ss94, (3)Putney (1997), (4)Reimers et al. (1998), (5)Schmidt et al. (2001), (6)Schmidt et al. (1992), (7)Friedrich et al. (1996), (8)Dupuis et al. (2002), (9)Wickramasinghe & Ferrario (2000), (10)Wickramasinghe & Martin (1979), (11)Greenstein & McCarthy (1985), (12)Putney & Jordan (1995), (13)Schmidt et al. (1992), (14)Guseinov et al. (1983b), (15)Guseinov et al. (1983a), (16)Angel et al. (1974), (17)Angel (1978), (18)Liebert (1976), (19)Wickramasinghe & Cropper (1988), (20)Schmidt & Norsworthy (1991), (21)Schmidt et al. (2003), (22)Bergeron et al. (1997), (23)Schmidt & Smith (1995), (24)Schmidt et al. (1986), (25)Reimers et al. (1994), (26)Reimers et al. (1996), (27)Liebert et al. (2003), (28)Putney (1995), (29)Liebert et al. (1994), (30)Koester et al. (1998), (31)Liebert et al. (1985), (32)Liebert et al. (1983), (33)Berdyugin & Pirola (1999), (34)Greenstein (1986), (35)Cohen et al. (1993), (36)Wickramasinghe & Ferrario (1988), (37)Wickramasinghe et al. (2002), (38)Green & Liebert (1981), (39)Schmidt et al. (1996), (40)Moran et al. (1998), (41)Liebert et al. (1993), (42)Glenn et al. (1994), (43)Schmidt et al. (1998), (44)Vennes et al. (1999)

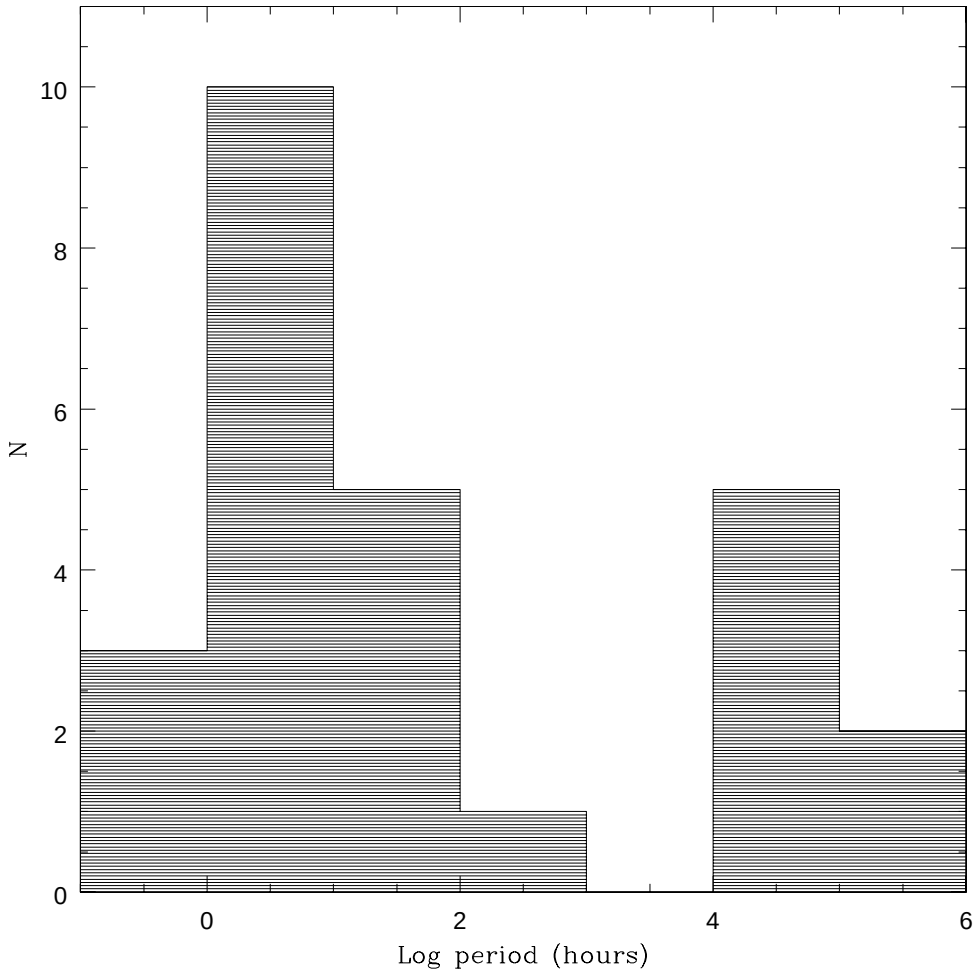

Figure 3.59: Updated period distribution for magnetic white dwarfs. The apparent bimodal distribution is a partly artificial effect as the sources seen to vary over timescales > week have been grouped into a single class with a period of 5 years. The distribution at short periods is real. We expect the peak at $4 < \mathrm{lop(P)} < 5$ to smooth out at we determine more accurate periods from our upcoming Liverpool Telescope data.

down to less than 1% full-amplitude in two targets, and that the majority of our variable sources display variability at the 2 – 3% level. This suggests that our period detection is not significantly biased toward the high-amplitude variables, although we acknowledge that variability below the 1% level in some sources may have been undetected by our survey. It should also be noted that the amplitude of variability quoted may increase for the longer-period targets as more data are taken. If we have currently only observed a small fraction of the phase of the sinusiodal variation, we may not yet have seen the true amplitude of the variability, only a fraction of it.

One of the driving aims behind the survey was to look for correlations between spin period, field strength, mass, temperature and age of magnetic white dwarfs. The lack of exact periods has made this difficult, and for the sources without a reliable period we have simply used the best period from the periodogram, even where the 3σ errors cover a large range of frequencies. Plots of the various parameters against spin period can be found in (Figs 3.61 - 3.64). The variable sources with a defined period have been plotted in red, those which are variable but without a reliable period are in black, those that may be variable are in green, and those that are not seen to vary are in blue. The sources with a defined period also have their errors plotted. I have grouped the targets that are non-variable over the week, but may be varying over months - years, and set their periods to 5 years. I have also grouped the targets thought to have very long periods ($\leq$ 100 years) and set their periods at 100 years. From the these plots it can be seen that there is no obvious correlation between spin period and any other tested parameter, although there may be tentative evidence for a negative correlation between period and magnetic field strength at shorter periods. This is particularly interesting since Ferrario & Wickramasinghe (1997) claimed to have found a positive correlation between these two parameters. We note, however, that our sample size with well-defined spin periods is still very small. We hope to be able to improve the number of targets

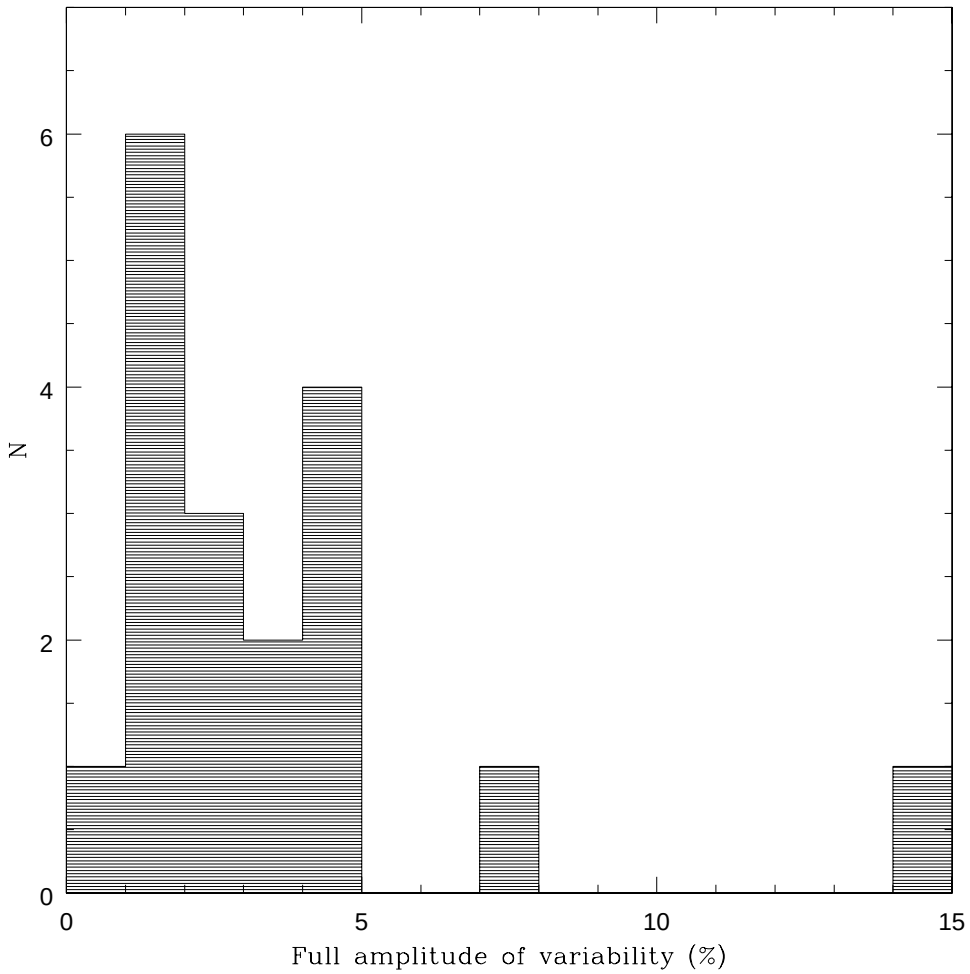

Figure 3.60: Amplitude of variability distribution for our sources. Most appear to be variable on the 2-3% level, and we have successfully detected variability down to an amplitude of $< 1\%$.

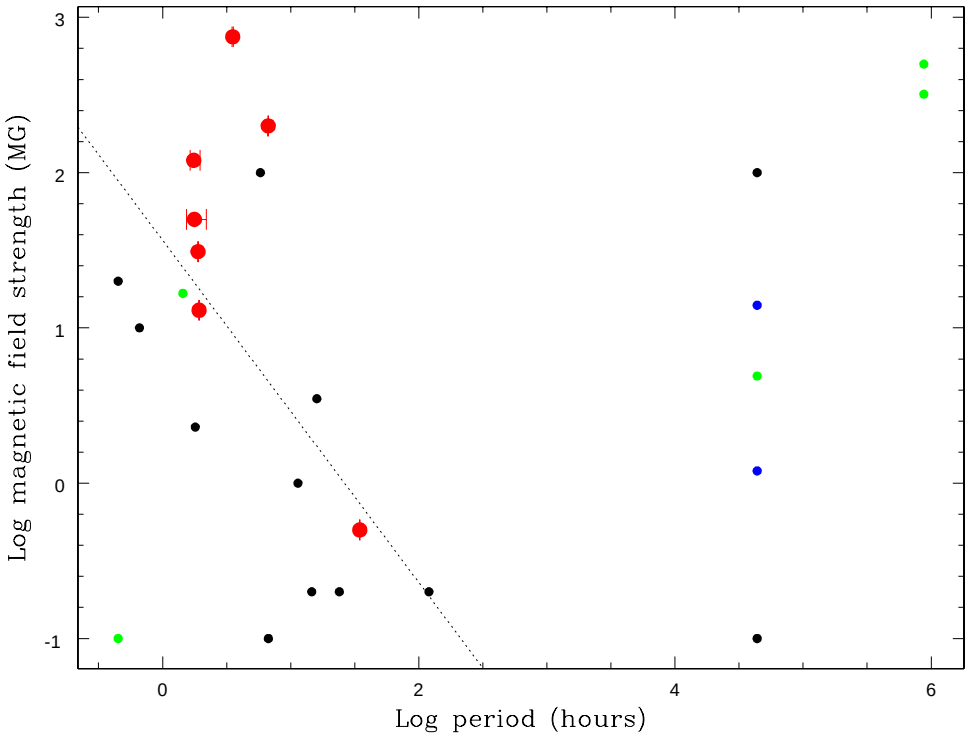

Figure 3.61: Plot of log magnetic field strength (MG) vs log period (hours). Red points are variable sources with well-defined period, black points are variable but without a reliable period, green are the sources which may be variable and blue are those not seen to vary over the timescale of our observations. The dotted line is a straight-line fit through all of the short-period sources.

with a defined period range by collecting more data using the Liverpool Telescope, and carrying out randomisation and Monte-Carlo tests on the existing data in the near future.

One particularly interesting object in our survey is G195-19. We have assumed throughout this work that any variability in these sources is due to their spin period since they are isolated and should have no other source of variability on timescales longer than a few minutes. However, G195-19 may well be varying on two different timescales - one around a few hours - days and another with larger amplitude over a few months. Further observations of this object would be extremely useful in confirming that result.

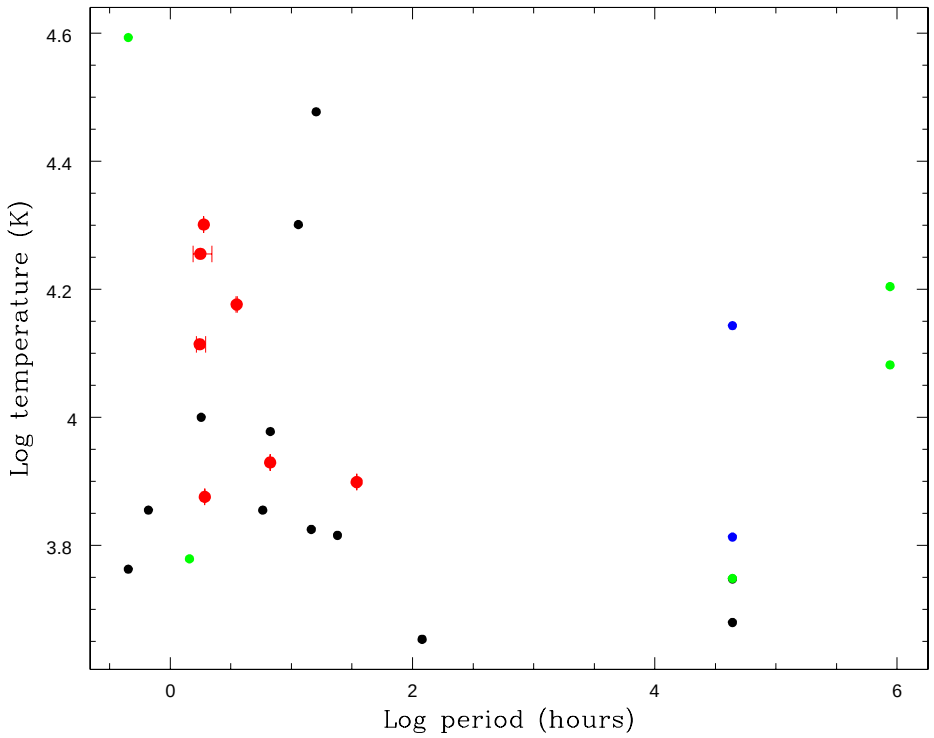

Figure 3.62: Plot of log effective temperature vs log period (hours). Red points are variable sources with well-defined period, black points are variable but without a derived period, green are the sources which may be variable and blue are those not seen to vary over the timescale of our observations.

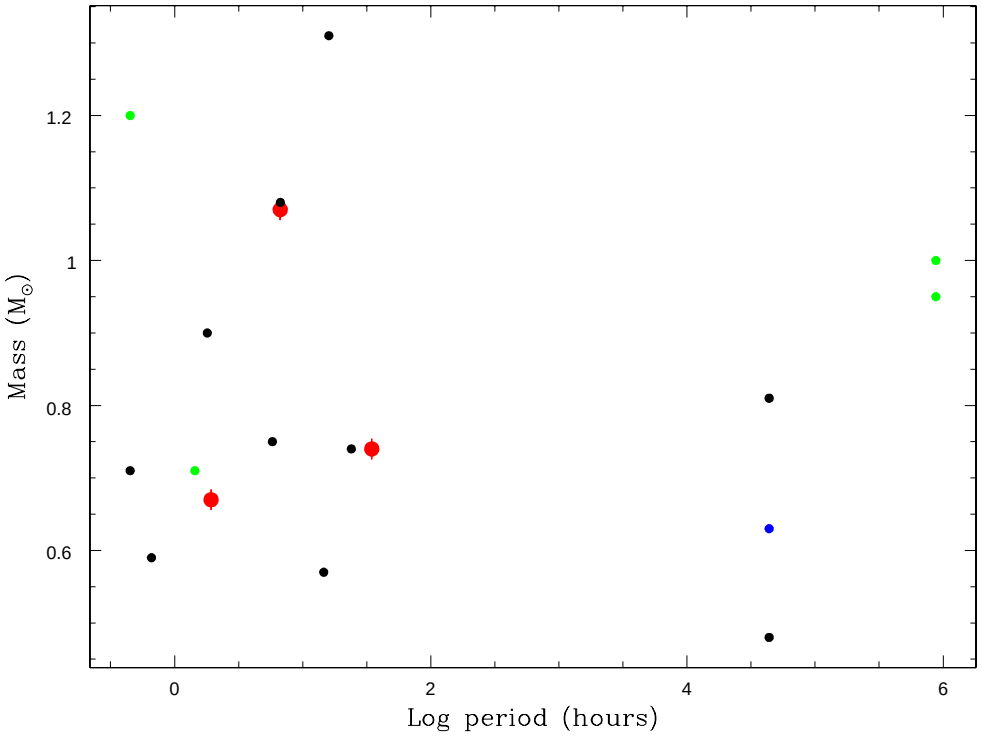

Figure 3.63: Plot of mass vs log period (hours). Red points are variable sources with well-defined period, black points are variable but without a derived period, green are the sources which may be variable and blue are those not seen to vary over the timescale of our observations.

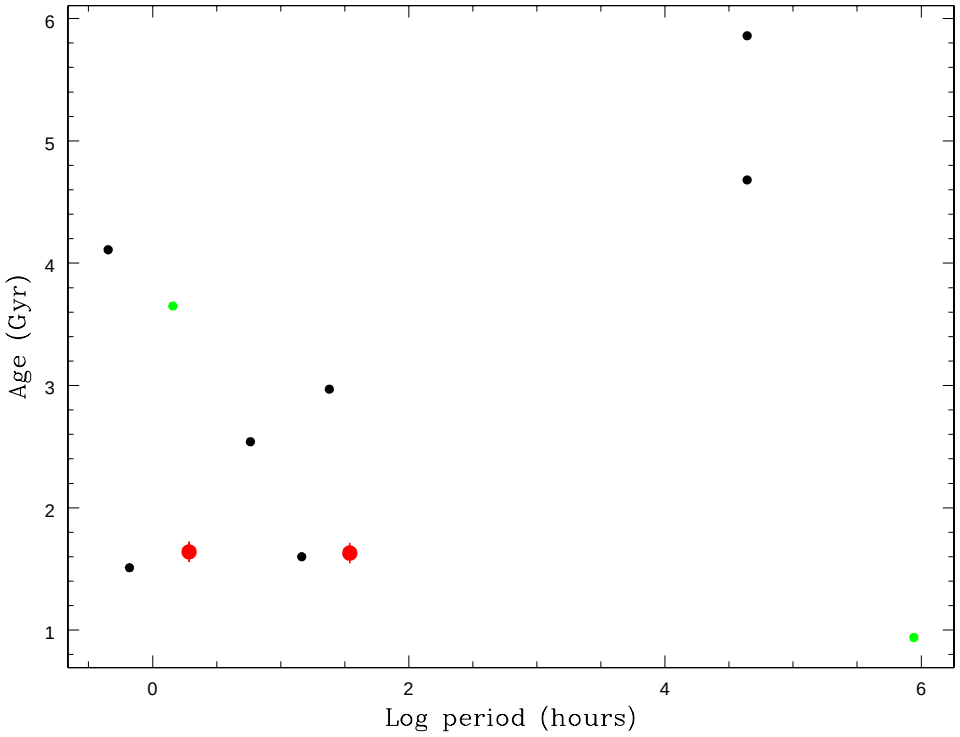

Figure 3.64: Plot of age vs log period (hours). Red points are variable sources with well-defined period, black points are variable but without a derived period, green are the sources which may be variable and blue are those not seen to vary over the timescale of our observations.

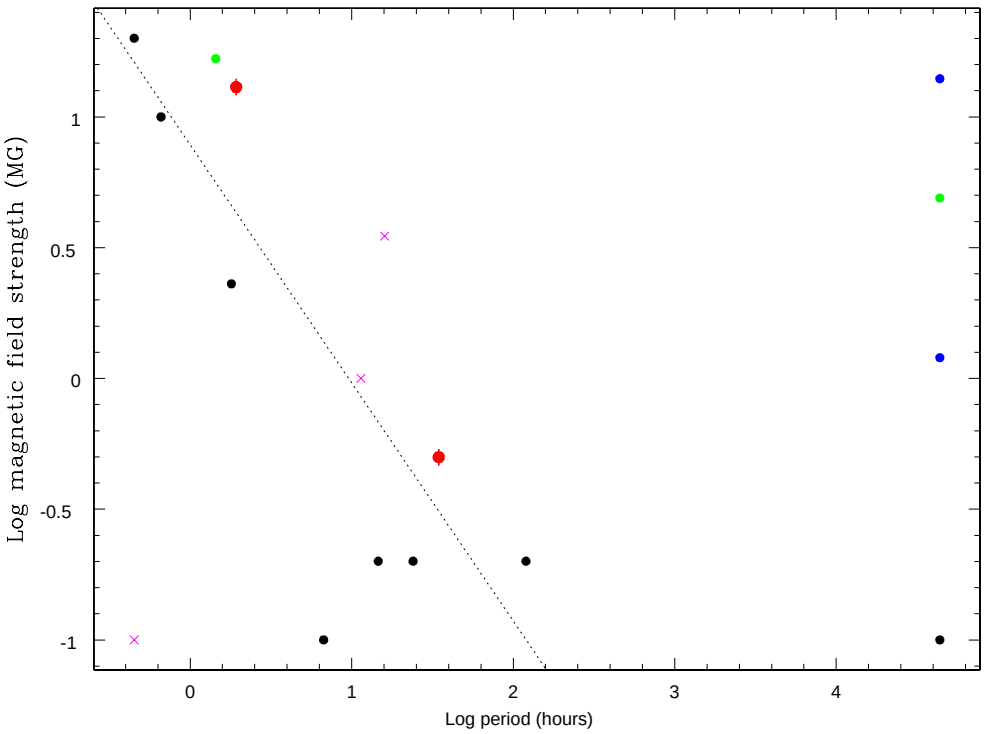

Figure 3.65: Plot of log magnetic field strength (MG) vs log period (hours) for low-field, low-temperature magnetic white dwarfs. These are sources in which the variability may be caused by star spots on the surface of the star. Red points are variable sources with well-defined period, black points are variable but without a derived period, green are the sources which may be variable and blue are those not seen to vary over the timescale of our observations. The magenta crosses are the sources with low field but high temperature (above or around the convective cut-off temperature). Theoretically these should not be variable. The dotted line is a fit through the short-period sources.

Another interesting result is the 14 targets with low temperatures (T < 12000 K) and low magnetic field strengths (B < 20 MG) that are still shown to display variability (Fig 3.65). After the discovery of variability in the cool, low-field magnetic white dwarfs WD 1953-011 and GD 356, we were keen to test our theory that the periodicity is caused by star spots on their surfaces (see Chapter 2 for further discussion). Low-temperature (< 12000 K) magnetic white dwarfs should be able to form star spots since their atmospheres are at least partially convective. If this theory is correct then cool, low-field magnetic white dwarfs should display variability, while hot, low-field ones should not, since their field strengths are not large enough to cause magnetic dichroism, but their temperatures are too high for a convective atmosphere. While we do indeed have 14 cool, low-field targets displaying variability, we also have 3 low-field, hot variable targets. All of these have temperatures above 20000 K, well above the convective cut-off temperature, and therefore almost certainly have fully radiative atmospheres that cannot form star spots. This would suggest that star spots are not the sole cause of variability in low-field magnetic white dwarfs.

3.6 Conclusions

From our sample of 30 isolated, magnetic white dwarfs, we have observed variability in 17 (57%) over our observed timescales. There are a further 11 sources in which we have been unable to confirm or rule out variability, and 2 sources that are non-variable over the observed timescale. In total we have discovered possible variability in fifteen targets that has not been reported before in the literature. We have found no correlation between spin period and age, mass or temperature, but there may a negative correlation between period and field strength for the short-period targets. We note that this will be better determined once more exact periods for the

variable targets are derived. We have identified 14 targets with low field strength and low temperature, which are candidates for having star spots on their surfaces, and these should be followed up with polarimetry, but we have also found that 3 low-field, high-temperature MWDs are unexpectedly variable. Finally, we have identified an unusual source in G195-19, which appears to be displaying variability on two different timescales. More data on this source would be useful. The above results are only the initial findings from our survey. There are a number of issues to resolve, the most important of which is the scatter in the photometry that is not covered by the errors in the data. While we have attempted to compensate for this by scaling the reduced χ^2 of the sinusoidal fits to 1, we have essentially been unable to trust our error bars, which has made the process of identifying variability in our data difficult. Once this has been addressed, we should have a more robust method of identifying the variable targets. Once we have confirmed variability we will then apply Monte-Carlo and randomisation methods to test the robustness of our periods.

Chapter 4

The changing period of NN Ser

4.1 Introduction

The evolution of close binary systems is governed by angular momentum (AM) loss, driven by a combination of gravitational radiation (Kraft et al. 1962; Faulkner 1971), which is dominant for periods $P_{orb} < 3\,h$, and magnetic braking (Verbunt & Zwaan 1981), which dominates for $P_{orb} > 3\,h$ (see Chapter 1 for a more comprehensive discussion). While the mechanisms are well-understood, and the loss rates due to gravitational radiation are well constrained, the strength of magnetic braking is still a matter of debate. The rate of angular momentum loss by magnetic braking is governed by the mass, radius and angular momentum of the magnetically active star, which led to the development of the standard model of binary evolution still used today (Rappaport et al. 1983; Spruit & Ritter 1983). However, there is recent evidence to suggest that the AM loss rate saturates for low-mass stars above a certain value of angular momentum (Sills et al. 2000). This has led to a major revision in magnetic braking loss rates for binaries with low-mass secondary stars, such as cataclysmic variables.

Cataclysmic variables (CVs) are useful for testing close binary evolution, as any theory is constrained by 2 major features in the distribution of CV periods: the period gap and the value of the period minimum (again, see Chapter 1 for a discussion). The value of the minimum period is governed entirely by the angular momentum loss rate for short-period systems. According to the standard theory, systems below the period gap are driven by gravitational radiation alone, which implies that the minimum period should be at $P_{min} = 1.1\,h$. In fact the observed cut-off is at about $P_{min} \simeq 1.3\,h$, suggesting that gravitational radiation alone is not strong enough to reproduce the observed value of P_{min} (see Chapter 1 for further discussion about the CV orbital period distribution) .

The standard model was developed by extrapolation from studies of braking rates of solar-type stars in clusters, but a recent dramatic increase in the amount of data available for stars in these clusters (for reviews see Stauffer et al. 1997; Krishnamurthi et al. 1997; Reid & Mahoney 2000) has shown that this extrapolation to lower masses appears to be totally wrong - low-mass stars retain more of their angular momentum than their higher-mass counterparts. This means that the new suggested $\dot{J}$ is anything between 10 and 10^4 times smaller than assumed in the majority of CV studies. Importantly, there is also no evidence for a cut-off in magnetic braking as the secondary star becomes fully convective (Andronov et al. 2003), so the new data offer no explanation for the existence of the period gap.

We therefore need a way to measure directly the angular momentum loss rates of CVs in order to test the two evolutionary models. One way of doing this is to measure mid-eclipse timings of eclipsing binary systems to find the period change of the system and calculate the angular momentum loss. The period changes are tiny - of order 5×10^{-4} seconds per year - so this is difficult to do in CVs due to contamination of the light curve by the accretion processes. In order to overcome this problem, we have used a non mass-transferring pre-CV, NN Ser.

NN Ser is a white dwarf / M dwarf binary system with an extremely low-mass ($M \sim 0.2\ M_{\odot}$) and therefore fully convective secondary star. The system was first studied in detail by Haefner (1989), who identified it as a deeply eclipsing (> 4.8 mag) pre-cataclysmic variable with a strong reflection effect of ~ 0.6 mag, and an orbital period of 0.13 days. Wood & Marsh (1991) used low-resolution *IUE* spectra to derive the system parameters, which were refined by the radial velocity study of Catalan et al. (1994) to give the values in Table 4.1. The most recent study by Haefner et al. (2004) combines high-speed photometry from the MCCP photometer with VLT trailed photometry and phase-resolved spectroscopy. This allows them to put good constraints on the temperature of the secondary star. They also attempt to derive accurate values for the radii and masses of the system components, but their values depend on their failure to detect the secondary eclipse for NN Ser, which caused them to derive a binary inclination of $i = 84.6^{\circ} \pm 1.1^{\circ}$. We have detected the secondary eclipse in our ULTRACAM data (see Fig. 4.1), and our preliminary modelling indicates that the true inclination is $i \sim 88^{\circ}$. Full results of our modelling will be the subject of future work, but we conclude from our initial results that Haefner et al. (2004) have overestimated the radius (and therefore the mass) of the secondary star by $\sim 15\%$. Nevertheless, we carry out all of our analysis for all values of mass and radius included in the uncertainties given by Catalan et al. (1994) and Haefner et al. (2004). All four studies also give eclipse timings (listed in Table 4.3) which we have used to extend our baseline for measuring the period change to $\sim$ 15 years. NN Ser is ideally suited for this study as there is no mass transfer, so the light curve is uncontaminated, and the deep primary eclipses give rise to very sharp ingress and egress features. Given the high-time resolution of ULTRACAM, we are able to estimate the times of mid-eclipse to a typical accuracy of ~ 0.15 s.

Table 4.1: System parameters of NN Ser

	Catalán et al. 1994 Wood & Marsh, 1991	Haefner et al. 2004
Binary separation	$0.95 \pm 0.025\ R_\odot$	$0.9543 \pm 0.0233\ R_\odot$
Inclination	$84° < i < 90°$	$84.6° \pm 1.1°$
Mass ratio	$0.18 < q < 0.23$	0.2778 ± 0.0297
White dwarf mass	$0.57 \pm 0.04\ M_\odot$	$0.54 \pm 0.05\ M_\odot$
RD mass	$0.1 < M_\odot < 0.14$	$0.150 \pm 0.008\ M_\odot$
WD radius	$0.017 < R_\odot < 0.021$	$0.0189 \pm 0.0010\ R_\odot$
RD radius	$0.15 < R_\odot < 0.18$	$0.174 \pm 0.009\ R_\odot$
White dwarf temp.	$55000\,K \pm 8000\,K$	$57000\,K \pm 3000\,K$
RD temp.	$2900\,K \pm 150\,K$	$2950\,K \pm 70\,K$
RD irradiated temp.	$5650\,K < T < 8150\,K$	$7125\,K \pm 200\,K$
RD spectral type	M4.7 - M6.1	M4.75 ± 0.25
Distance	$356\ pc < d < 472\ pc$	$500 \pm 35\ pc$

Table 4.2: Observation log for ULTRACAM observations of NN Ser

Date	Filters	No. eclipses	Conditions
17/05/2002	u'g'r'	2	good, seeing ∼1.2"
18/05/2002	u'g'r'	1	variable, seeing 1.2" - 2.4"
19/05/2002	u'g'r'	1	fair, seeing ∼2"
20/05/2002	u'g'r'	1	fair, seeing ∼2"
19/05/2003	u'g'z'	1	variable, seeing 1.5" - 3"
21/05/2003	u'g'i'	1	excellent, seeing ∼1"
22/05/2003	u'g'i'	1	excellent, seeing <1"
24/05/2003	u'g'i'	1	good, seeing ∼ 1.2"
03/05/2004	u'g'i'	3	variable, seeing 1.2" - 3.2"
04/05/2004	u'g'i'	1	variable, seeing 1.2" - 3"

4.2 Data acquisition

The data were taken with the ultra-fast, triple-beam CCD camera, ULTRACAM (see Dhillon & Marsh 2001 for a review). We used the camera in conjunction with the 4.2m William Herschel telescope at the ING to observe NN Ser simultaneously in the Sloan u', g' and either r', i' or z' bands. We were able to achieve a time resolution of ~ 2.06 s. The observations were taken over a period of 2 years, in May 2002 – 2004, and during those runs we observed 13 primary eclipses of the system. We were also able to observe a number of secondary eclipses as the white dwarf transited the secondary star (see Fig. 4.1). The pixel size for the 3 ULTRACAM CCDs is 13μm, with a scale of 0.3"/pix. Readout noise is 3.10 – 3.40 e, depending on the CCD, while the gain is 1.13 – 1.20 e/ADU. A full list of observations and observing conditions is given in Table 4.2. The weather in May 2004 was particularly variable, leading to larger errors in our measured times for that epoch.

The data were reduced using the ULTRACAM pipeline software written by TRM. Differential photometry was performed on the target, with respect to a nearby, bright, non-variable comparison star.

4.3 Analysis & Results

4.3.1 Eclipse timings

All MJD times were corrected to barycentric time, then additionally corrected for light travel time to the Solar System barycentre. While this may seem non-intuitive, it should be noted that Barycentric Dynamical time (TDB) is actually the time on Earth converted to a hypothetical time in a gravitationally uniform, perfectly circular Solar orbit, therefore light travel time corrections must still be applied. All times are therefore listed in MJD(BTDB). In order to measure accurate eclipse times, we needed a model of the eclipse of the white dwarf, which was calculated by TRM as follows. We defined the two stars by their radii relative to the separation of the binary. Since we allowed for tidal deformation of the M dwarf (but not the white dwarf), the radius of the M dwarf was measured from its centre of mass towards the white dwarf. Apart from the relative radii, we also require the binary mass ratio and inclination, stellar effective temperatures and linear limb darkening coefficients to define our model binary. The two stars were divided into many small elements. The temperatures of the elements covering the M dwarf were set, accounting for incident flux from the white dwarf by adding fluxes so that

$$\sigma T_2'^4 = \sigma T_2^4 + F_{\rm irr},$$

where σ is the Stefan-Boltzmann constant, T_2 is the initial (internal) temperature of the secondary element and $F_{\rm irr}$ is the power per unit area accounting for projection

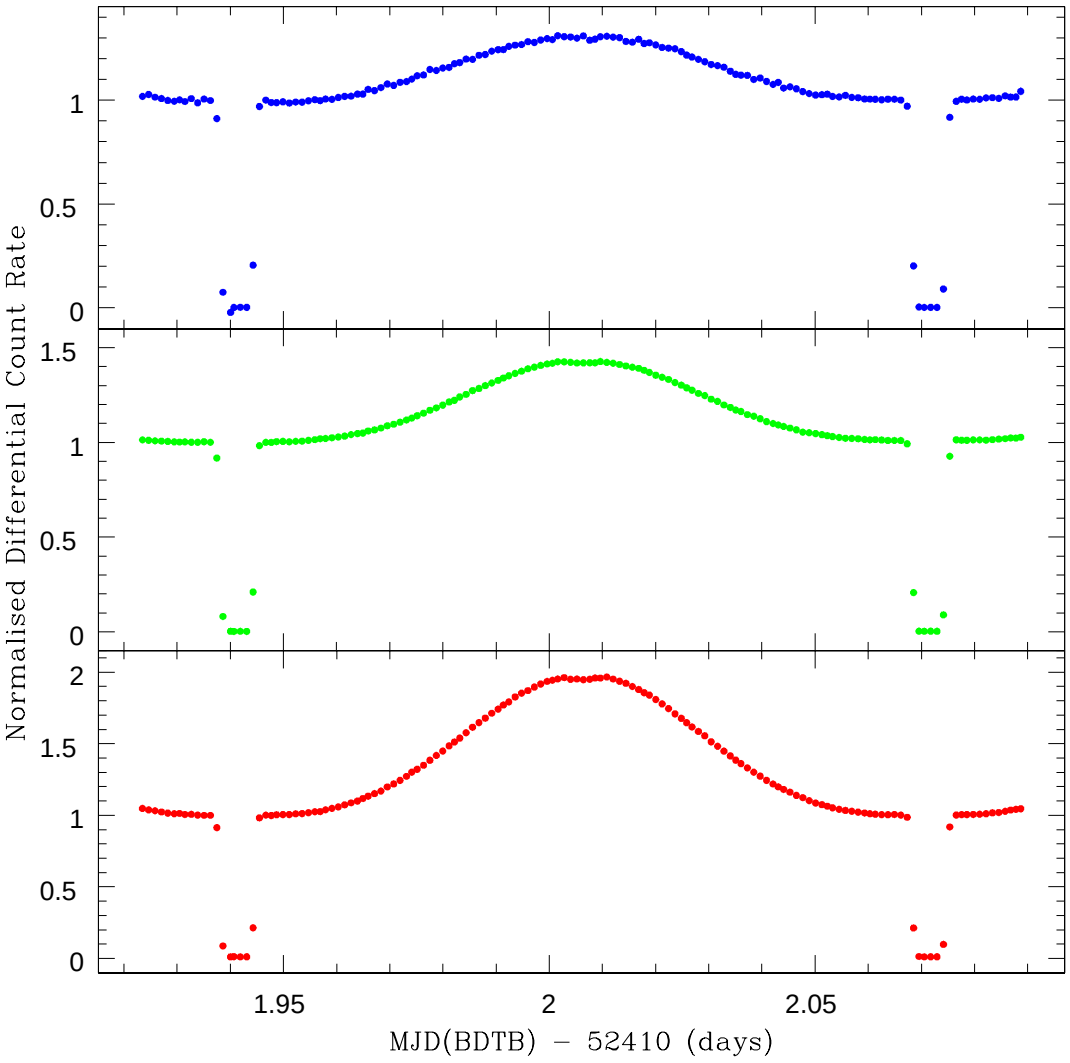

Figure 4.1: Binned differential light curves for NN Ser, taken simultaneously in the u', g' and r' Sloan filters from top to bottom respectively. The light curves are binned by a factor of 43. The hump in the light curve is caused by the reprocessing of light from the WD by the cool secondary star. A shallow secondary eclipse can be detected at the top of the reflection hump in the r' and g' bands.

Table 4.3: Measured times of mid-eclipse for each of the 13 observed primary eclipses of NN Ser. Times were measured for all 3 wavebands simultaneously observed with ULTRACAM and are given in MJD(BTDB), i.e. MJD corrected for general relativity effects and light travel time to the Solar System barycentre. The red filter varied between nights, so the filter used is listed in the final column. *Timing problems were noted to have occurred during cycle 8 (see Section 4.3.1 for details).

Cycle Number	u' eclipse time	uncertainty $1\ \sigma$	g' eclipse time	uncertainty $1\ \sigma$	r'/i'/z' eclipse time	uncertainty $1\ \sigma$	red filter
0	52411.9470588	0.0000020	52411.9470564	0.0000005	52411.9470577	0.0000010	r'
1	52411.0771385	0.0000016	52412.0771385	0.0000005	52412.0771383	0.0000010	r'
8*	52412.9876761	0.0000030	52412.9876977	0.0000008	52412.9876721	0.0000013	r'
16	52414.0283427	0.0000030	52414.0283394	0.0000006	52414.0283379	0.0000016	r'
24	52415.0689716	0.0000025	52415.0689810	0.0000007	52415.0689795	0.0000016	r'
2822	52779.0331646	0.0000021	52779.0331696	0.0000010	52779.0331362	0.0000100	z'
2838	52781.1144524	0.0000015	52781.1144513	0.0000006	52781.1144567	0.0000014	i'
2846	52782.1550904	0.0000021	52782.1550929	0.0000006	52782.1550948	0.0000011	i'
2860	52783.9762155	0.0000022	52783.9762151	0.0000007	52783.9762110	0.0000020	i'
5512	53128.9486787	0.0000070	53128.9486778	0.0000040	53128.9486611	0.0000800	i'
5513	53129.0787555	0.0000027	53129.0787597	0.0000022	53129.0787487	0.0000050	i'
5514	no data	n/a	53129.2088356	0.0000020	53129.2088355	0.0000027	i'
5520	53129.9893197	0.0000050	53129.9893229	0.0000025	53129.9893148	0.0000040	i'

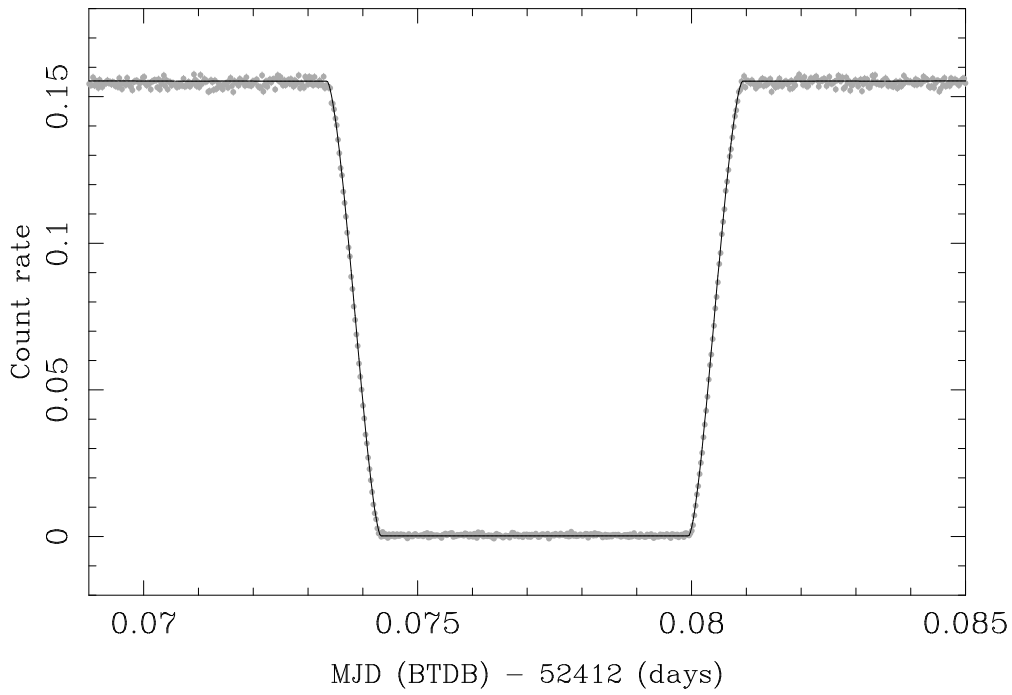

Figure 4.2: Differential light curve for NN Ser in g' with light curve model overplotted.

and the distance from the white dwarf. The surface brightness of each element was then set assuming black-body spectra, and given the effective wavelength of the filter in question. Once the surface brightnesses were set, the model light-curves were computed by summing over all elements, testing for which were in view and not eclipsed and accounting for their projected areas. The eclipse by the M dwarf was computed, allowing once again for tidal distortion. Our assumption of black-body spectra for the two stars is physically unrealistic, but for the eclipse times of this paper, the key element is to have a model that can match the shape of the primary eclipse, which ours does well (Fig. 4.2). The timings and associated errors for the mid-eclipses in all of the wavebands are given in Table 4.3. The errors on our mid-eclipse timings are typically $\sim 0.15\,\mathrm{s}$.

We derive a best-fit linear ephemeris for NN Ser as

Table 4.4: Previous eclipse times of NN Ser. References: (1) Haefner (1989); (2) Wood & Marsh (1991); (3) Pigulski & Michalska (2002); (4) Haefner (2004).

Time of mid-eclipse MJD(BTDB)	Cycle Number	Reference
47344.025(5)	0	1
47703.045744(2)	2760	4
47703.175833(6)	2761	4
47704.216460(3)	2769	4
47705.127023(3)	2776	4
47705.257115(7)	2777	4
47712.28158(15)	2831	2
47713.32223(15)	2839	2
48301.41420(15)	7360	2
51006.0405(2)	28152	4
51340.2159(2)	30721	4
51666.9779(4)	33233	3

$$\mathrm{MJD(BTDB)} = 47344.0246049(14) + 0.130080144430(36)\mathrm{E}.$$

The times of mid-eclipse were then plotted against cycle number. We found that all 13 of the ULTRACAM points except for one (cycle 8) were in agreement with each other, and that the one discrepant point showed a time shift of 2.06 s - exactly the same timing as one exposure. We therefore concluded that the GPS timestamp had slipped by one exposure for that point, and corrected it by 2.06s to bring it in line with the other points. Old eclipse timings from the literature (Haefner 1989; Wood & Marsh 1991; Pigulski & Michalska 2002; Haefner et al. 2004; Table 4.4)

were then added to the plot. The residuals after subtracting a straight-line fit can be seen in Fig.4.3.

The data, with eclipse times t_E, were fit with a parabola of the form:

$$t_E = T_0 + AE + BE^2. \tag{4.1}$$

The period derivative can then then be found using

$$\dot{P} = \frac{2B}{P}. \tag{4.2}$$

We found that the period derivative over the 15 years of observations appears to be increasing, so we fit all of the data to find an average rate of period change, and just the ULTRACAM data to find the current rate.

The angular momentum of the system as a whole is given by

$$J = \left(\frac{Ga}{M}\right)^{1/2} M_1 M_2, \tag{4.3}$$

where M_1, M_2 and M are the primary, secondary and total masses respectively. Combining this with Kepler's third law,

$$\frac{4\pi^2}{P^2} = \frac{GM}{a^3}, \tag{4.4}$$

we find that, for a detached system (where M_1, M_2 and M are constant),

$$\frac{\dot{J}}{J} = \frac{2}{3}\frac{B}{P^2}. \tag{4.5}$$

For NN Ser, our measured value for the average rate of period change is

$$\dot{P}_{av} = 9.06 \times 10^{-12} \pm 0.06 \times 10^{-12}$$

and for the current rate of period change

$$\dot{P}_{cur} = 2.85 \times 10^{-11} \pm 0.15 \times 10^{-11}.$$

Taking $0.1\,M_\odot \leq m_2 \leq 0.14\,M_\odot$ and $0.15\,R_\odot \leq r_2 \leq 0.18\,R_\odot$ (Catalan et al., 1994), this corresponds to angular momentum loss rates of

$$0.84 \times 10^{35} \leq \dot{J}_{av} \leq 2.09 \times 10^{35}\text{ergs}.$$

and

$$2.52 \times 10^{35} \leq \dot{J}_{cur} \leq 6.87 \times 10^{35}\text{ergs}.$$

where the relatively large allowed range is caused by the uncertainties in the system parameters, where we have assumed that the system parameters are independent of each other. Obviously this will overestimate the size of the uncertainty in our measured angular momentum loss rate for any one value of secondary mass. When carrying out the analysis of period loss mechanisms in Section 4.4, we have used a more realistic approach, relating the secondary radius to its mass, using the M-R relation for secondaries in binary stars given in Gorda & Svechnikov (1998) and calculating the resulting separation of the binary. This then gives a range of values for the angular momentum change that are specific to each value of secondary mass.

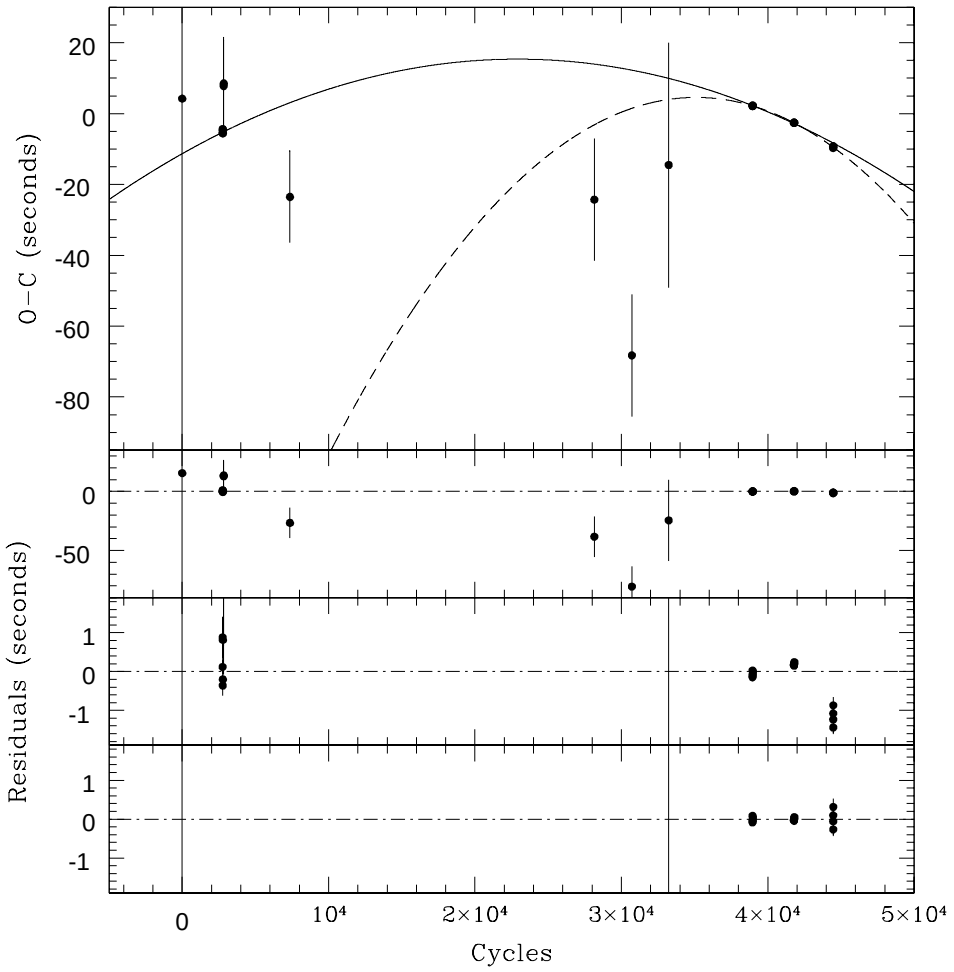

Figure 4.3: The upper plot is an O-C diagram showing the period change in NN Ser. The solid line is a fit through all the data (average rate of period change), while the dashed line is a fit through the ULTRACAM data only (current rate of period change). The lower three plots are (from uppermost): residuals after a fit through all the data is subtracted, showing all the points; residuals after the fit through all the data is subtracted, zoomed in on the ULTRACAM points; residuals after the fit through the ULTRACAM data is subtracted, zoomed in on those points.

4.4 Discussion - Mechanisms for period change

Period changes in most binary systems are generally thought to be due to one of three mechanisms:

1. Applegate's (1992) mechanism, where period changes are caused by coupling between the binary period and changes in the shape of the secondary star;

2. the presence of a third body in a long orbit around the binary. This affects the light travel-time, which can be mis-interpreted as a change in the binary period. For example, as the binary moves towards the observer, the eclipses are seen to occur more frequently than when the binary is moving away.

3. a genuine angular momentum loss from the system.

For some binary systems, period changes can also be the result of conservative mass-transfer between system components, where the minimum period occurs when the masses of the two components are equal. Since conservative mass-transfer does not take place in CVs or pre-CVs such as NN Ser, we discount this mechanism from further analysis.

We show below that the most commonly suggested cause of binary period change - Applegate's (1992) mechanism - cannot work for NN Ser: the luminosity of the secondary star is too low to provide the necessary energy. We also discuss the other two mechanisms in detail, along with the ramifications for binary evolution.

4.4.1 Applegate's mechanism

Applegate (1992) proposed that observed orbital period modulations could be induced in binary systems by the gravitational coupling of the binary orbit to variations in the shape of the magnetically active secondary star. These variations in shape are caused by the cyclic redistribution of angular momentum within the star by a magnetic torque. To test this theory for NN Ser, we used the equations in Applegate (1992) to calculate the luminosity change required to support the observed period change.

The total period change seen in NN Ser, ΔP, is $\dot{P}\times$ total observed time. With the eclipse timings from the literature, the total observed time between the MCCP and the ULTRACAM data is 14.9 years, which gives a total period change of $\Delta P = (4.26 \pm 0.03) \times 10^{-3}$ s.

The change in angular momentum required to drive this ΔP is given by

$$\Delta J = -\frac{GM^2}{R}\left(\frac{a}{R}\right)^2 \frac{\Delta P}{6\pi} \tag{4.6}$$

where M and R are the mass and radius of the secondary star and a is the binary separation. Applegate (1992) showed that the amount of energy required to support this change in angular momentum is

$$\Delta E = \Omega_{dr}\Delta J + \frac{(\Delta J)^2}{2I_{eff}} \tag{4.7}$$

where $\Omega_{dr} = \Omega_s - \Omega_*$ is the angular velocity of differential rotation, which we approximate as $\Omega_{dr} \simeq \Delta\Omega/\Omega \sim 0.014$. I_{eff} is the effective moment of inertia. In the numerical examples in Applegate (1992), the differentially rotating shell mass is

typically $M_s \simeq 0.1M$, so we can approximate the moment of inertia as

$$I_s = \frac{2}{3} M_s R^2, \tag{4.8}$$

where $I_{eff} = 2I_s$. When calculating these values for NN Ser, we calculated the mass of the secondary star for a given radius using the mass-radius relation for binary secondary stars from Gorda & Svechnikov (1998). We then used Kepler's law to calculate the binary separation. This gives a value for the total energy required to drive the period change of NN Ser of 7.1×10^{39}ergs $\leq \Delta$E $\leq 1.8 \times 10^{40}$ergs.

We can relate the energy required for the observed period change to the amount of energy that has been generated by the secondary star over the lifetime of our observations. The luminosity of the secondary star is $L_2 = 4\pi R^2 \sigma T_{eff}^4$, which, for NN Ser's secondary star with 2880 K $<$ T$_{\rm eff}$ $<$ 3020 K, gives

$$2.5 \times 10^{39}\text{ergs} \leq \text{E}_2 \leq 4.5 \times 10^{39}\text{ergs},$$

A plot of the ratio of the energy required over the energy generated vs the secondary mass is shown in Fig. 4.4. It can be seen that the energy generated by the secondary star is too small to drive Applegate's mechanism in this system, for all allowed values of secondary radius. Since the current rate of period change in NN Ser is higher than the average rate, the ratio of energy required over energy generated is greater, so Applegate's mechanism fails for the current rate of period change by an even larger amount.

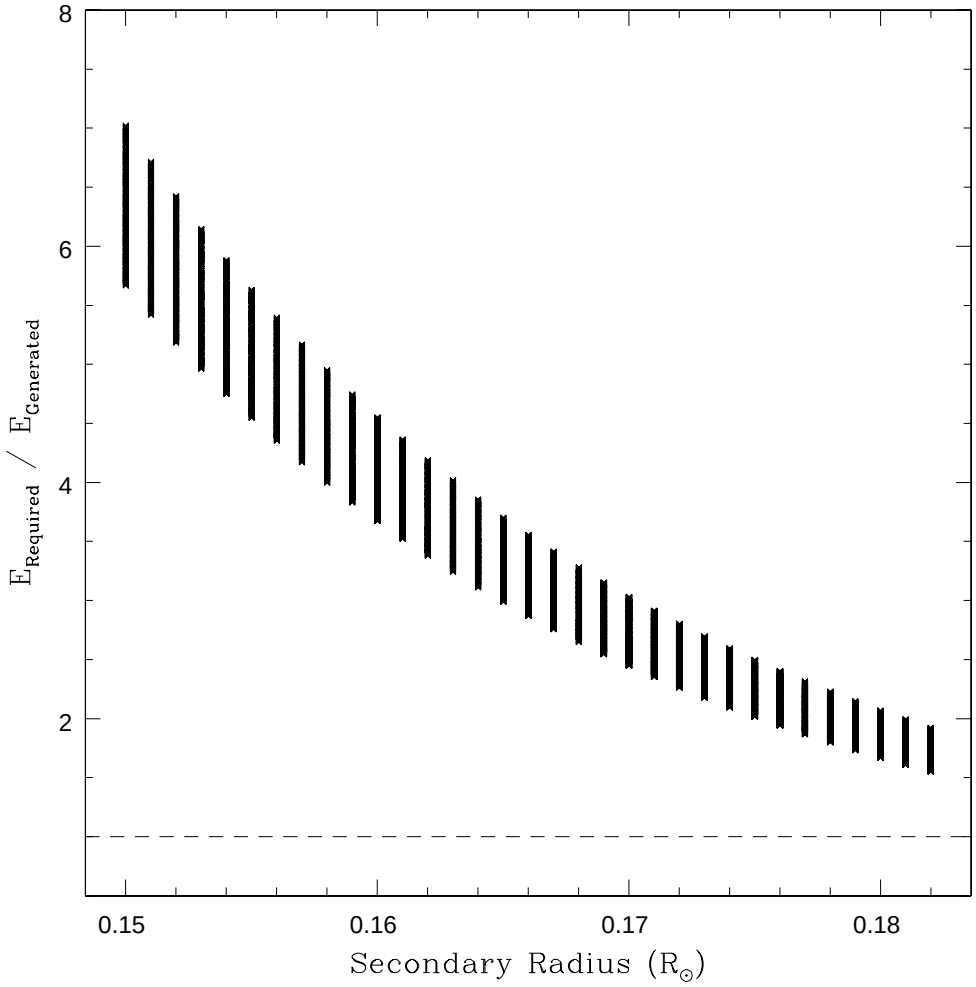

Figure 4.4: Ratio of energy required for Applegate's mechanism over energy generated by the secondary star, vs secondary radius. The spread of energy ratios at each mass are due to the uncertainties in the observed period change and the temperature of the secondary star. Dashed line is at a ratio of 1, i.e. Applegate's mechanism for period change is only possible below this line.

4.4.2 Third body

Apparent changes in the orbital periods of binary stars have often been attributed to the light-travel time variation caused by third bodies, although further observation often reveals that this cannot be the case. However with the relatively limited coverage to date, this is at least a possibility for NN Ser which we investigate in this section.

Changes in eclipse timings of binary stars do not necessarily indicate a genuine change in the binary period. A third body in a long orbit around the binary can cause small but significant changes in the light-travel time from the binary system, which manifest themselves as strictly sinusoidal changes in the timings of mid-eclipse. We are able to put constraints on the mass and period of any third body which could cause the observed period change in NN Ser by fitting all possible sine waves to a plot of mid-eclipse timings vs cycle number. A function of form

$$T = T_0 + P_{orb}E + A_3 \sin\left(\frac{2\pi(E - E_3)}{P_3}\right)$$

was fitted to the plot for values of P_3 between 2 and 500000 days, where P_{orb} was kept fixed at the orbital period of the binary, P_3 is the modulation period of the period change, A_3 is the amplitude of the period modulation, and $E - E_3$ is a measure of the phase of the zero point of the modulation with respect to the zero point of the binary period. As we are interested in the minimum possible mass, we assumed that the inclination of the orbital plane of the third body is aligned with the line of sight, i.e. $\sin i = 1$. This gave us the values of A_3 for all possible modulation periods between 2 and 500000 days. From this, we were able to use Kepler's law and the observed luminosity of NN Ser to find the range of allowable masses of the third body which could cause the observed period change in NN Ser. The minimum possible mass comes from the fact that we have not seen a reversal

in the period change of NN Ser. The minimum value of P_3 is therefore $\sim$ 30 years, which corresponds to a minimum mass of $M_3 = 0.0043\,\mathrm{M}_\odot$.

The maximum value of M_3 comes from the luminosity of the binary system in eclipse. The luminosity of the third body must be equal to or less than the observed mid-eclipse luminosity. This means that it must have a mass equal to or less than that derived for the secondary star. If the maximum mass is $0.18\mathrm{M}_\odot$ then the maximum orbital period for any third body is $P_3 = 1.042 \times 10^5$ days $\sim$ 285 years.

We therefore find that a low-mass companion to the binary system could cause the observed changes in mid-eclipse timings that we observe in NN Ser, and that the long periods suggested by our data would be able to accommodate NN Ser's primary even before its evolution to a white dwarf. Our results also indicate that measuring eclipse timings of binary systems is potentially a very sensitive method of detecting extra-solar planets in long-period orbits.

4.4.3 Comparison with angular momentum loss models

Angular momentum loss in CVs and pre-CVs is governed by two mechanisms - gravitational radiation and magnetic braking. The rates of AM loss caused by both mechanisms must be added together to find the total AM loss for the system. We compare the measured angular momentum loss rate for NN Ser to both the values predicted by the standard CV magnetic braking rate (Rappaport et al. 1983), based on extrapolation from studies of braking rates of solar-type stars in clusters, and to the reduced magnetic braking rate (Sills et al. 2000), based on more recent data, for which the angular momentum saturates at lower masses. Under the standard model, the angular momentum, J, decreases as $\dot{J} \propto -\omega^3$ (Skumanich 1972a), where ω is the angular velocity of the star. However, the reduced braking model suggests

that the angular momentum loss is best modelled as $\dot{J} \propto -\omega^3$ for $\omega < \omega_{crit}$ and $\dot{J} \propto -\omega$ for $\omega > \omega_{crit}$, where the threshold rate, ω_{crit} is much lower than the rotation rates of CVs. This means that the new suggested $\dot{J}$ is anything between 10 and 10^4 times smaller than assumed in the majority of CV studies.

If this is correct, we require a large-scale revision of CV evolution, possibly with systems staying at an approximately fixed period throughout their lifetime rather than migrating from long to short periods. However, such a model has significant problems when compared to observations, particularly as the mass transfer rate should be much lower than seen in the high accretion rate group of CVs known as novalike variables.

Both models were applied to CV studies by Andronov et al. (2003), hereafter APS03.

4.4.3.1 Gravitational radiation

We use the same expression for AM loss due to gravitational radiation as used in APS03, although this was misquoted in their paper. The correct expression is given by:

$$\left(\frac{dJ}{dt}\right)_{grav} = -\frac{32}{5}\frac{G^{7/2}}{c^5}a^{-7/2}M_1^2M_2^2M^{1/2} \tag{4.9}$$

where M_1, M_2 and M are the white dwarf mass, secondary star mass and total mass respectively, and a is the binary separation given by Newton's form of Kepler's third law $a = (GM/\Omega^2)^{1/3}$, where Ω is the orbital angular velocity of the system. For NN Ser this gives a range of values of 5.75×10^{32} ergs $< \dot{J}_{grav} < 1.74 \times 10^{33}$ ergs, over 100 times smaller than required to drive our measured value of $\dot{P}$ for NN Ser.

4.4.3.2 Standard magnetic braking model

The standard model for magnetic braking in CVs is based upon studies of the solar wind and and the rotation periods of solar-type stars in open clusters (Weber & Davis 1967; Skumanich 1972b). Skumanich (1972a) found that the rotational velocity of G-type main sequence stars decreases with time, t as $t^{-0.5}$ (the Skumanich law). Rappaport et al. (1983) developed a prescription based upon this empirical relation that is still commonly used in CV studies. This relationship is given by

$$\left(\frac{dJ}{dt}\right)_{mb} \approx -3.8 \times 10^{-30} M_{\odot} R_{\odot}^{4} m_2 r_2^{\gamma} \omega^3 \text{ergs}, \tag{4.10}$$

where $0 \leq \gamma \leq 4$ is a dimensionless parameter and ω is the angular frequency of the rotation of secondary star (= binary period for CVs) in rad s^{-1} . We applied this to NN Ser to find the predicted standard angular momentum loss rate for this pre-CV. The results can be seen in Fig. 4.5. APS03 cut off the standard magnetic braking model at a secondary mass of $0.3 M_{\odot}$ to satisfy the standard CV theory. This states that as the secondary star becomes convective, the magnetic field is no longer locked to the stellar core and so dissipates, cutting off the magnetic braking mechanism. APS03 suggested that there is no evidence for this cut-off, so we have not applied it here. We find that by ignoring the magnetic braking cut-off, this model can explain the observed loss rates seen in NN Ser.

4.4.3.3 Reduced magnetic braking model

The more recently proposed model for angular momentum loss due to magnetic braking was applied to CVs in APS03. Studies of the rotational periods of low-mass stars (Queloz et al. 1998; Collier-Cameron & Jianke 1994; Keppens et al. 1995;

Krishnamurthi et al. 1997; Sills et al. 2000) all showed that the standard model overestimates angular momentum loss rates for periods below 2.5 – 5 days and that a modification of the standard model was required for those high rotation rates. APS03 modelled the modified angular momentum loss rates using a prescription with the same functional form as that of Sills et al. (2000), given by

$$\left(\frac{dJ}{dt}\right)_{mb} = -K_w \sqrt{\frac{r_2}{m_2}} \begin{cases} \omega^3 & \text{for } \omega \leq \omega_{crit} \\ \omega\omega_{crit}^2 & \text{for } \omega > \omega_{crit} \end{cases} \tag{4.11}$$

where ω_{crit} is the critical angular frequency at which the angular momentum loss rate enters the saturated regime. The constant $K_w = 2.7 \times 10^{47}$ g cm s^{-1} is calibrated to give the known solar rotation rate at the age of the Sun (Kawaler 1988). The values of ω_{crit} were calculated from the values of $\omega_{crit\odot}$ given in Sills et al. (2000), using the relationship between ω_{crit} and convective turnover time at 200 Myr, τ, from Krishnamurthi et al. (1997):

$$\omega_{crit} = \omega_{crit\odot} \frac{\tau_\odot}{\tau}. \tag{4.12}$$

The values of τ were taken from Kim & Demarque (1996).

Again, the prescription was applied to NN Ser. Results are shown in Fig. 4.5. Our plot differs significantly from the original plot in APS03 due to their mis-calculation of the angular momentum loss due to gravitational radiation. By applying the correct gravitational radiation loss rate, the total angular momentum loss rates predicted by APS03 are within ~ 1 order of magnitude of the standard magnetic braking model rather than ~ 2 orders of magnitude lower, as they originally claimed. However, this is still too low to explain the loss rates seen in NN Ser.

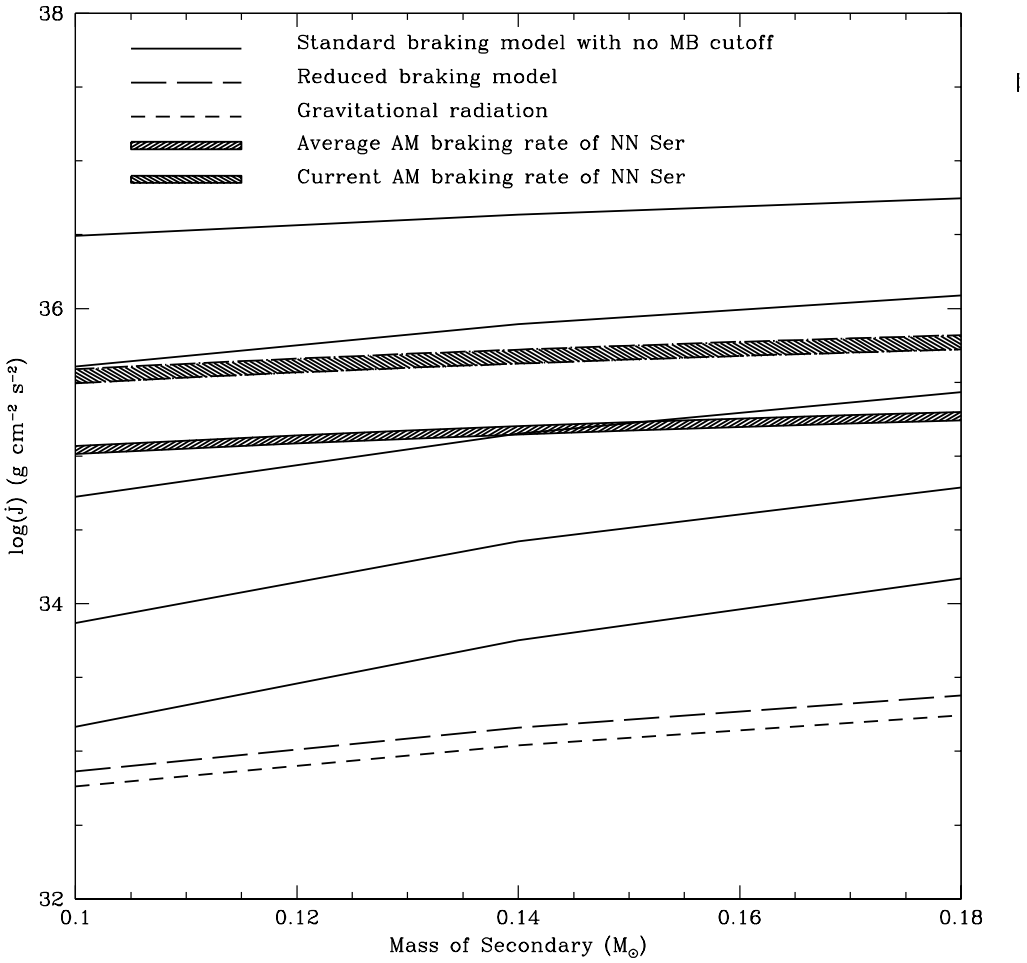

Figure 4.5: Plot of the braking rates predicted by gravitational radiation and the standard and reduced braking models for NN Ser. The different plots for the standard model are for different values of $\gamma = 0,1,2,3,4$, from the top down. The shaded regions show our measured values of the average and current braking rates for NN Ser.

4.5 Discussion

We have found that only two mechanisms can explain the observed period change in NN Ser - either a genuine angular momentum loss from the system or an unseen third body in orbit around the binary. In the case of an angular momentum loss, our observations show that the system is losing angular momentum at a rate consistent with the Skumanich law, but only if we assume that magnetic braking is not cut off as the secondary star's mass reaches $0.3\,M_{\odot}$. APS03 pointed out that an increase in the angular momentum loss rate at low periods can solve a major problem regarding the theoretical vs observed values of the period minimum. If CV evolution at $P < 2\,h$ were driven solely by gravitational radiation, Patterson (1998) demonstrated that the period minimum should be at 1.1 h rather than the observed value of 1.3 h. He also noted that the angular momentum loss rates would be very low for these short-period systems, implying a low mass-accretion rate and therefore a high population of CVs at the minimum period, a prediction that is contradicted by observation. By adding the extra angular momentum loss rate from magnetic braking, the cut-off is shifted to longer periods. However, our value of the magnetic braking rate causes the opposite problem. We find that at short periods, the magnetic braking rate is almost 100 times the rate of angular momentum loss due to gravitational radiation. Since

$$P_{min} \propto \left(\frac{\dot{J}}{J_{gr}}\right)^{0.34},$$

this would bring the minimum period up to a value of 331 mins $\simeq$ 5.5 hours, which is clearly not correct.

We also have the continuing problem of how to explain the presence of the period gap - a dearth of systems with periods $2\,h \leq P \leq 3\,h$. If magnetic braking does not shut off as the secondary star becomes fully convective then there is no reason

for systems to cease mass-transfer between those periods. APS03 suggested that instead of a migration of CVs from long- to short-period, the systems above and below the period gap may belong to two different populations, with no migration between the two. However, this is more likely for their longer-timescale angular momentum loss, as their model depends upon the presence of an evolved secondary star, than for our measured magnetic braking rate.

4.6 Conclusions

We have observed 13 primary eclipses of NN Ser using the high-speed CCD camera ULTRACAM and derived times of mid-eclipse, from fitting of light curve models, with uncertainties as low as 0.06 s. The data show that the period of the binary is decreasing, with an average rate of $\dot{P} = (9.057 \pm 0.055) \times 10^{-12}$, which has increased to a rate of $\dot{P} = (2.849 \pm 0.147) \times 10^{-11}$ over the last 2 years. These rates of period change appear difficult to reconcile with any models of orbital period change. If this period change reflects an angular momentum loss, the average loss rate ($\dot{J} = 1.4 \pm 0.6 \times 10^{35}$ergs) is consistent with the loss rates (via magnetic stellar wind braking) used in standard models of close binary evolution, which were derived from observations of much more massive cool stars. It would also imply that there is no cut-off in magnetic braking as the secondary star mass drops below $M = 0.3 M_{\odot}$. Models for low-mass stars such as NN Ser's secondary star predict rates of $\sim$100 times lower than we observe. The alternatives are either magnetic activity-driven changes in the quadrupole moment of the secondary star (Applegate 1992) or a light travel time effect caused by the presence of a third body in a long ($\sim$ decades) orbit around the binary. We have shown that Applegate's mechanism fails by an order of magnitude on energetic grounds, but that the presence of a third body with mass $0.0037\,\mathrm{M}_{\odot} < \mathrm{M}_3 < 0.14\,\mathrm{M}_{\odot}$ and orbital period $15 < \mathrm{P}_3 < 285$ years could account

for the observed changes in the timings of NN Ser's mid-eclipses. We conclude that we have either observed a genuine angular momentum loss for NN Ser, in which case our observations pose serious difficulties for the theory of close binary evolution, or we have detected a previously unseen low-mass companion to the binary.

Chapter 5

Conclusions

Conclusion /nm./: the place where you got tired of thinking

The following chapter summarises the results contained in this thesis, along with suggestions for future work.

5.0.1 Star spots on white dwarfs

We have discovered variability in the cool, low-field, isolated magnetic white dwarfs WD 1953-011 and GD 356. Due to their low temperatures and field strengths, we believe that this variability is caused by the presence of star spots on their surfaces, making these the first detections of star spots on white dwarfs. We have used the period of the variability to derive spin periods for WD 1953-011 and GD 365 of 1.441769(8) days and 0.0803652(3) days respectively. Future work includes the mapping of the surface of these stars using spectropolarimetry in an attempt to directly detect the star spots and verify our theory.

5.0.2 Magnetic white dwarf spin period survey

We have carried out a survey for variability in 34 magnetic white dwarfs from the sample in Wickramasinghe & Ferrario (2000). Of the 30 targets believed to be isolated, we have detected variability in 17, and have derived reliable periods for 5 of these. Of the remaining 13, we have been able to rule out variability in 2 over the observed timescales. We have found no correlation between spin period and age, mass or temperature but there may be a correlation between period and field strength at short periods. We have been awarded Liverpool Telescope time to follow up and test this result for the slow-rotators.

We have identified 14 targets with low field strength and low temperature, which are candidates for having star spots on their surfaces. These should be followed up with spectropolarimetry. We have also found unexpected variability in 3 low-field, high-temperature targets, which are too hot to have convective atmospheres and therefore cannot be displaying star spots. This suggests that star spots are not the only cause of variability in low-field magnetic white dwarfs.

Finally, we have identified one of our targets that appears to be variable on two different timescales - over both hours and months. This is hard to reconcile with our assumption that variability in magnetic white dwarfs is attributable to the spin period, and more data on this object would be welcome.

We have already been awarded robotic Liverpool Telescope time over the next 4 semesters to follow up the targets we suspect are varying over timescales $>$ month. This is a timescale that has not previously been explored for magnetic white dwarfs, since previous detections of variability have either relied on data from week-long observing runs or observed differences in the target between individual observing campaigns years apart. These new data should allow us to more accurately de-

termine the period distribution of magnetic white dwarfs and better test for any correlation between spin periods and other parameters.

5.0.3 The changing period of NN Ser

We have detected a period change in the eclipsing pre-CV NN Ser over the last 15 years of observations, with an average rate of $\dot{P} = (9.057 \pm 0.005) \times 10^{-12}$ and a current rate of $\dot{P} = (2.849 \pm 0.147) \times 10^{-11}$. These rates of period change are difficult to reconcile with any models of orbital period change. If this period change reflects an angular momentum loss then the average loss rate is consistent with the magnetic braking loss rates used in standard models of close binary evolution, which should only be applicable to much more massive secondary stars. It would also imply that there is no cut-off in magnetic braking as the secondary star drops below a mass of $0.3\,\mathrm{M}_{\odot}$, causing problems for theories invoking this cut-off to explain the presence of the CV period gap and the value of the period minimum. The alternatives to a genuine angular momentum loss are either magnetic activity-driven changes in the quadrupole moment of the secondary star (Applegate 1992) or a light travel-time effect caused by the presence of a third body in orbit around the binary. We have shown that Applegate's mechanism fails by an order of magnitude on energetic grounds, but that the presence of a third body with mass $0.0037\,\mathrm{M}_{\odot} < \mathrm{M}_3 < 0.14\,\mathrm{M}_{\odot}$ and orbital period $15 < \mathrm{P}_3 < 285$ years could account for the observed changes in NN Ser's period. We conclude that we have either observed a genuine angular momentum loss in NN Ser, in which case our observations pose serious difficulties for the theory of close binary evolution, or we have detected a previously unseen low-mass companion to the binary. We will continue to monitor this system with ULTRACAM.

Bibliography

Andronov N., Pinsonneault M., Sills A., 2003, ApJ, 582, 358

Angel J. R. P., 1978, ARA&A, 16, 487

Angel J. R. P., Carswell R. F., Beaver E. A., Harms R., Strittmatter P. A., 1974, ApJ, 194, L47

Applegate J. H., 1992, ApJ, 385, 621

Arnaud K. A., Zheleznyakov V. V., Trimble V., 1992, PASP, 104, 239

Aznar-Cuadrado R., Jordan S., Napiwotzki R., Schmid H. M., Solanki S. K., Mathys G., 2005, astro-ph/0501191

Barstow M. A., Jordan S., O'Donoghue D., Burleigh M. R., Napiwotzki R., Harrop-Allin M. K., 1995, MNRAS, 277, 971

Beauchamp A., Wesemael F., Bergeron P., Fontaine G., Saffer R. A., Liebert J., Brassard P., 1999, ApJ, 516, 887

Berdyugin A. V., Pirola V., 1999, A&A, 352, 619

Bergeron P., Leggett S. K., Ruiz M. T., 2001, ApJ Supp., 133, 413

Bergeron P., Ruiz M. T., Leggett S. K., 1997, ApJ Supp., 108, 339

Bergeron P., Saffer R. A., Liebert J., 1992, ApJ, 394, 228

Bergeron P., Wesemael F., Beauchamp A., 1995, PASP, 107, 1047

Bergeron P., Wesemael F., Lamontagne R., Fontaine G., Saffer R. A., Allard N. F., 1995, ApJ, 449, 258

Beurmann K., Reinsch K., 2002, A&A, 381, 487

Bondi H., Hoyle F., 1944, MNRAS, 104, 273

Brinkworth C. S., Burleigh M. R., Wynn G. A., Marsh T. R., 2004, MNRAS, 384, L33

Brinkworth C. S., Marsh T. R., Morales-Rueda L., Maxted P. F. L., Burleigh M. R., Good S. A., 2005, MNRAS, 357, 333

Catalan M. S., Davey S. C., Sarna M. J., Smith R. C., Wood J. H., 1994, MNRAS, 269, 879

Cavallo R., Arnaud K. A., Trimble V., 1993, JApA, 14, 141

Cohen M. H., Putney A., Goodrich R. W., 1993, ApJ, 405, L67

Collier-Cameron A., Jianke L., 1994, MNRAS, 269, 1099

Cumming A., Marcy G. W., Butler R. P., 1999, ApJ, 526, 890

Dhillon V. S., Marsh T. R., 2001, NewAR, 45, 91

Diaconis P., Efron B., 1983, SvA, 248, 96

Dupuis J., Chayer P., Vennes S., Christian D. J., Kruk J. W., 2000, ApJ, 537, 977

Dupuis J., Vennes S., Chayer P., 2002, ApJ, 580, 1091

Faulkner J., 1971, ApJ, 170, 99

Ferrario L., Vennes S., Wickramasinghe D. T., Bailey J., Christian D. J., 1997, MNRAS, 292, 205

Ferrario L., Wickramashinge D. T., Liebert J., Schmidt G. D., Bieging J. H., 1997, MNRAS, 289, 105

Ferrario L., Wickramasinghe D. T., 1997, MNRAS, 356, 615

Fleming T. A., Werner K., Barstow M. A., 1993, ApJ, 416, L79

Fontaine G., Thomas J. H., Horn H. M. V., 1973, ApJ, 184, 911

Friedrich S., Oestreicher R., Schweizer W., 1996, A&A, 309, 227

Glenn J., Liebert J., Schmidt G. D., 1994, PASP, 106, 722

Gnedin Y. N., Borisov N. V., Natsvlishvili T. M., Piotrovich M. Y., 2001, Astrophysics, 44, 321

Gorda S. Y., Svechnikov M. A., 1998, ARep, 42, 793

Green R. F., Liebert J., 1981, PASP, 93, 105

Greenstein J. L., 1986, ApJ, 304, 334

Greenstein J. L., McCarthy J. K., 1985, ApJ, 289, 732

Greenstein J. L., Oke J. B., Richstone D., Altena W. F. V., Steppe H., 1977, ApJ, 218, L21

Groote D., Hunger K., 1982, A&A, 116, 64

Guseinov O. H., Novruzova H. I., Rustamov Y. S., 1983a, Ap. & Sp. Sci., 97, 305

Guseinov O. H., Novruzova H. I., Rustamov Y. S., 1983b, Ap. & Sp. Sci., 96, 1

Haefner R., 1989, A&A, 213, L15

Haefner R., Fiedler A., Butler K., Barwig H., 2004, A&A, 428, 181

Harrington R. S., Dahn C. C., 1980, AJ, 85, 454

Heber U., Napiwotzki R., Reid I. N., 1997, A&A, 323, 819

Hellier C., 2001, Cataclysmic variable stars. How and why they vary. Springer

Jordan S., Schmelcher P., Becken W., 2001, A&A, 376, 614

Karl C. A., Napiwotzki R., Heber U., Dreizler S., Koester D., Reid I. N., 2005, A&A, 434, 637

Kawaler S. D., 1988, ApJ, 333, 236

Kawka A., Vennes S., Wickramasinghe D. T., Schmidt G. D., Koch R., 2003, 13th European Workshop on White Dwarfs, ed. R. Silvotti & D. de Martino (Dordrecht: Klewer), p. 109

Keppens R., MacGregor K. B., Charbonneau P., 1995, A&A, 294, 469

Kim Y., Demarque P., 1996, ApJ, 457, 340

King A. R., Pringle J. E., Wickramasinghe D. T., 2001, MNRAS, 320, L45

Koester D., Allard N. F., 2000, Baltic Astron., 9, 119

Koester D., Dreizler S., Weidermann V., Allard N. F., 1998, A&A, 338, 612

Kolb U., King A. R., Ritter H., 1998, MNRAS, 289L, 29

Kraft R. P., Matthews J., Greenstein J. L., 1962, ApJ, 136, 312

Krishnamurthi A., Pinsonneault M. H., Barnes S., Sofia S., 1997, ApJ, 480, 303

Latter W. B., Schmidt G. D., Green R. F., 1987, ApJ, 320, 308L

Li J., Ferrario L., Wickramasinghe D., 1998, ApJ, 503, 151

Liebert J., 1976, PASP, 88, 490

Liebert J., Bergeron P., Holberg J. B., 2003, AJ, 125, 348

Liebert J., Bergeron P., Holberg J. B., 2005, AJ, 156, 47

Liebert J., Bergeron P., Schmidt G. D., Saffer R. A., 1993, ApJ, 418, 426

Liebert J., Schmidt G. D., Green R. F., Stockman H. S., McGraw J. T., 1983, ApJ, 264, 262

Liebert J., Schmidt G. D., Sion E. M., Starrfield S. G., Green R. F., Boroson T. A., 1985, PASP, 97, 158

Liebert J., Smith G. D., Lesser M., Stepanian J. A., Lipovetsky V. A., Chaffee F. H., Foltz C. B., Bergeron P., 1994, ApJ, 421, 733

Lomb N. R., 1976, Ap. & Sp. Sci., 39, 447

Marsh M. C., Barstow M. A., Buckley D. A., Burleigh M. R., Holberg J. B., O'Donoghue D., Penny A. J., Sansom A. E., 1997, MNRAS, 287, 705

Martin B., Wickramasinghe D. T., 1982, MNRAS, 200, 993

Maxted P. F. L., Ferrario L., Marsh T. R., Wickramasinghe D. T., 2000, MNRAS, 315, L41

Maxted P. F. L., Marsh T. R., 1999, MNRAS, 307, 122

Morales-Rueda L., Maxted P. F. L., Marsh T. R., North R. C., Heber U., 2003, MNRAS, 338, 752

Moran C., Marsh T. R., Dhillon V. S., 1998, MNRAS, 299, 218

Mukadam A. S., Mullally F., Nather R. E., Winget D. E., von Hippel T., Kleinman S. J., Nitta A., Krzesinski J., Kepler S. O., Kanaan A., Koester D., Sullivan D. J., Hometer D., Thompson S. E., Reaves D., Cotter C., Slaughter D., Brinkmann J., 2004, ApJ, 607, 982

Musielak Z. E., Porter J. G., Davis J. M., 1995, ApJ, 453, L33

Naylor T., 1998, MNRAS, 296, 339

O'Brien M. S., 2000, ApJ, 532, 1078

O'Brien M. S., Clemens J. C., Kawaler S. D., Dehner B. T., 1996, ApJ, 467, 397

Patterson J., 1998, PASP, 110, 1132

Pigulski A., Michalska G., 2002, IBVS, 5218

Putney A., 1995, ApJ, 451, L67

Putney A., 1997, ApJ Supp., 112, 527

Putney A., Jordan S., 1995, ApJ, 449, 863

Queloz D., Allain S., Mermilliod J. C., Bouvier J., Mayor M., 1998, A&A, 335, 183

Rappaport S., Verbunt F., Joss P. C., 1983, ApJ, 275, 713

Reid I. N., Mahoney S., 2000, MNRAS, 316, 827

Reimers D., Jordan S., Beckmann V., Christlieb N., Wisotzki L., 1998, A&A, 337, L13

Reimers D., Jordan S., Koehler T., Wisotzki L., 1994, A&A, 285, 995

Reimers D., Jordan S., Koester D., Bade N., K´ohle T., Wisotzki L., 1996, A&A, 311, 572

Scargle J. D., 1982, ApJ, 263, 835

Schmidt G. D., Allen R. G., Smith P. S., Liebert J., 1996, ApJ, 463, 320

Schmidt G. D., Bergeron P., Liebert J., Saffer R. A., 1992, ApJ, 394, 693

Schmidt G. D., Harris H. C., Leibert J., Eisenstein D. J., Anderson S. F., Brinkman J., Hall P. B., Harvanek M., Hawley S., Kleinman: S. J., others ., 2003, ApJ, 595, 1101

Schmidt G. D., Latter W. B., Foltz C. B., 1990, ApJ, 350, 758

Schmidt G. D., Liebert J., Smith P. S., 1998, ApJ, 116, 451

Schmidt G. D., Norsworthy J. E., 1991, ApJ, 366, 270

Schmidt G. D., Smith P. S., 1995, ApJ, 448, 305

Schmidt G. D., Stockman H. S., Smith P. S., 1992, ApJ, 398, L57

Schmidt G. D., Vennes S., Wickramasinghe D. T., Ferrario L., 2001, MNRAS, 328, 203

Schmidt G. D., West S. C., Liebert J., Greeen R. F., Stockman H. S., 1986, ApJ, 309, 218

Sills A., Pinsonneault M. H., Terndrup D. M., 2000, ApJ, 534, 335

Skumanich A., 1972a, ApJ, 171, 565

Skumanich A., 1972b, ApJ, 171, 565

Spruit H. C., 1998, A&A, 333, 603

Spruit H. C., Ritter H., 1983, A&A, 124, 267

Stauffer J. R., Hartmann L. W., Prosser C. F., Randich S., Balachandran S., Patten B. M., Simon T., Giampapa M., 1997, ApJ, 479, 776

Valyavin G., Fabrika S., 1999, ASP Conf. Ser. 11th Workshop on White Dwarfs, ed. J. E. Solhein & E. G. Meistas, 169, 206

Vennes S., 1999, ApJ, 525, 995

Vennes S., Ferrario L., Wickramasinghe D. T., 1999, MNRAS, 302, L49

Verbunt F., Zwaan C., 1981, A&A, 100, 7

Warner B., 1995, Cataclysmic Variable Stars. Cambridge Astrophysics Series

Weber E. J., Davis L. J., 1967, ApJ, 148, 217

Wickramasinghe D. T., Cropper M., 1988, MNRAS, 235, 1451

Wickramasinghe D. T., Ferrario L., 1988, ApJ, 327, 222

Wickramasinghe D. T., Ferrario L., 2000, PASP, 112, 873

Wickramasinghe D. T., Ferrario L., 2005, MNRAS, 356, 1576

Wickramasinghe D. T., Martin B., 1979, MNRAS, 188, 165

Wickramasinghe D. T., Schmidt G., Ferrario L., Vennes S., 2002, MNRAS, 332, 29

Wood J. H., Marsh T. R., 1991, ApJ, 381, 551

Wunner G., R$\acute{}$osner W., Herold H., Ruder H., 1985, A&A, 149, 102

Zheleznyakov V. V., Serber A. V., 1995, Adv. Space Res., 16, 77